Design and Development of Hybrid Controller for Z-Source Inverter: An Application to Electric Vehicle

THESIS

Submitted in partial fulfillment
of the requirements for the degree of

DOCTOR OF PHILOSOPHY

by

A ANANDA KUMAR

Under the supervision of

Prof. Dheerendra Singh

BIRLA INSTITUTE OF TECHNOLOGY & SCIENCE

PILANI – 333 031 (RAJASTHAN) INDIA

2015

Design and Development of Hybrid Controller for Z-Source Inverter: An Application to Electric Vehicle

THESIS

Submitted in partial fulfillment
of the requirements for the degree of

DOCTOR OF PHILOSOPHY

by

A ANANDA KUMAR
[ID.No. 2007PHXF431P]

Under the supervision of

Prof. Dheerendra Singh

BITS Pilani
Pilani | Dubai | Goa | Hyderabad

BIRLA INSTITUTE OF TECHNOLOGY & SCIENCE
PILANI – 333 031 (RAJASTHAN) INDIA

2015

BIRLA INSTITUTE OF TECHNOLOGY & SCIENCE
PILANI – 333 031 (RAJASTHAN) INDIA

CERTIFICATE

This is to certify that the thesis entitled "**Design and Development of Hybrid Controller for Z-Source Inverter: An Application to Electric Vehicle**" and submitted by **A ANANDA KUMAR**, ID.No. **2007PHXF431P** for the award of Ph.D. degree of the Institute embodies the original work done by him under my supervision.

Signature of the supervisor : _____

Name of the supervisor : Dr. DHEERENDRA SINGH

Designation : Assistant Professor

Date : _____

Dedicated

to

my parents

my wife & my daughter ‘Sri Laasya'

Acknowledgements

I wish to express my heartfelt gratitude and sincere thanks to my thesis supervisor Prof. Dheerendra Singh, Department of Electrical and Electronics Engineering at BITS, Pilani, for his able guidance, encouragement and continued support throughout the period of this research work. I have a deep sense of admiration to his innate goodness. It has been a divine grace and my proud privilege to work under his guidance.

Prof. Dheerendra Singh, with his wide experience, sharp and incisive intellect and maestro ability combined with astute research methodology and deep insight of the subject has unerringly steered the work on smooth and steady course. This work owes much to his intellect, vision, didactic guidance, personal involvement and cheerful encouragement. I humbly acknowledge a lifetimes gratitude to him.

I am indebted to Prof. V.S. Rao, Vice-Chancellor, Prof. Ashoke Kumar Sarkar, (Director, BITS-Pilani, Pilani Campus), Prof. G Sundar, Director, Off-Campus Programmes, Prof. S.K. Verma, Dean, Academic Research Division, BITS, Pilani Campus for giving me an opportunity to carry out research at the Institute.

I express my heartfelt thanks to Mr. Rahul Verma, senior scientist, Mr. Ajeet Kumar Dhakar, scientist, Mr. Prashant Kumar Pedapati, Scientist, Industrial Electronics Group (IEG), CSIR Central Electronics Engineering Research Institute, Pilani.

I wish to express my deep sense of gratitude towards the members of Doctoral Advisory Committee (DAC), Prof. Hari Om Bansal and Prof. Hitesh Dutt Mathur, Department of Electrical and Electronics Engineering, BITS, Pilani for their constructive criticism, valuable suggestions and moral support throughout the research work. Their editorial miracles of revision are simply amazing. Without which the thesis would have not taken right shape.

My sincere thanks to Prof. Anu Gupta, Head of Department, Electrical and Electronics Engineering, BITS, Pilani, for her encouragement, and moral support during various phases of research work.

I am grateful for the best wishes and prayers of my friends cum colleagues Prof. V.K. Choube, Prof. S Gurunarayanan, Prof. Surekha Bhanot, Prof. Rajneesh Kumar, Prof. Navneet Gupta, Prof. Pradyumn Chaturvedi, Prof. Rahul Singhal, Mr. K. Srinivasa Reddy and Mr. Nitin Chaturvedi.

Co-operation and encouragement of my friends and colleagues at BITS, Pilani, who with their caring words, constructive criticism and suggestions have contributed directly or indirectly in a significant way towards completion of this thesis, are gratefully acknowledged.

The support extended by librarian of the Central Electronics Engineering Research Institute (CEERI) Pilani, is acknowledged.

Special thanks to Mr. Giridhar Kunkur, Librarian (BITS-Pilani, Pilani Campus) for making timely availability of various books and on-line journals.

Also, I would like to thanks Mr. Santosh Kumar Saini (ARC Division, BITS-Pilani, Pilani Campus) for his help in compilation of thesis.

A very special and sincere heartfelt gratitude to my parents, Mr. K P Balasubramanyam and Mrs. K Uma Devi, to my daughter Sri Laasya and to my wife Mrs. Santhi, whose constant persuasion and moral support have been a source of inspiration to me. No words can adequately express my gratitude to them.

Lastly, my deepest gratitude is due to the All-pervading, All-sustaining spirit whose divine light and warmth provided me the perseverance, guidance, inspiration, faith and strength to carry on even when the life got tough.

A ANANDA KUMAR

Abstract

The development of automobiles with heat engines is one of the greatest achievements of 20^{th} century and marvel of modern technology. However, the highly developed automotive industry and the large number of automobiles in use around the world have caused and are still causing serious health and environmental problems for society and human life. It has been well recognized that electric and hybrid electric drive train technologies are the most promising solutions to the problem of land transportation in the future.

In fact, the choice of electric-propulsion systems for electrical vehicle (EV) mainly depends on three factors: driver expectation, vehicle constraint, and energy source. With these considerations, it is obvious that the overall motor operating point is not tightly defined. Therefore, selecting the most appropriate electric-propulsion system for an electrical vehicle is a challenging task.

From drive point of view, the major types of electric motors adopted or under serious consideration for EVs include DC motor, induction motor (IM), permanent magnet (PM) synchronous motor and switched reluctance motor (SRM). Moreover, based on an exhaustive review of the state of the art related to electric-propulsion systems, it is observed that investigations on the cage IMs and the PM motors are highly dominant, whereas those on DC motors are decreasing.

Advanced electric vehicles (EVs) require efficient power electronics and electrical machines to function the general-purpose motor drive for EVs system is based on the voltage-source inverter (VSI). Where DC voltage source is supported by a relatively large capacitor feeds the main converter circuit. The DC voltage source can be a battery, fuel-cell stacks, diode, rectifier and solar cells. However, voltage-source inverter has conceptual and operational barriers and limitations. The voltage-source inverter is a buck (step-down) inverter for DC-to-AC power conversion. The AC output voltage is limited below and cannot exceed the DC-rail voltage. For applications where overdrive is desirable and the available DC voltage is limited, an additional DC-DC boost converter is needed to obtain a desired AC output. The additional boost converter stage increases system cost and lowers efficiency. The upper and lower devices of each phase leg cannot

be gated on simultaneously either by purpose or by EMI noise. Dead time to block both upper and lower devices has to be provided in the voltage-source inverter, which causes waveform distortion. Therefore, many research efforts have been focused on developing new converters and inverters suitable for electric vehicle applications. Of late one of the most promising topologies, Z-source inverter (ZSI) is being explored and investigated. Where utilizes the zero states to boost the input voltage, improves the inverter reliability and enlarges its application field. In comparison with other power electronics converters, it provides an attractive single stage DC/AC conversion with buck-boost capability with reduced cost, reduced volume and higher efficiency. Therefore, the ZSI is a very promising and competitive topology for vehicular applications.

As a research hot-spot in power electronics converters, the Z-source topology has been greatly explored from various aspects, such as: shoot-through control methods, designing of the Z-network elements, modeling of the Z-source, DC-link control strategies, motor speed control algorithms for automotive applications. The control of DC-link voltage is a key point which is turns the output of the Z-source inverter, therefore the controller design is focused on how to control the peak DC-link voltage. The DC-link voltage which is pulsating with a high frequency (approx. 3 times of switching frequency), it reaches its peak value in non-shoot-through state and keeps zero in shoot-through state. Such a pulse voltage introduces difficulty in measuring its peak value directly. Hence, an indirect peak DC-link voltage control strategy is developed by with the help of mathematical model of Z-source inverter.

The precise control of peak DC-link voltage of the inverter is very essential for reliable electrical vehicle drive operation. Where (Z-source inverter fed induction motor drive) DC-link voltage drops occur due to increase in output load-torque. This leads to inefficient speed control and eventually the stopping of the electrical vehicle drive. The dynamic response of the Z-source inverter fed induction motor drive depends on the type of peak DC-link voltage controller. In this research work, the considered close loop peak DC-link voltage controllers are Zeigler-Nichols (ZN) based proportional integral (PI) controller and a fuzzy based fuzzy gain scheduled proportional integral (FGS-PI) controller designed and developed for unified speed and voltage control. A comparative study of responses obtained from prototype experimental setup developed in laboratory.

Z-source inverter fed induction motor drive is made based on real time and hybrid controller for DC-link voltage control algorithm is suggested.

Also, a comprehensive mathematical modeling of Z-source inverter fed induction motor drive system is carried out to analyze and design the drive system. The dynamic response of the Z-source inverter fed induction motor drive under various operating conditions such as speed and load perturbations are simulated in MATLAB environment using Simulink and power system block set (PSV) toolbox. The controller of the drive uses three feedback signals namely currents in two of the motor phases (i_a and i_b) the rotor speed (N_r), the Z-source inverter input voltage (V_{in}) and the Z-network capacitor voltage (V_c). The controller consists of the closed loop speed controller for generating the torque reference (T^*), field controller for providing the reference value of excitation current, the vector controller for generating two quadrature current signals for control of torque and flux. Additionally, peak DC-link voltage has been controlled using the input voltage and capacitor voltage through the controller, this controller generates the shoot-through duty ratio (D_{sh}) for boosting the voltage. The two phase stationary voltage signals from vector control and shoot-through duty ratio are used for generating the modified space vector pulse width modulated gating signals for the solid state devices of the inverter.

The power circuit consists of two current sensors for motor currents, one AC tacho-generator for motor speed measurement and two voltage sensors one for input and one capacitor voltage. These signals are fed to the ADC of digital signal processor. For the implementation of the control algorithm, a dedicated digital signal processor (TMS320F28335) is used to reduce system hardware to a great extent. The entire control algorithm is coded in 'C' language. The processor facilitates the implementation of speed and DC-link voltage control algorithm.

List of Tables

List of Figures

List of Abbreviations

CBC	Constant Boost Control
CCM	Continuous Conduction Mode
CSI	Current Source Inverter
DRFO	Direct Rotor Field Orientation
DSFO	Direct Stator Field Orientation
DSP	Digital Signal Processor
EMI	Electro Magnetic Interference
EV	Electric Vehicle
FCHEV	Fuel Cell Battery Hybrid Electric Vehicles
IM	Induction Machine
IPM	Interior permanent magnet machine
IRFO	Indirect Rotor Field Orientation
MBC	Maximum Boost Control
PID	proportional integral derivative
PWM	Pulse Width Modulation
RHP	Right Hand side Poles
SBC	Simple Boost Control
SPM	Surface Permanent Magnet Machine
SRM	Switched Reluctance Machine
SVM	Space Vector Modulation
TSVM	Traditional Space Vector Modulation
VSI	Voltage Source Inverter
ZSI	Z-Source Inverter

Chapter - 1

Introduction

Power electronics is widely being used in almost every walks of life, be it domestic or industrial applications. The inverter converts DC voltage/current into AC voltage/current and it is one of the most popular converters. Inverter has been generally used in motor drives [1-2], induction heating [3], AC uninterruptible power supplies (UPS) [4-7], AC power supplies [8-10], distributed generation [11-16], electric vehicles [17-22] active power filters [23-24], and static VAR generators or compensators [25-26] etc. There are two types of traditional inverters, voltage source inverter and current source inverter. However, both inverters have some conceptual limitations. The Z-source inverter has some unique features and overcome some of traditional inverters limitations [27]. The purpose of this research work is to investigate the properties of the Z-source inverter and its applications.

1.1 Voltage Source Inverter

Figure 1.1 shows the topology of voltage source inverter (VSI). The input to inverter is a DC voltage source, which is usually with a capacitor in parallel to absorb the high frequency current ripple. The inverter bridge consists of six switches with a freewheeling diode in anti-parallel with each of them.

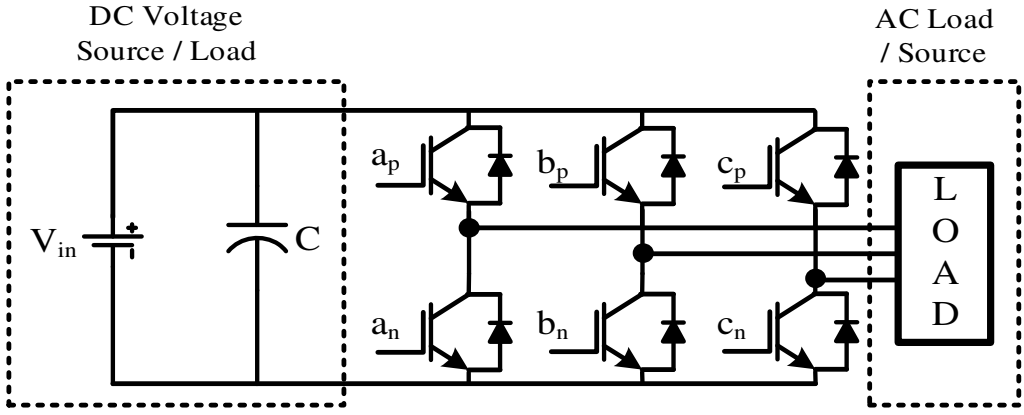

Figure 1.1: Three-phase voltage source inverter

The inverter has two kinds of control methods, one is six step control, which turns each switch on and off only once per fundamental cycle creating a six step stair case waveform for the output phase voltage. The other method is pulse width modulation, which switches the devices at high frequency (tens of kHz) to output a voltage with very few low frequency harmonics as well as to control the output voltage level.

For six-step control, the output line-line peak fundamental voltage is

$$V_P = \frac{2\sqrt{3}V_{in}}{\pi} \tag{1.1}$$

where 'V_{in}' is the DC bus/rail voltage.

The output peak phase voltage can be expressed as

$$\hat{V}_{ac} = \frac{m.V_{in}}{2} \tag{1.2}$$

where 'V_{in}' is the input voltage, and 'm' is the modulation index, which ranges from 0 to 1 with third harmonic injection or space vector pulse width modulation control.

The six-step method has advantages such as simple and low switching losses. However, it is unable to eliminate the low frequency harmonics in the output voltage.

The sketch of the basic pulse width modulation control for voltage source inverter is shown in Figure 1.2.

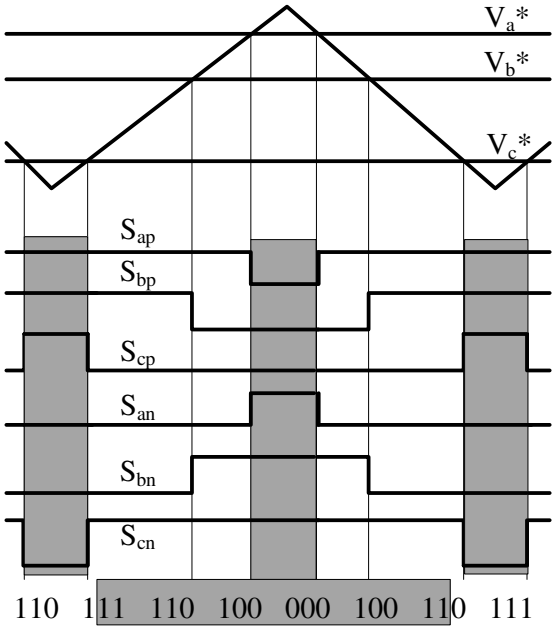

Figure 1.2: Switching pulses for voltage source inverter

The two switches on the same phase leg are turned on and off complementary. There are ‘8' switching states including `6' active states (001,010,011,100,101,110) and ‘2’ zero states (000, 111) when the upper ‘3’or lower ‘3’ switches are gated on shorting the load terminals.

1.1.1 Limitations of Voltage Source Inverter

The voltage source inverter has several limitations:
From equation (1.2), the inverter output voltage range is limited, the inverter output line-line voltage cannot be a higher than the DC-link voltage. For many applications like a fuel cell, photo-voltaic array, and during voltage sag etc., the input DC-link voltage is not always constant. A DC-DC boost converter is often needed to boost the DC-link voltage to meet the required output voltage. This increases the system complexity, cost and reduces the system reliability.

The two switches on the same phase leg should not be gated on at the same time; otherwise a short circuit will occur and may destroy the inverter. The mis-triggering caused by electromagnetic interference is a major killer of the inverter. For safety reasons, there is always a dead time (3 to 10 μs) to make sure that the two switches will not be turned on simultaneously. However, the dead time causes output voltage distortion and harmonic problems. The harmonic problem can be solved by implementing a current/voltage feedback control [28]. However, this increases the system complexity. A LC filter is needed for the load side compared to current source inverter, which increases the complexity and reduces the system efficiency.

1.2 Current Source Inverter

The current source inverter (CSI) is shown in Figure 1.3. The input to inverter is a current source or a voltage source with a large inductor in series. The inverter bridge consists of six switches with a reverse blocking diode in series or switches with reverse blocking ability. Three capacitors are connected at the AC side of the inverter to provide a leading power factor load. Because of the reverse blocking nature of the thyristor, it is often used in current source inverter. However, due to the fact that it is unable to be turned off by the gate signal, a leading power factor load is required to enable load commutation. This also limits the control to be six-step only, which will cause lots of low frequency harmonics in the output waveform. Another group of

current source inverter use self-commutated devices, such as GTO, IGBT, with reverse blocking diode in series. Generally the following rule has to be followed: there must be at least one device in the upper three devices and one in the lower three devices gated on at the same time to provide a current path.

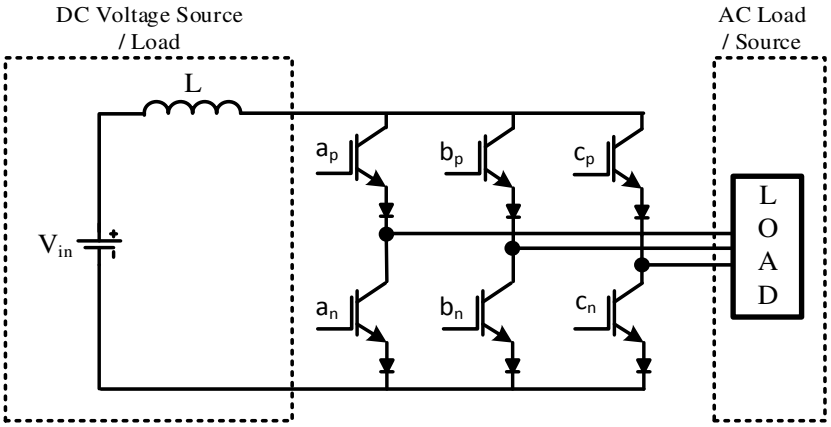

Figure 1.3: Three-phase current source inverter

1.2.1 Limitations of Current Source Inverter

To keep the inductor average voltage zero, the maximum inverter DC side voltage, which is the peak line-to-line output voltage of the inverter has to be greater than the input DC voltage. Therefore, the inverter is basically a boost converter. For applications where a wide voltage range is required, extra circuitry has to be used to obtain the required voltage. The commonly used methods include using a DC converter or a controlled rectifier [29-30]. However, these methods increase the circuit complexity and reduce the efficiency as well as the reliability.

At least one switch in the upper three devices and one in the lower three devices has to be turned on at the same time, or an open circuit will occur and destroy the inverter. Mis-trigger caused by the electromagnetic interference (EMI) noise could significantly reduce the inverter reliability. To make sure that there will be no open circuit, overlap time is often needed, which will cause distortion in output waveform and low frequency harmonic problem.

The main switches should have reverse blocking capability, which requires an extra diode in series with high-speed high-performance switches, such as an IGBT. This will reduce the system efficiency. With emergence of the reverse blocking IGBT, this might not be a problem anymore [31].

1.3 Impedance/ Z-Source Inverter

The impedance/ Z-source inverter (ZSI) can overcome some of voltage source and current source inverters limitations,

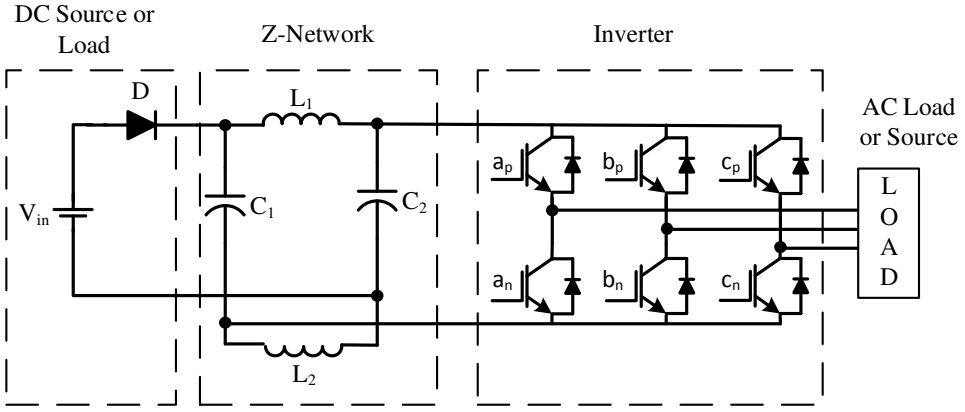

Figure 1.4: Three-phase Z-source inverter

The Z-source inverter employs a Z-network ($L_1 = L_2$ & $C_1 = C_2$) between input source voltage and inverter bridge as shown in Figure 1.4. A modified pulse width modulation control scheme is shown in Figure 1.5, in which there is one more switching state, the shoot through state, besides the eight switching states (six active states and two zero states) for traditional voltage source inverter.

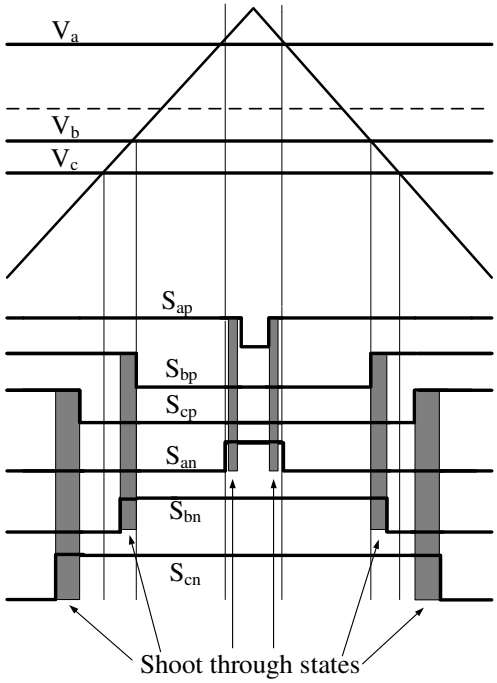

Figure 1.5: Switching pulses for Z-source inverter

With the Z-network, the shoot through state intentionally added to boost the output voltage. The output voltage is higher or lower than DC-link voltage. Therefore, the inverter is a buck-boost type converter and can output whatever voltage desired, and overcome the voltage limitation of the voltage source inverter and current source inverter. With the ability to handle the shoot through state, the reliability of the Z-source inverter is greatly enhanced. Also, without need of dead time, distortion of output waveform can be avoided.

The Z-source inverter, the output peak phase voltage is

$$\hat{V}_{ac} = m.B\frac{V_{in}}{2} \tag{1.3}$$

Where 'm' is modulation index, 'V_{in}' input voltage and 'B' is boost factor.

'B' is expressed as,

$$B = \frac{1}{1-2\frac{T_{sh}}{T}} \tag{1.4}$$

where 'T_{sh}' is the shoot through time per cycle and 'T' is the switching time period. In summary, the Z-source inverter has several unique features:

1. The inverter can boost and buck the output voltage with a single stage structure.
2. The shoot through caused by electromagnetic interference (EMI) can no longer destroy the inverter, which increases the reliability of inverter greatly.
3. The converter does not required dead time and the output waveforms are close to sinusoidal.

1.4 Literature Review

This section outlines the major works reported so far in the Z-source inverter topology and its control circuits for different applications. Z-source inverter with the ingredient of buck-boost feature y was first proposed by in [27].

In Z-source inverter, the output voltage and shoot-through was controlled through shoot-through controlled methods. In the simple boost control, the shoot-through state time periods are generated by two straight lines which are equal or greater than the peak values of the modulating reference sinusoidal signals. When the magnitude of triangular

waveform is greater than the positive straight line, or lower than the negative straight line, the circuit turns into shoot-through state, otherwise it operates just as traditional carrier based pulse width modulation. In this method, three phase reference wave forms are compared with the high frequency carrier wave (triangular wave) having constant peak value. Comparator, compares these two signals and produces pulses (when $V_{sin} > V_{tri}$, ON pulse and $V_{sin} < V_{tri}$, OFF pulse). The shoot-through time periods generated by the two straight lines are inserted in this switching wave forms by logical 'OR' gate. These pulses are then sent to gate terminals of the power IGBTs through isolation and gate driver circuit. Simple boost control (SBC) is uncomplicated method, however, the resulting voltage stress across the device is relatively high because some traditional zero states are not utilized either partially or fully. The voltage stress across the switches is quite high when simple boost control is used, and this characteristic would restrict the obtainable voltage gain because of the limitation of device voltage rating.

Maximum boost control (MBC) was proposed to produce maximum voltage gain (boost) under a given modulation index [32]. Maximum boost control turns all traditional zero states into shoot-through zero state. The voltage stress across the switching devices is greatly reduced by fully utilizing the zero states. Indeed, turning all zero states into shoot-through state could minimize the voltage stress; however, doing so also causes a shoot-through duty ratio varying in a line cycle, which causes inductor current ripple. This would require a high inductance for low frequency or variable frequency applications. Maximum boost control method maintains the six active states unchanged and turns all zero states into shoot-through zero states.

The constant boost control (CBC), which could obtain maximum voltage gain at any given modulation index without producing any low-frequency voltage ripple that is related to the output frequency and minimizes the voltage stress at the same time [33]. In constant boost control method, the inverter could achieve the minimum passive component requirements. This method would increase the voltage stress across the devices by a small amount compared to the maximum boost control method. This method is very suitable for minimizing the Z-source network, especially in variable speed drive applications. This method is suitable for limited applications and provides less voltage boost in the DC-link than the maximum boost control.

A detailed analysis of the various conventional pulse width modulation strategies could be modify to switch a Z-source inverter either is continuous or discontinuous mode, while retaining all the unique harmonic performance features [34-35].

The Z-source inverter based control for AC motor drive system is proposed in [36-38] and it outlined the various features and advantages of Z-source inverter fed induction motor system over the traditional voltage source inverter/current source inverter based drive systems. The operating principle including different modes of operation of current mode Z-source inverter fed induction motor drive system had discussed in [39]. The different pulse width modulation schemes that could be used for Z-source inverter control to achieve buck-boost energy conversion with random and reduced common mode switching [40]. A photovoltaic power conditioning system based on Z-source inverter for residential usage. The system realizes the boost and inversion with maximum power tracking in one single power stage, thus minimizing the number of switching devices [41].

Applications such as distributed generation demand quality output waveforms, and additionally, when the system is subjected to input and load side disturbances, their effects need to be minimized. This could be achieved with closed loop control, here the system was modeled first with small signal modeling technique, and relevant transfer functions were derived [42]. The DC side of the Z-source inverter shows a non minimum phase characteristic, and the output voltage of a Z-source network shows a significant overshoot and undershoots, following a step change in the input due to energy resettling. These effects could be transferred to the AC side, giving oscillations in the AC output as well. Hence, multi loop controllers should be employed to minimize such effects. The DC and AC sides were considered separately when designing the controllers.

Indirect controller algorithms for the control of DC-link voltage on the DC side and also the AC output voltage was given in [43]. An indirect controller was employed in the DC side, whereas the AC side controller is designed in the synchronous reference frame. The modulation index, shoot-through time, and saturation levels were appropriately selected so that the DC side effects were prevented from propagating into the AC side. The derived transfer functions prove the presence of right hand side poles (RHP) and non minimum phase characteristics in the DC side. These characteristics

impose complications in designing the controllers. In this method, the AC and DC sides were considered as separate units, and the controllers were designed to achieve good voltage regulation and disturbance rejection.

To design controllers for Z-source converter, it requires a proper dynamic modeling and analysis. It is apparent that an accurate small signal model of Z-source converter is needed, which not only give a global but a detailed view of system dynamics, providing design guidelines [44]

A proportional integral derivative (PID) controller for DC-link voltage boost in Z-source inverter is presented in [45]. With this compensator, a constant capacitor voltage could be achieved with an improved transient performance. By adding the compensator, which enhances the rejection of disturbance, including the input voltage ripple and load current variation and have good ride through for voltage drops. Controller design for specific applications, namely fuel cell and voltage sag compensation are discussed in [46]. Unified control technique has been presented in [47] for Z-source inverter with minimal number of sensors and PI controllers. Operation modes and characteristics of the Z-source inverter with small inductance or low power factor have been discussed in [48].

An improved Z-source inverter topology has proposed in [49]. Compared to the traditional topology, the improved one could reduce the Z-source capacitor voltage stress significantly to perform the same voltage boost, and has inherent limitation to inrush current at starting. This was proposed with a modified configuration of the Z-source power circuit.

Selection of the components of the Z-source converter is described in [50]. It emphasizes the relevance of the output to input voltage ratio and of the DC-link frequency for the installation size of the passive and active components. A presented design procedure for optimized throughput of power uses a DC equivalent circuit and leads to minimized passive components. With this set of parameters, further characteristics of electric and thermal stress of the components could be determined analytically and also by simulation. This research also comprises of design formula in general form and its evaluation for an experimental test set up for a 10 hp phase standard motor. By means of a DC equivalent circuit analysis and a simulation, it had

been shown that small sized passive components of the Z-source drive converter is adequate to compensate low voltages of the mains and further unavoidable voltage drops and thereby the reduction of efficiency of the induction motor could be prevented. Though additional losses occur in the Z-source inverter, which have to be compared with the reduced losses of the induction motor, the Z-source inverter is worth considering, because the developments of power semiconductors would increase its advantages and reduce its disadvantages.

An electrical vehicle system based on the high performance Z-source inverter which could operate at wide load range with small inductor which is very suitable for electrical vehicle system [51], eliminate the possibility of the DC-link voltage aberrations and then decrease the iron loss of the motor. The operation modes, voltage relation-ship of the high performance Z-source inverter with electrical vehicle system, and a partly pulse width modulation control strategy, which consists of the V/f law, had been described in detail. Presence of the additional transistor makes the control circuit more complex.

A fuel cell battery hybrid electric vehicle system power control strategy to control power from the fuel cell, power to the motor, and State of charge (SOC) of the battery, using the Z-source inverter is presented in [52]. The Z-source inverter is very promising for use in fuel cell hybrid electric vehicles (FCHEVs) because it is less complex and more cost effective than a DC-DC boosted inverter, greater reliability due to shoot-through can no longer destroy the inverter, no need for any DC-DC converters to control the battery SOC.

A dual-loop peak DC-link voltage control technique for controlling the peak DC-link voltage for a Z-source inverter with inductive load is developed in [53], where the outer voltage loop provides the inductor current reference and the inner current loop produces the shoot through duty ratio. Here the modulation index is calculated based on the maximum constant boost control method, where, the peak DC-link voltage is estimated by measuring both the input and capacitor voltages. The two controllers are designed based on a third-order small signal model of the Z-source inverter. Both controllers are implemented using the direct digital design method using a digital signal processor (DSP) linked with MATLAB for automatic code generation.

1.5 Motivation and Objectives

The electric vehicle applications are increasing in commercial areas. The voltage ride-through issues are more and more in electric vehicles. Electric vehicles are often subject to voltage disturbances such as drops and momentary interruptions [54].

The voltage dips could disrupt the voltage source inverter fed electric vehicle systems and the critical load. The power quality related problems in electric vehicles are due to the short-lived (typically 0.1 to 2 s) voltage dips of 10 to 50% below the nominal voltage. The DC-link capacitor in an electric vehicle could not hold DC voltage above the operable level under such voltage drops, because it is a relatively small energy storage element. It leads to a lack of ride through capability for sensitive loads driven by electric vehicles [55].

The tripping may occur owing to several causes,

- DC-bus under voltage (controller or protection tripping).
- Increased AC current during the droop.
- Droop in speed or torque variations.

Thus, concerns about these difficulties have increased and the amount of research on the ride-through systems has also increased. Ride-through solutions are classified in [56].

The voltage source inverter based drive modifications are:

1) Extra boost rectifier.
2) An active rectifier at front end.

Structure 1 the additional boost rectifier consists of the existing rectifier to maintain the DC-link voltage during voltage dips. It has two major disadvantages. First, due to the extra current drawn throughout voltage dip, extra hardware is essential, which has to be properly rated. Second, in the case of an outage, the boost rectifier cannot ride-through voltage sag.

Structure 2 the active rectifier is used in-stead of the existing rectifier. It has disadvantages of being over-rated on current ratings of all existing rectifier elements. So, the ride-through ability of the rectifier is delimited. In case of an outage, the active rectifier cannot provide ride-through voltage drop.

The problem in adding a boost converter to a voltage source inverter is that it in-creases the cost and lowers the efficiency and reliability of the system. When the load on a drive is suddenly increased, the DC-bus voltage experiences voltage drop. This drop can be so much to the extent that it could lead to a loss of power delivery to the load. This voltage drop has to be compensated for better reliability. In addition to this, the dead time in which the inverter is operated to ensure safety distorts the output voltage waveform. A combined solution for voltage drop compensation and minimization of output voltage distortion is Impedance or Z-source inverter. A Z-source inverter has a Z-network between the three-phase rectifier and the inverter. Z-source inverter intentionally avoids the dead time and creates a shoot-through to boost the DC-link voltage in the Z-network which in-turn compensates the voltage drop.

The work presented in this thesis is to be to develop a peak DC-link voltage control of Z-source inverter fed induction motor drive for electric vehicle. This work aims to understand the challenges in controlling the peak DC-link voltage and speed control of induction motor drive fed Z-source inverter. Thus the objectives of this research were to Simulate, real time implementation and investigate the Z-source inverter fed induction motor drive for electric vehicle application.

In order to fulfill these objectives the work was divided into following steps:

- Small signal modeling of Z-source inverter.
- The shoot-through calculation and DC-link voltage control algorithm for Z-source inverter.
- Implementation of indirect field oriented control of voltage source and Z-source inverter fed induction motor drive.
- The comparison between Ziegler-Nichols PI controller and fuzzy gain scheduling PI controller to control the peak DC-link voltage of Z-source inverter.
- Simulation and hardware implementation of Z-source inverter fed induction motor drive for speed and peak DC-link voltage control for electric vehicle.

1.6 Structure of the Thesis

The entire research work is arranged in eight chapters. The organization of this thesis is as follows:

Chapter 1: The introduction with general overview and the limitations of the current state of the art. The following topics are discussed in detail: inverter topology overview and limitations of their limitations, structure and advantages of the Z-source inverter. The detailed literature review of Z-source inverter fed induction motor drive. Finally, the objectives and motivation toward this research is laid down in last section of this chapter.

Chapter 2: Presents the selection criteria of power converter and electrical machine for electrical vehicle. The selection of power converter topology is crucial in the design of an electrical vehicle system. Different types of power converters are discussed and compared.

Chapter 3: Presents a small signal model of the Z-source inverter for inductive load. A detailed analysis of Z-source inverter is essential to design proper control for Z-source inverter. A small signal model would give an overview as well as a detailed look into the functioning and the dynamics of the system enabling us to know the limits of the system and design accordingly. The vector control method speed control of the induction motor.

Chapter 4: Discusses various pulse width modulation methods for the Z-source inverter, and presents five pulse width modulation methods to achieve simple boost, maximum boost, maximum constant boost, modified space vector pulse width modulation, and a new method double space vector pulse width modulation.

Chapter 5: Mainly focuses on the peak DC-link voltage control through the linear/ non-linear (hybrid) controller, to get high performance of the drive under all operating conditions. The classical Zeigler-Nichols and Fuzzy Gain Scheduling PI controller's parameters tuning for peak DC-link voltage control are discussed.

Chapter 6: This chapter presents the real time implementation of the Z-source inverter fed induction motor drive. The speed and peak DC-link voltage are controlled by indirect field oriented control method with modified space vector pulse width modulation technique using TMS320F28335 DSP. The digital implementation of Z-source inverter fed induction motor drive in six levels with detailed explanation.

Chapter 7: Presents, the proposed algorithm its testing on MATLAB/SIMULINK plate form and the same is validated on prototype Z-source inverter fed induction motor setup in laboratory. The speed and peak DC-link voltage of Z-source inverter fed induction motor, emulating electrical vehicle subjected to various dynamical conditions were measured. The drive's performance investigation was carried out and the inferences on behavior were drawn.

Chapter 8: Summarizes the research work and gives future research directions.

Chapter - 2

Power Converter and Electric Machine: Selection

The selection of the power circuit topology is crucial in the design of an electrical vehicle system. The associated power electronics technology used in power conversion in the electrical vehicle has important considerations in its working capabilities under various operating conditions. Hence, for the power conversion, a traditional voltage source inverter or a current source inverter can be used. A conventional voltage source inverter (Figure 2.1) acts as a DC-AC buck inverter or an AC-DC boost rectifier with a constraint, that AC output voltage does not exceed the DC bus voltage, where as a conventional current source inverter (Figure 2.2) acts as a DC-AC boost inverter or an AC-DC buck rectifier, the AC output voltage is higher than the input DC voltage, that is fed to the inductor. Due to these constraints both topologies do not prove to be efficient proposition for inverter selection and functionality for the electrical vehicle.

2.1 Power Circuit Topology

A power circuit is employed to attain the elastic input DC voltage to the voltage source inverter. The inverter has to accommodate increased voltage at high speed, less voltage and inrush current initially (at the time of starting) of AC drive.

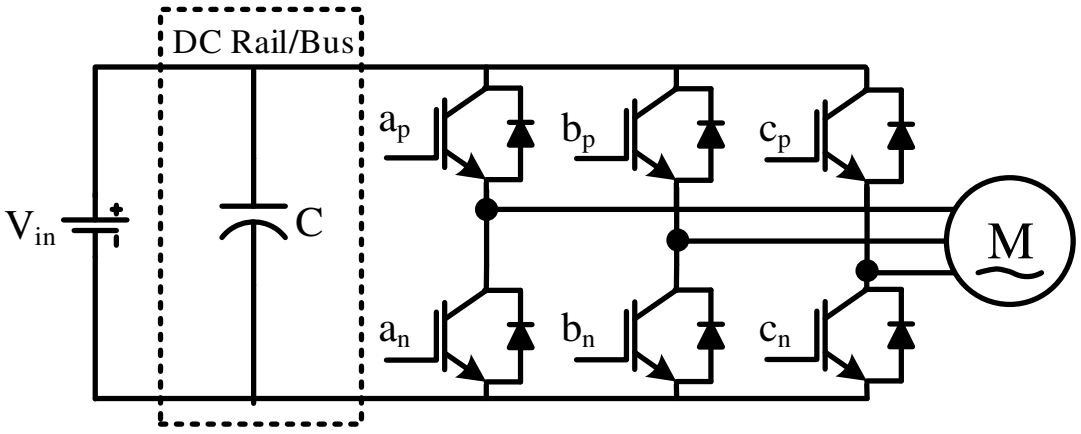

Figure 2.1: Conventional VSI topology

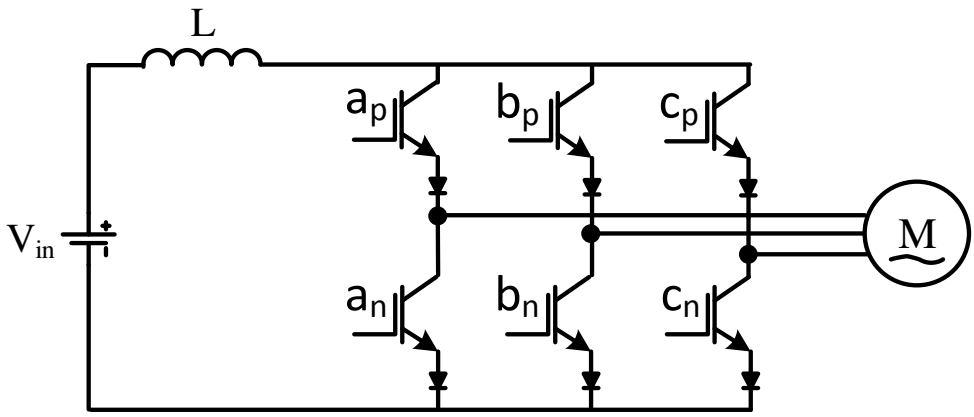

Figure 2.2: Conventional CSI topology

2.1.1 Cascaded DC-DC and Voltage Source Inverter

Another version of the DC-DC-AC power converter is boost converter with voltage source inverter [57-58]. The Figure 2.3 shows the circuit topology for the cascaded DC-DC and voltage source inverter. The capacitance at the bridge of the DC-DC and DC-AC networks keeps the operations decoupled. In voltage source inverter, the output AC voltage is less then input voltage, because the voltage source inverter itself is a buck converter viewed from DC to AC side. It essentially is a cascade of the traditional voltage source inverter and DC-DC boost converter.

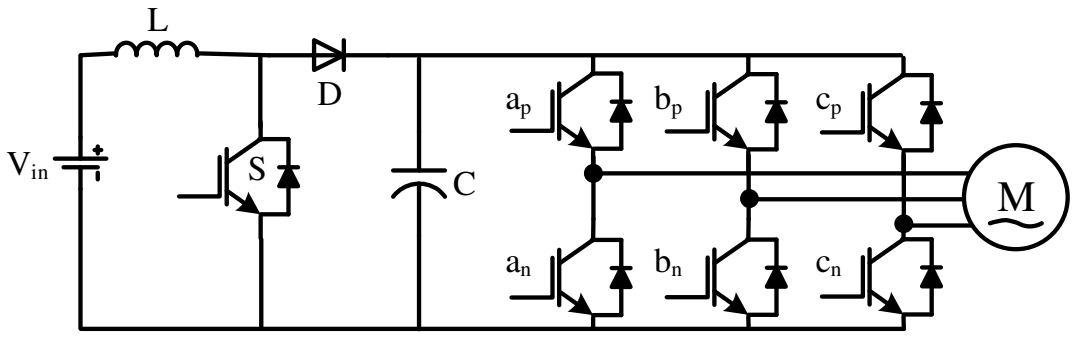

Figure 2.3: DC-DC-AC converter based on boost converter

Currently, two existing inverter topologies are used for electrical vehicles: the conventional 3-phase PWM inverter and a 3-phase PWM inverter with a DC-DC boost converter at front end. Because of the wide voltage change and the limited voltage level of the battery, the conventional PWM inverter topology imposes high stresses on the switching devices and motor. The DC-DC boosted PWM inverter topology can alleviate

the stresses and limitations. However, it has other problems, such as the high cost and complexity associated with the two-stage power conversion.

2.1.2 Impedance/ Z-Source Inverter

In early 2000s, a novel power source converter called Z-source converter was designed for variable speed applications [37]. This Z-source inverter, shown in Figure 2.4 can provide output AC voltage of between zero to infinity.

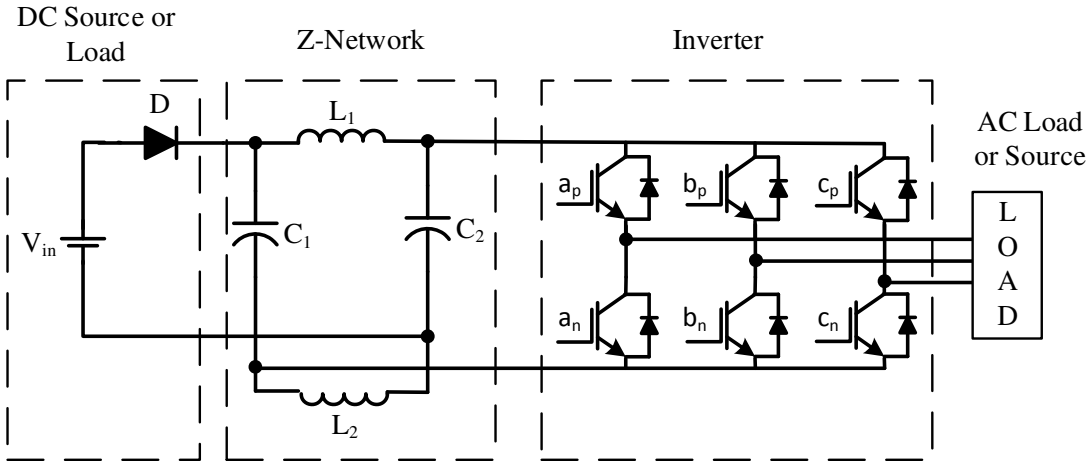

Figure 2.4: Impedance/Z-source inverter

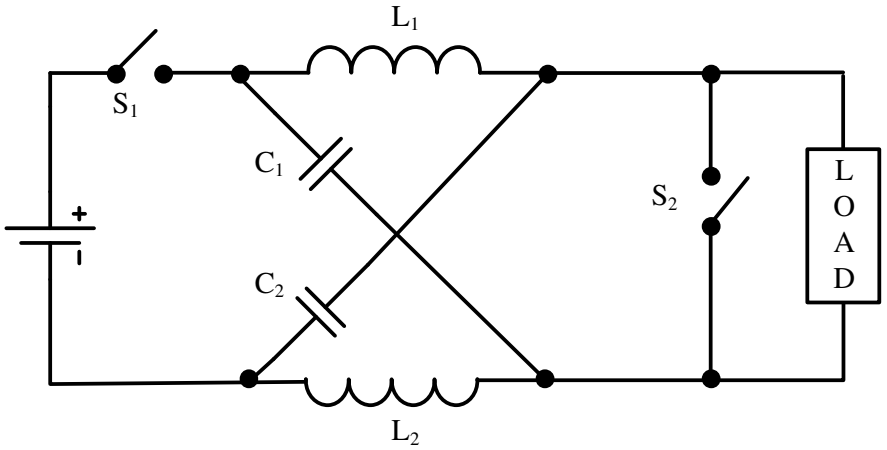

Figure 2.5: Equivalent circuit of Z-source inverter

The Figures 2.4 and 2.5 shows the general arrangement of a standard Z-source converter and its equivalent circuit model respectively. The relationship among the shoot-through duty ratio, modulation index and buck-boost factor is discussed in

[59]. The switch 'S_1' encounters excessive initial current and hence experiences immense operational stress, due to the overlap in the processes of energy transfers between the DC-AC and DC to the Z-source network. The voltage ripple across the DC bus capacitor employed in voltage source inverter is far less in comparison to the ripple across the Z-network capacitor.

The choice of inductors and capacitors associated with the Z-source topology is crucial. First, the resonance should be counter acted with the selection of the reactive elements. The reactive components ought to be sufficiently large to minimize the ripples in voltage and current across the capacitance and inductance respectively. The possibility of minimization of the reactive elements is reaffirmed by the dominance of the equivalent switching frequency in the Z-source network as compared to voltage source inverter due to the even dispersal of shoot-through states in the PWM cycles. The unique dynamics of switching in the reactive components of the Z-source network need to be incorporated in a steady state model for an efficient system design.

2.2 Machine Selection

The unwanted maintenance necessities of brush type DC machines limit the machine candidature to AC machines like:

1. Squirrel Cage Induction Machine (IM)
2. Permanent Magnet Synchronous Motor (PMSM) or BLDC Motor
3. Switched Reluctance Machine (SRM)

2.2.1 Squirrel Cage Induction Machine (IM)

The three phase induction motors are broadly accepted as the most possible applicants for the electric propulsion of electrical vehicles due to their ruggedness, reliability, low maintenance, low cost, and capability to operate in hostile environments. They are mainly well suited for the rigors of industrial and traction drive environments. Today, induction motor drive is the most mature technology among various commutator-less motor drives. Vector control of induction motors can decouple its torque control from field/flux control. Figure 2.6 shows the typical characteristics of an induction motor drive.

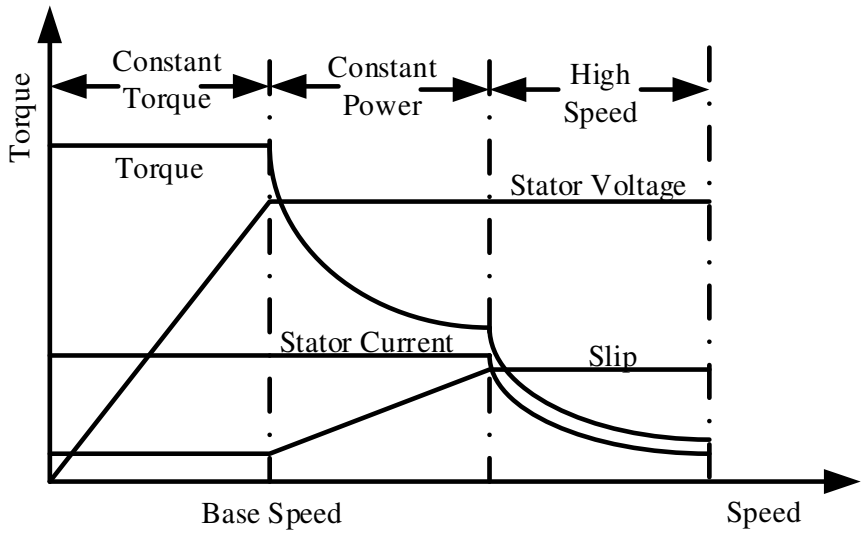

Figure 2.6: Induction motor characteristics

Extended speed range beyond the base speed through the flux weakening operation. Moreover, efficiency at high-speed range may bear in addition to the fact that induction motors efficiency is naturally lower than that of permanent magnet motors due to the absence of rotor winding and rotor copper losses.

In general, induction motor drives were facing a number of disadvantages, which pushed them out from the competition of electrical vehicles electric propulsion. The disadvantages are: low power factor, low efficiency, high losses, and low inverter usage factor, which is more serious for huge power and high speed motor.

The induction motor drives efficiency can be improved through new techniques [60-61]. Some of the proposed control techniques are mainly devoted to electrical vehicle applications [62].

2.2.2 Permanent Magnet Synchronous Motor (PMSM) or Brush Less DC (BLDC) Motor

Permanent magnet synchronous motors are most capable of challenging the induction motors for the electric propulsion of electrical vehicles. These motors have number of advantages, (a) low overall weight and volume for a given output power (high power density), (b) heat efficiently dissipated to surroundings and (c) high efficiency. The Figure 2.7 shows the synchronous motor characteristics, it has a small constant power

region (the fixed permanent magnet limit their extended speed range). In order to increase speed range of permanent magnet synchronous motor (brushless) motor, the conduction angle of the power converter can be controlled at more than the base speed. The speed range may be extended three to four times of the base speed. However, at high-speed range the efficiency may drop, the motor may experience from demagnetization [63]

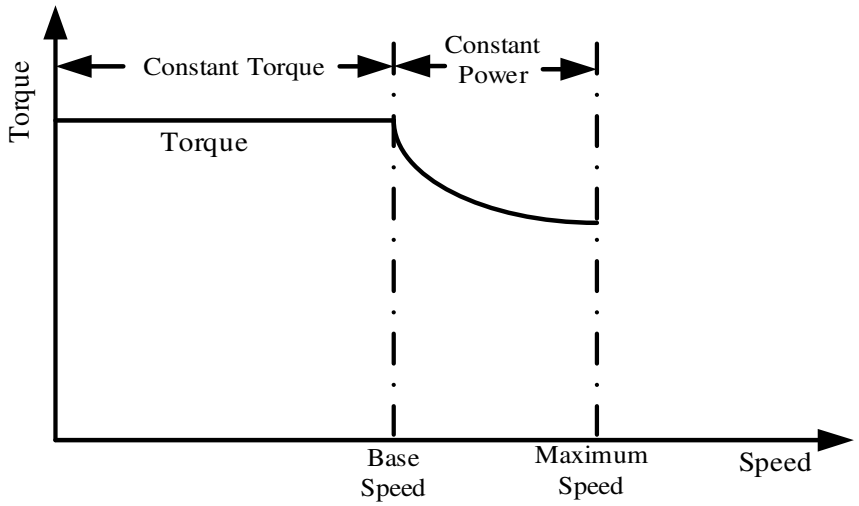

Figure 2.7: PM synchronous motor characteristics

The permanent magnet synchronous motor has different configurations based on the arrangement of the permanent magnet. They can be classified as surface magnet mounted or buried magnet mounted. The surface magnet designs may use small amount magnets, while the buried magnet designs may get higher air-gap flux density. Another configuration is PM hybrid motor; where the air gap magnetic field is get through the combination of field winding and permanent magnet. The PM hybrid motors offer higher overall efficiency and wider speed range but require more complex construction.

2.2.3 Switched Reluctance Motor (SRM)

The switched reluctance motors are gaining much attention now and are accepted to have high potential for electrical vehicle applications. These motors have advantages of simple and rugged construction, fault-tolerant operation, simple control and outstanding torque-speed characteristics as shown in Figure 2.8.

The switched reluctance motors are rewarded with efficient rotor build without any magnetic sources on the rotor, harmoniously providing the torque-speed characteristic suitable for electrical vehicle solicitations and perfect for abrasive atmospheric conditions. The maximization of the machine torque density and lowering the converter cost are not supported due to the requirement of lowering machine torque ripples and generated noise to satisfactory values [64].

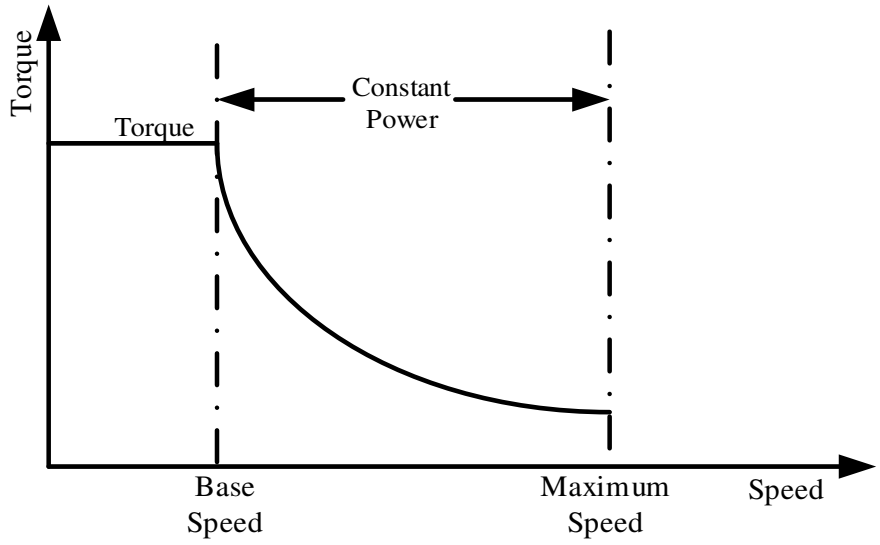

Figure 2.8: SRM characteristics

In spite of being probably the meekest of rotating machines, the drive system of a pragmatic switched reluctance motor is quite complex. The inverter comprises of a fixed number of governable switches whose task is to link the numerous phases to a DC source at suitable intervals as decided by the controller. The switched reluctance motors are different from DC and AC machines in the manner that they are not simply connected to a DC or AC source at the time of operation. Each of the machine phases has to be excited in a proper sequence with currents whose timing has to be cautiously correlated with the location of the rotor poles so as to generate a productive torque.

The extended speed range ability and energy efficiency are among the above-mentioned motor electric propulsion features. However, these two basic characteristics are affected by vehicle dynamics and system architecture. These two characteristics demand special attention on the selection of traction drives for electrical vehicles. Moreover, the issue of extended speed range is significant to a vehicles acceleration performance, which is a

design criteria usually determined by users demand. The issue of energy efficiency of the system becomes important because rarely in real time the vehicle operates in extremes (high speed and acceleration). A conclusion that should be drawn from this analysis is that induction motor is an alternative choice for electrical vehicle. From Table 2.1, the comparative study has revealed that the induction motor is the solution that makes the consensus even if competition remains hard with PM brushless motors [65].

Table 2.1: Electric propulsion systems evaluation

Characteristics	**IM**	**PMSM**	**SRM**
Power Density	3.5	5	3.5
Efficiency	3.5	5	3.5
Controllability	5	4	3
Reliability	5	4	5
Technological maturity	5	4	4
Cost	5	3	4
Total	27	25	23

2.3 Summary

A single-stage power converter, Z-source inverter is explored as a competitive alternative to existing inverter topologies for electrical vehicle, having inherent advantages of voltage buck and boost capabilities.

In the proof-of-concept electrical vehicle system proposed in this thesis, a Squirrel-Cage IM was selected because of its rugged structure, mature manufacturing technology, and low cost. In particular, induction machines can be completely demagnetized, a feature especially useful to avoid over voltage at high speed when system would fail. A conclusion that should be drawn from this analysis is that induction motor is an alternative choice for electrical vehicle.

Chapter - 3

Z-Source Inverter and Induction Motor: Modeling

The electric vehicle drive systems need to operate to a wide range of speeds, therefore buck-boost of voltage with voltage source converter is a choice for power converters in drive systems [66-67]. However, it has limitations those were discussed in Chapter 2. The Z-source inverter is a new topology of power converter, found to be an apt viable option for AC drive applications. This Z-source inverter topology is shown in Figure 3.1. A conventional voltage source inverter output voltage is restricted to $\frac{2}{\pi}V_{dc}$. Whereas theoretically, for a Z-source inverter there is no such voltage limit, thereby granting greater freedom while designing AC converters, which has better performance and lesser cost of operation.

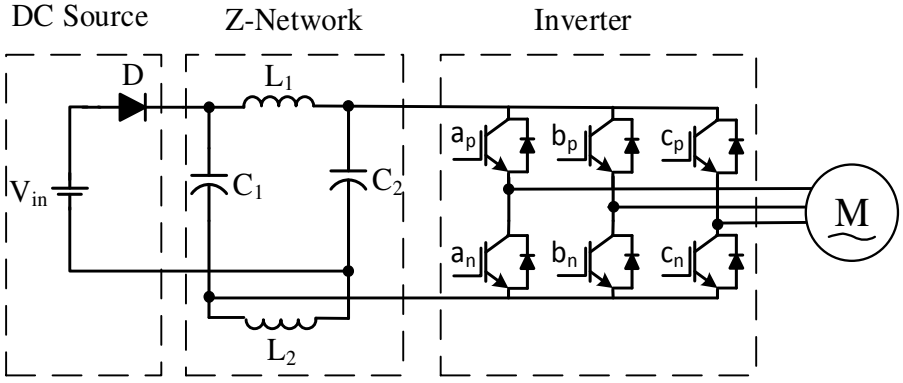

Figure 3.1: Three phase Z-source inverter-feeding to AC motor

Peng [37] proposed a control method for Z-source inverter, which enables it to produce any AC output voltage as per requirement by controlling the shoot through duty cycle. Although, various methods shows that Z-source inverter ensures maximum voltage gain irrespective of modulation index [33]. It is essential to have a detailed analysis of Z-source inverter in order to model proper control for Z-source inverter. A small signal model would give an overview as well as a detailed look into the functioning and the dynamics of the system enabling us to know the limits of the system and design accordingly [68].

This chapter would build up on the steady state model of a Z-source inverter and study the changes brought in by the inductors and capacitors present in the circuit. Here, we shall derive transfer functions for inductive load circuit.

3.1 Small Signal Model of ZSI

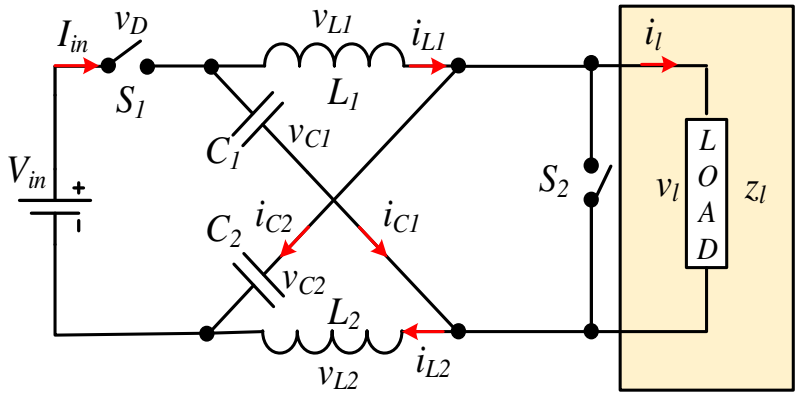

Figure 3.2: Equivalent circuit of Z-source inverter

The small signal model is working in continuous conduction mode (CCM). The Z-source inverter is shown in Figure(s) 3.2, 3.3 and 3.4 depict the working of Z-source inverter under two different modes of operation.

Mode-1: Inverter circuit as shown in Figure 3.3 is operating in one of the seven different ways of shoot-through state. The inverter circuit looks like a 'short circuit' from the DC-link of the inverter. In shoot-through state, the capacitor voltage becomes higher than the input DC voltage, which makes the diode '*D*' reverse biased and voltage does not appears across the load in the zero state. During this mode, there is no power transfer from the source to the load because the load and source sides are decoupled by the shoot-through state and the open switch 'S_1'.

Mode-2: Inverter circuit as shown in Figure 3.4 is operating in one of the six active states and the circuit can be seen as an equivalent current source. During this mode the DC source voltage appears across the inductor and the capacitor, the power transfers from the source to the load through inductor.

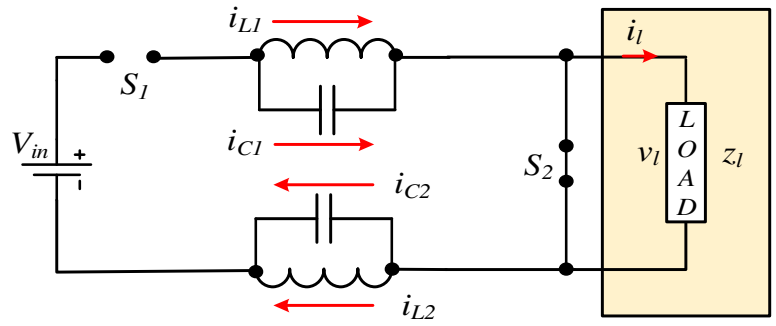

Figure 3.3: Z-source inverter operation mode 1 ('S_1' open and 'S_2' closed)

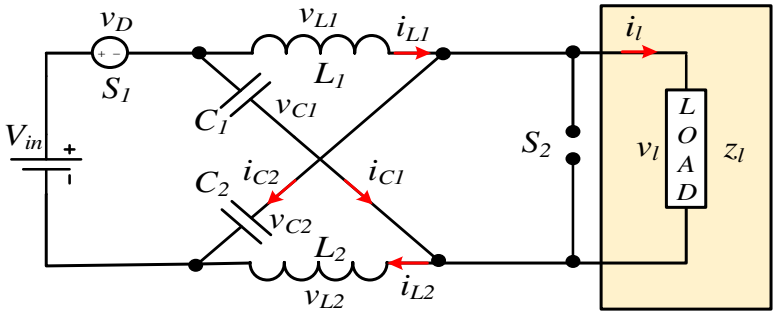

Figure 3.4: Z-source inverter operation mode 2 ('S_2' open and 'S_1' closed)

We make the following assumptions while performing the small signal analysis.

1. The Z-network elements are ideal and lossless.
2. Z-source inverter is working in continuous current conduction mode.
3. The input voltage 'V_{in}' is an independent voltage source. The forward voltage drop of switch 'S_1' is modeled by a fixed voltage drop 'V_D'.
4. As the load impedance is much larger than the on-resistance R_{on} of switch 'S_2', R_{on} is considered to be zero in the modeling and analysis.

3.1.1 Inductive Load

The load current is assumed to be continuous of an inductive load. The state variables are capacitor voltages, inductor currents and load current.

$$X(t) = \begin{bmatrix} i_{L1}(t) \\ i_{L2}(t) \\ v_{C1}(t) \\ v_{C2}(t) \\ i_l(t) \end{bmatrix} \tag{3.1}$$

The input voltage 'V_{in}' is used as ideal voltage source and the load impedance is $Z_l = R_l + sL_l$. In Mode-1, the switch 'S_1' is off and 'S_2' is on (the load is short-circuited by 'S_2'), the circuit equations can be written in state space form,

$$K\dot{x} = A_1 x + B_1 u \tag{3.2}$$

$$\begin{bmatrix} L_1 & 0 & 0 & 0 & 0 \\ 0 & L_2 & 0 & 0 & 0 \\ 0 & 0 & C_1 & 0 & 0 \\ 0 & 0 & 0 & C_2 & 0 \\ 0 & 0 & 0 & 0 & L_1 \end{bmatrix} \frac{d}{dt} \begin{bmatrix} i_{L1}(t) \\ i_{L2}(t) \\ v_{C1}(t) \\ v_{C2}(t) \\ i_l(t) \end{bmatrix} = \begin{bmatrix} 0 & 0 & 1 & 0 & 0 \\ 0 & 0 & 0 & 1 & 0 \\ -1 & 0 & 0 & 0 & 0 \\ 0 & -1 & 0 & 0 & 0 \\ 0 & 0 & 0 & 0 & -R_1 \end{bmatrix} \begin{bmatrix} i_{L1}(t) \\ i_{L2}(t) \\ v_{C1}(t) \\ v_{C2}(t) \\ i_l(t) \end{bmatrix} \tag{3.3}$$

where, $K = \begin{bmatrix} L_1 & 0 & 0 & 0 & 0 \\ 0 & L_2 & 0 & 0 & 0 \\ 0 & 0 & C_1 & 0 & 0 \\ 0 & 0 & 0 & C_2 & 0 \\ 0 & 0 & 0 & 0 & L_1 \end{bmatrix}$, $A_1 = \begin{bmatrix} 0 & 0 & 1 & 0 & 0 \\ 0 & 0 & 0 & 1 & 0 \\ -1 & 0 & 0 & 0 & 0 \\ 0 & -1 & 0 & 0 & 0 \\ 0 & 0 & 0 & 0 & -R_1 \end{bmatrix}$ and $B_1 = \begin{bmatrix} 0 \\ 0 \\ 0 \\ 0 \\ 0 \end{bmatrix}$

Mode-2, the switch 'S_1' is on and 'S_2' is off, then equations can be expresses in state space form.

$$K\dot{x} = A_2 x + B_2 u$$

$$\begin{aligned} &\begin{bmatrix} L_1 & 0 & 0 & 0 & 0 \\ 0 & L_2 & 0 & 0 & 0 \\ 0 & 0 & C_1 & 0 & 0 \\ 0 & 0 & 0 & C_2 & 0 \\ 0 & 0 & 0 & 0 & L_1 \end{bmatrix} \frac{d}{dt} \begin{bmatrix} i_{L1}(t) \\ i_{L2}(t) \\ v_{C1}(t) \\ v_{C2}(t) \\ i_l(t) \end{bmatrix} \\ &= \begin{bmatrix} 0 & 0 & 0 & -1 & 0 \\ 0 & 0 & -1 & 0 & 0 \\ 0 & 1 & 0 & 0 & -1 \\ 1 & 0 & 0 & 0 & -1 \\ 0 & 0 & 1 & 1 & -R_1 \end{bmatrix} \begin{bmatrix} i_{L1}(t) \\ i_{L2}(t) \\ v_{C1}(t) \\ v_{C2}(t) \\ i_l(t) \end{bmatrix} + \begin{bmatrix} 1 \\ 1 \\ 0 \\ 0 \\ -1 \end{bmatrix} \left(V_{in}(t) - V_D\right) \end{aligned} \tag{3.4}$$

where, $A_2 = \begin{bmatrix} 0 & 0 & 0 & -1 & 0 \\ 0 & 0 & -1 & 0 & 0 \\ 0 & 1 & 0 & 0 & -1 \\ 1 & 0 & 0 & 0 & -1 \\ 0 & 0 & 1 & 1 & -R_l \end{bmatrix}$ $B_2 = \begin{bmatrix} 1 \\ 1 \\ 0 \\ 0 \\ -1 \end{bmatrix}$

The duty ratios of 'S_1' and 'S_2' are 'D'' and 'D' respectively. The 'D'' defined as $D' = 1 - D$, where 'D' is shoot-through duty ratio.

Small-signal relationship among the state variables is derived by applying small signal perturbations $\tilde{V}_{in}(t)$ to the input voltage and $\tilde{d}(t)$ to the shoot-through duty ratio of 'S_2' shown by

$$V_{in}(t) = V_{in} + \tilde{V}_{in}(t) \tag{3.5}$$

$$d(t) = D + \tilde{d}(t) \tag{3.6}$$

Here, the drop in forward voltage of switch 'S_1' is modeled as the constant 'V_D'. Alterations in state variables of the small signal are produced due to 'D' in the perturbations,

$$x = X + \tilde{x} \tag{3.7}$$

Using state space averaging method, the averaged matrix 'A' is given by:

$$A = D.A_1 + D'.A_2 \tag{3.8}$$

Similarly,

$$B = D.B_1 + D'.B_2 \tag{3.9}$$

Also, the perturbations are applied at the operation point, at which the DC steady state equations are

$$\begin{bmatrix} 0 \\ 0 \\ 0 \\ 0 \\ 0 \end{bmatrix} = \begin{bmatrix} 0 & 0 & D & -D' & 0 \\ 0 & 0 & -D' & D & 0 \\ -D & -D' & 0 & 0 & -D' \\ D' & -D & 0 & 0 & -D' \\ 0 & 0 & D' & D' & -R_l \end{bmatrix} \begin{bmatrix} i_{L1} \\ i_{L2} \\ v_{C1} \\ v_{C2} \\ i_1 \end{bmatrix} + \begin{bmatrix} D' \\ D' \\ 0 \\ 0 \\ -D' \end{bmatrix} (V_{in} - V_D) \tag{3.10}$$

To obtain small signal state equations, we combine the above equations (3.8) through (3.10)

$$K\dot{\tilde{X}} = A\tilde{X} + B\tilde{U} + (A_1 - A_2)X + (B_1 - B_2)U \tag{3.11}$$

$$\begin{bmatrix} L_1 & 0 & 0 & 0 & 0 \\ 0 & L_2 & 0 & 0 & 0 \\ 0 & 0 & C_1 & 0 & 0 \\ 0 & 0 & 0 & C_2 & 0 \\ 0 & 0 & 0 & 0 & L_1 \end{bmatrix} \frac{d}{dt} \begin{bmatrix} i_{L1}(t) \\ i_{L2}(t) \\ v_{C1}(t) \\ v_{C2}(t) \\ i_l(t) \end{bmatrix} = \begin{bmatrix} 0 & 0 & D & -D' & 0 \\ 0 & 0 & -D' & D & 0 \\ -D & D' & 0 & 0 & -D' \\ D' & -D & 0 & 0 & -D' \\ 0 & 0 & D' & D' & -R_1 \end{bmatrix} \begin{bmatrix} \tilde{i}_{L1}(t) \\ \tilde{i}_{L2}(t) \\ \tilde{v}_{C1}(t) \\ \tilde{v}_{C2}(t) \\ \tilde{i}_l(t) \end{bmatrix} + \begin{bmatrix} D' \\ D' \\ 0 \\ 0 \\ -D' \end{bmatrix} \tilde{V}_{in}(t) + \begin{bmatrix} V_{C1}+V_{C2}-(V_{in}-V_D) \\ V_{C1}+V_{C2}-(V_{in}-V_D) \\ -I_{L1}-I_{L2}+I_1 \\ -I_{L1}-I_{L2}+I_1 \\ -(V_{C1}+V_{C2})+(V_{in}-V_D) \end{bmatrix} \tilde{d}(t) \tag{3.12}$$

where I_{L1}, I_{L2}, V_{C1}, V_{C2}, V_{in} are steady state values at the operation points when small signal perturbations occur.

After Laplace transformation, the above equations become the following:

$$sL_1\tilde{i}_{L1}(s) = D\tilde{v}_{C1}(s) - D'\tilde{v}_{C2}(s) + D'\tilde{v}_{in}(s) + (V_{C1}+V_{C2}-V_{in}+V_D)\tilde{d}(s) \tag{3.13}$$

$$sL_2\tilde{i}_{L2}(s) = -D'\tilde{v}_{C1}(s) + D\tilde{v}_{C2}(s) + D'\tilde{v}_{in}(s) + (V_{C1}+V_{C2}-V_{in}+V_D)\tilde{d}(s) \tag{3.14}$$

$$sC_1\tilde{v}_{C1}(s) = -D\tilde{i}_{L1}(s) + D'\tilde{i}_{L2}(s) + (-I_{L1}-I_{L2}+I_1)\tilde{d}(s) - D'\tilde{i}_l(s) \tag{3.15}$$

$$sC_2\tilde{v}_{C2}(s) = D'\tilde{i}_{L1}(s) - D\tilde{i}_{L2}(s) + (-I_{L1}-I_{L2}+I_1)\tilde{d}(s) - D'\tilde{i}_l(s) \tag{3.16}$$

$$sL_l\tilde{i}_l(s) = D'\tilde{v}_{C1}(s) + D'\tilde{v}_{C2}(s) - D'\tilde{v}_{in}(s) + (V_{in}-V_D-V_{C1}-V_{C2})\tilde{d}(s) - R_l\tilde{i}_l(s) \tag{3.17}$$

The Z-impedance network is symmetric,

$$L_1 = L_2 = L \text{ and } C_1 = C_2 = C.$$

Additionally, we assume a continuous conduction mode of Z-source inverter and $D + D' = 1$.

From the equations (3.13) and (3.14)

$$\tilde{i}_{L1}(t) - \tilde{i}_{L2}(t) = \frac{1}{sL}[\tilde{v}_{C1}(t) - \tilde{v}_{C2}(t)] \tag{3.18}$$

Similarly, combining equations (3.15) and (3.16)

$$sC'[\tilde{v}_{C1}(t) - \tilde{v}_{C2}(t)] = -\frac{1}{sL}[\tilde{v}_{C1}(t) - \tilde{v}_{C2}(t)] \tag{3.19}$$

From equation (3.19)

$$(1+s^2LC)[\tilde{v}_{C1}(t)-\tilde{v}_{C2}(t)]=0 \tag{3.20}$$

The final Laplace transform equation indicates that at any non-oscillatory frequency $\left(i.e.\ \omega \neq \sqrt{\frac{1}{LC}}\right)$

$$\tilde{v}_{C1}(t)=\tilde{v}_{C2}(t)=\tilde{v}_C(t) \tag{3.21}$$

From the equations (3.18) and (3.21)

$$\tilde{i}_{L1}(t)=\tilde{i}_{L2}=\tilde{i}_L(t) \tag{3.22}$$

Finally, above mentioned small signal equations from (3.13) to (3.17) can be summarized as,

$$sL\tilde{i}_l(s)=(D-D')\tilde{v}_C(s)+D'\tilde{v}_{in}(s)+(2V_C-V_{in}+V_D)\tilde{d}(s) \tag{3.23}$$

$$sC\tilde{v}_C(s)=(D'-D)\tilde{i}_L(s)+(-2I_L+I_1)\tilde{d}(s)-D'\tilde{i}_l(s) \tag{3.24}$$

$$sL_l\tilde{i}_L(s)=2D'\tilde{v}_C(s)-D'\tilde{v}_{in}(s)+(-2V_C+V_{in}-V_D)\tilde{d}(s)-R_l\tilde{i}_l(s) \tag{3.25}$$

The condition $I_{L1} = I_{L2} = I_L$ and $V_{C1} = V_{C2} = V_C$ is satisfied by the DC steady state values due to the symmetry in the Z network. The steady state thus assumes the values,

$$V_C=\frac{1-D}{1-2D}(V_{in}-V_D) \tag{3.26}$$

$$I_L=\frac{1-D}{1-2D}I_l \tag{3.27}$$

$$I_l=\frac{V_C}{R_l} \tag{3.28}$$

3.2 Small Signal Equivalent Circuits and Transfer Functions

The small signal models from the previous section are used to derive the transfer function for Z-source inverter in this section.

3.2.1 Inductive Load

The equivalent circuit shown in Figure 3.5 is the small-signal circuit model. The small-signal equivalent circuit is a circuit representative of the derived mathematical model

based on equations (3.23), (3.24), (3.25).

The inductor current loop equation is shown in Figure 3.5(a), the small-signal inductor current $\tilde{i}_L(t)$ is the loop current,

1. The terms $D'\tilde{v}_{in}(t)$ and $(D-D')\tilde{v}_C(t)$ are modeled as dependent sources as they are dependent on other voltages in the Z-source inverter.
2. The term $\tilde{d}(t)(2V_C - V_{in} + V_D)$ is treated as an independent source since it is decided by the duty cycle variations.

In Figure 3.5(b) is the small signal model to the capacitor node,

1. $\tilde{v}_C(t)$ is the voltage of the capacitor.
2. The term $(-2I_L + I_l)\tilde{d}(t)$ is a current source driven by the control variations and is independent.
3. The current sources $(D'-D)\tilde{i}_L(t)$ and $D'\tilde{i}_l(t)$ depend on other currents in the Z-source inverter.

The circuit equivalent to the load loop is shown by Figure 3.5(c),

1. It has the small-signal loop current $\tilde{i}_l(t)$

2. The item $(2V_C - V_{in} + V_{Dl})$ is in dependent on voltages in Z-source inverter or driven by control $\tilde{d}(t)$.

The dependent voltage and current sources appear in the equivalent circuit indicate that strong couplings may exist among the state variables.

In small signal modeling and transient analysis, the response of one state variable to multiple small signal perturbations can be expressed as a linear combination of the variable response to each individual perturbation.

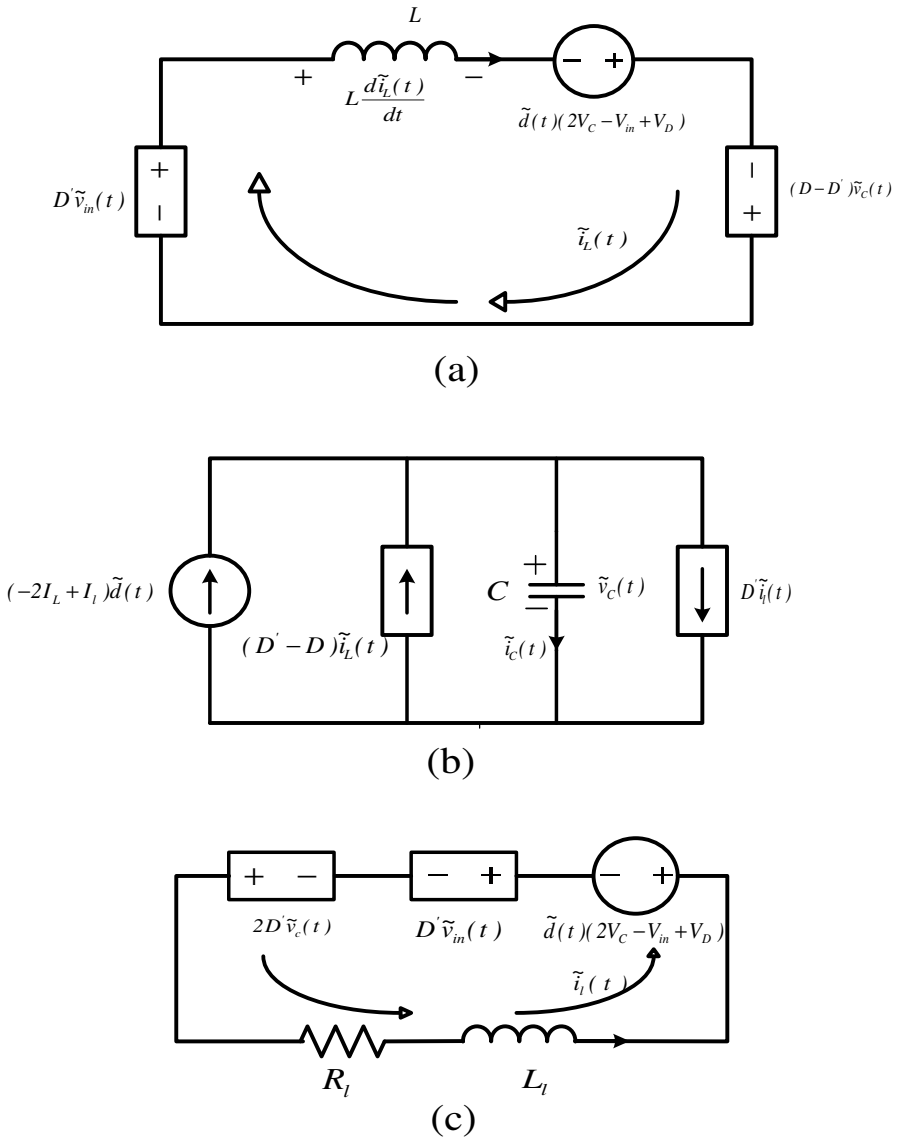

Figure 3.5: Circuit equivalent to small signal AC model: Z-source inverter with inductive load (a) Inductor current loop circuit, (b) Capacitor voltage node circuit, (c) Load current loop circuit

The small signal equivalents for the Z-source network can be derived as,

$$\tilde{v}_C(s) = G_{Vin}\tilde{v}_{in}(s) + G_{vd}\tilde{d}(s) \tag{3.29}$$

$G_{vin}(s) = \left.\frac{\tilde{v}_C(s)}{\tilde{v}_{in}(s)}\right|_{\tilde{d}(s)=0}$ is the input to capacitor voltage transfer function.

$G_{vd}(s) = \left.\frac{\tilde{v}_C(s)}{\tilde{d}(s)}\right|_{\tilde{v}_{in}(s)=0}$ is the control to capacitor voltage transfer function.

From equations (3.23) to (3.25),

$$G_{vin}(s) = \frac{k_1 s + k_2}{k_3 s^3 + k_4 s^2 + k_5 s + k_6} \tag{3.30}$$

and

$$G_{vd}(s) = \frac{k_7 s^2 + k_8 s + k_9}{k_3 s^3 + k_4 s^2 + k_5 s + k_6} \tag{3.31}$$

where the coefficient k_1 through k_9 are given below:

$k_1 = D'(D' - D)L_l + D'^2 L$

$k_2 = D'(D' - D)R_l$

$k_3 = L_l LC$

$k_4 = R_l LC$

$k_5 = 2D'^2 L + L_l (D - D')^2$

$k_6 = R_l (D - D')^2$

$k_7 = (-2I_L + I_l) L_l L$

$k_8 = (-2I_L + I_l) R_l L + (D' - D)(2V_C - V_{in} + V_D) L_l + LD'(2V_C - V_{in} + V_D)$ and

$k_9 = (D' - D)(2V_C - V_{in} + V_D)$

The small signal expressions in terms of the transfer functions become,

$$\tilde{i}_L(s) = \left[\frac{(D - D')G_{vin}(s) + D'}{sL}\right]\tilde{V}_{in}(s) + \left[\frac{(D - D')G_{vd}(s) + (2V_C - V_{in} + V_D)}{sL}\right]\tilde{d}(s) \tag{3.32}$$

The input to inductor current transfer function is,

$$G_{ig}(s) = \left.\frac{\tilde{i}_L(s)}{\tilde{V}_{in}(s)}\right|_{\hat{d}(s)=0} = \frac{(D - D')G_{V\,in}(s) + D'}{sL} \tag{3.33}$$

The control to inductor current transfer function is,

$$G_{id}(s) = \left.\frac{\tilde{i}_L(s)}{\tilde{d}(s)}\right|_{\hat{v}_{in}(s)} = \frac{(D-D')\,G_{vd}(s) + (2V_C - V_{in} + V_D)}{sL} \tag{3.34}$$

The final current transfer functions will be

$$G_{ig}(s) = \frac{k_{10}s^3 + k_{11}s^2 + k_{12}s}{sL(k_3s^3 + k_4s^2 + k_5s + k_6)} \tag{3.35}$$

and

$$G_{id}(s) = \frac{k_{13}s^3 + k_{14}s^2 + k_{15}s}{sL(k_3s^3 + k_4s^2 + k_5s + k_6)} \tag{3.36}$$

where k_{10} through k_{15} are

$k_{10} = D' L_1 LC$

$k_{11} = D' R_1 LC$

$k_{12} = D'^2 L$

$k_{13} = (2\mathrm{V_C} - \mathrm{V_{in}} + \mathrm{V_D})\,\mathrm{L_1LC}$

$k_{14} = R_1 LC(2V_C - Vin + V_D) + (-I_L + I_1)L_1 L(D - D')$ and

$k_{15} = LD'(2V_C - V_{in} + V_D) + (-2I_L + I_1)L_1 L(D - D')$

3.3 Dynamic Modeling of Induction Motor

The speed control of the induction motor is not easier when compared with the DC motors. At light load conditions, the induction motors take large starting currents and operate at a poor lagging power factor. The 3-phase induction machine with a balance input voltage can be evaluated by single-phase equivalent circuit. In the steady state mode, the per-phase equivalent circuit of the induction motor is given in fundamental frequency. The simplified per-phase equivalent circuit model of the machine provides good performance prediction for steady state operation of the machine with sinusoidal supply voltages. But, it fails to give a good model for dynamic performance [69]. In an adjustable speed drives, the machine normally constituted as element within a feedback loop, and therefore its transient behavior has to be taken into consideration. Hence, an accurate dynamic model of the

induction motor is necessary which can explain the dynamic behavior of the machine under both transient and steady state conditions.

3.3.1 Voltage Equations in Machine Variables

An idealized three phase induction machine can be considered as a transformer with moving secondary windings where coupling coefficients are variables changing with the rotor position.

The voltage equations in machine variables can be written as.

$$v_{abcs} = r_s i_{abcs} + \frac{d}{dt}\lambda_{abcs} \tag{3.37}$$

$$v_{abcr} = r_r i_{abcr} + \frac{d}{dt}\lambda_{abcr} \tag{3.38}$$

where,

V_{abcs} is the stator voltages,

V_{abcr} is the rotor voltages,

λ_{abcs} is the stator flux linkages and

λ_{abcr} is the rotor flux linkages.

The 's' and '*r*' subscripts denote variables associated with stator and rotor windings respectively.

The flux linkage equations then become

$$\begin{bmatrix} \lambda_{abcs} \\ \lambda_{abcr} \end{bmatrix} = \begin{bmatrix} L_s & L_{sr} \\ L_{sr}^T & L_r \end{bmatrix} \begin{bmatrix} i_{abcs} \\ i_{abcr} \end{bmatrix} \tag{3.39}$$

The winding inductances of the induction machine are

$$L_s = \begin{bmatrix} L_{ls} + L_{ms} & -\frac{1}{2}L_{ms} & -\frac{1}{2}L_{ms} \\ -\frac{1}{2}L_{ms} & L_{ls} + L_{ms} & -\frac{1}{2}L_{ms} \\ -\frac{1}{2}L_{ms} & -\frac{1}{2}L_{ms} & L_{ls} + L_{ms} \end{bmatrix} \tag{3.40}$$

L_{mr} is the rotor magnetizing inductance, and with this notation the rotor inductance relationship could be expressed by the following equations

$$L_r = \begin{bmatrix} L_{lr} + L_{mr} & -\frac{1}{2}L_{mr} & -\frac{1}{2}L_{mr} \\ -\frac{1}{2}L_{mr} & L_{lr} + L_{mr} & -\frac{1}{2}L_{mr} \\ -\frac{1}{2}L_{mr} & -\frac{1}{2}L_{mr} & L_{lr} + L_{mr} \end{bmatrix} \tag{3.41}$$

and

$$L_{sr} = L_{sr} \begin{bmatrix} \cos\theta_r & \cos(\theta_r + \frac{2\pi}{3}) & \cos(\theta_r - \frac{2\pi}{3}) \\ \cos(\theta_r - \frac{2\pi}{3}) & \cos\theta_r & \cos(\theta_r + \frac{2\pi}{3}) \\ \cos(\theta_r + \frac{2\pi}{3}) & \cos(\theta_r - \frac{2\pi}{3}) & \cos\theta_r \end{bmatrix} \tag{3.42}$$

where,

L_{ms} is the stator magnetizing inductance,

L_{mr} is the rotor magnetizing inductance,

L_{ls} is the stator leakage inductance,

L_{lr} is the rotor leakage inductance, and

L_{sr} is the mutual inductances between the stator and rotor windings.

The above voltage equations could be used to describe machine dynamics. However, it is still inconvenient because of the time varying inductances. The transformations could be simply assigning the rotating speed of the reference frame, the so-called arbitrary reference frame. If the rotating speed of the reference frame is zero, it is called stationary reference frame. Likewise, if the rotating speed of the reference frame is equal to synchronous speed, it is called synchronously rotating reference frame.

The Figure 3.6 displays the reference frames including the 3-phase variables of the stationary circuit and arbitrary reference frame.

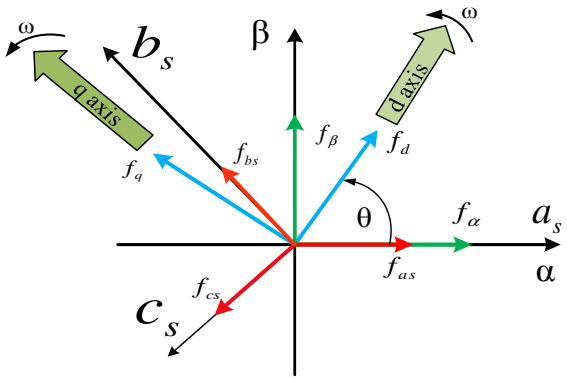

Figure 3.6: Reference frames

The transformation from a three phase stationary circuit to two phase arbitrary reference frame is:

$$f_{qd0} = T(\theta) F_{abcs} \tag{3.43}$$

$$T(\theta) = \frac{2}{3}\begin{bmatrix} \cos\theta & \cos(\theta - \frac{2\pi}{3}) & \cos(\theta - \frac{4\pi}{3}) \\ -\sin\theta & -\sin(\theta - \frac{2\pi}{3}) & -\sin(\theta - \frac{4\pi}{3}) \\ \frac{1}{2} & \frac{1}{2} & \frac{1}{2} \end{bmatrix} \tag{3.44}$$

and

$$T^{-1}(\theta)\begin{bmatrix} \cos\theta & -\sin\theta & 1 \\ \cos(\theta - \frac{2\pi}{3}) & -\sin(\theta - \frac{2\pi}{3}) & 1 \\ \cos(\theta - \frac{4\pi}{3}) & -\sin(\theta - \frac{4\pi}{3}) & 1 \end{bmatrix} \tag{3.45}$$

If the transformations are between the abc and the stationary reference frame, simply $\omega = 0$.

$$T_{abc \to \alpha\beta 0} = T(0) = \frac{2}{3}\begin{bmatrix} 1 & -\frac{1}{2} & -\frac{1}{2} \\ 0 & \frac{\sqrt{3}}{2} & -\frac{\sqrt{3}}{2} \\ \frac{1}{2} & \frac{1}{2} & \frac{1}{2} \end{bmatrix} \tag{3.46}$$

$$T^{-1}_{abc \to \alpha\beta 0} = T^{-1}(0) = \begin{bmatrix} 1 & 0 & 1 \\ -\frac{1}{2} & \frac{\sqrt{3}}{2} & 1 \\ -\frac{1}{2} & -\frac{\sqrt{3}}{2} & 1 \end{bmatrix} \tag{3.47}$$

Transformations between stationary frame and arbitrary reference frame are:

$$\begin{bmatrix} f_d \\ f_q \\ 0 \end{bmatrix} = \begin{bmatrix} \cos\theta & \sin\theta & 0 \\ -\sin\theta & \cos\theta & 0 \\ 0 & 0 & 1 \end{bmatrix} \begin{bmatrix} f_\alpha \\ f_\beta \\ f_0 \end{bmatrix} = T_{\alpha\beta 0 \to qd0}(\theta) \begin{bmatrix} f_\alpha \\ f_\beta \\ f_0 \end{bmatrix} \tag{3.48}$$

and

$$\begin{bmatrix} f_\alpha \\ f_\beta \\ f_0 \end{bmatrix} = \begin{bmatrix} \cos\theta & -\sin\theta & 0 \\ \sin\theta & \cos\theta & 0 \\ 0 & 0 & 1 \end{bmatrix} \begin{bmatrix} u_d \\ u_q \\ u_0 \end{bmatrix} = T^{-1}_{\alpha\beta 0 \to qd0}(\theta) \begin{bmatrix} u_d \\ u_q \\ u_0 \end{bmatrix} \tag{3.49}$$

3.3.2 Dynamic d-q Model

Transformations from 'abc' to an arbitrary reference frame:

$$T(\theta) v_{abcs} = T(\theta) r_s T^{-1}(\theta) i_{dq0s} + T(\theta) \frac{d}{dt}[T^{-1}(\theta) \lambda_{qd0s}] \tag{3.50}$$

where, $T(\theta)r_s T^{-1}(\theta) = r_s$

and $T(\theta)\frac{d}{dt}[T^{-1}\ \lambda_{qd0s}] = T(\theta)\frac{d}{dt}[T^{-1}(\theta)]\lambda_{qd0s} + T(\theta)T^{-1}(\theta)\frac{d}{dt}\lambda_{qd0z}$

$$T(\theta)\frac{d}{dt}[T^{-1}(\theta)] = \omega\begin{bmatrix}0 & -1 & 0\\ 1 & 0 & 0\\ 0 & 0 & 0\end{bmatrix} \tag{3.51}$$

Therefore, the stator voltage equations in arbitrary reference frame are expressed as

$$\begin{bmatrix}V_{ds}\\ V_{qs}\end{bmatrix} = R_s\begin{bmatrix}1 & 0\\ 0 & 1\end{bmatrix}\begin{bmatrix}l_{ds}\\ l_{qs}\end{bmatrix} + \omega\begin{bmatrix}0 & -1\\ 1 & 0\end{bmatrix}\begin{bmatrix}\lambda_{ds}\\ \lambda_{qs}\end{bmatrix} + \frac{d}{dt}\begin{bmatrix}\lambda_{ds}\\ \lambda_{qs}\end{bmatrix} \tag{3.52}$$

The rotor voltage equations derived for the dynamic model of the squirrel cage induction motor, in an arbitrary reference frame can be expressed by

$$v_{ds} = R_s i_{ds} + \frac{d\lambda_{ds}}{dt} - \omega\lambda_{qs} \tag{3.53}$$

$$v_{qs} = R_s i_{qs} + \frac{d\lambda_{qs}}{dt} - \omega\lambda_{ds} \tag{3.54}$$

$$R_r i_{dr} + \frac{d\lambda_{dr}}{dt} - (\omega - \omega_r)\lambda_{qr} = 0 \tag{3.55}$$

$$R_r i_{qr} + \frac{d\lambda_{qr}}{dt} + (\omega - \omega_r)\lambda_{dr} = 0 \tag{3.56}$$

and we have

$$\lambda_{ds} = (L_m + L_{ls})i_{ds} + L_m i_{dr} = L_s i_{ds} + L_m i_{dr} \tag{3.57}$$

$$\lambda_{qs} = (L_m + L_{ls})i_{qs} + L_m i_{qr} = L_s i_{qs} + L_m i_{qr} \tag{3.58}$$

$$\lambda_{dr} = (L_m + L_{lr})i_{dr} + L_m i_{ds} = L_r i_{dr} + L_m i_{ds} \tag{3.59}$$

$$\lambda_{qr} = (L_m + L_{lr})i_{qr} + L_m i_{qs} = L_r i_{qr} + L_m i_{qs} \tag{3.60}$$

The torque equation is:

$$T_e - T_L = J\frac{d\omega_m}{dt} = \frac{2}{P}J\frac{d\omega_r}{dt} \tag{3.61}$$

where,

ω and ω_r are rotating speed of reference frame and rotor rotating speed;

i_{ds} and i_{qs} are d- and q-axis stator currents;

λ_{ds} and λ_{qs} are the d and q-axis stator flux linkages;

R_s and R_r are stator and rotor resistances;

L_m, L_s and L_r are magnetizing stator and rotor inductance; and

T_l and T_e are load torque and electromagnetic torque.

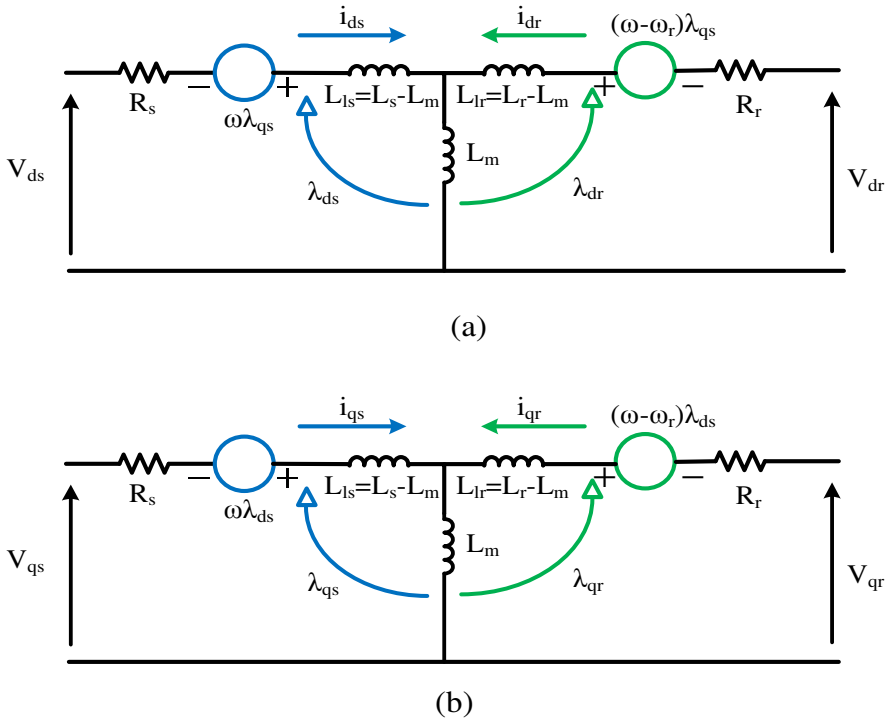

Figure 3.7: Dynamic d-q equivalent circuit: (a) d-axis circuit, (b) q-axis circuit

The equivalent circuits Figure 3.7(a) and Figure 3.7(b) are in arbitrary reference frame that the equations (3.53) to (3.56).

The dynamic q-d models can be launched by defining different rotating speeds for the reference frame. For example,

If the rotating speed of the reference frame is zero ($\omega = 0$), the dynamic q-d model in stationary reference frame is obtained.

If the rotating speed of the reference frame is synchronous speed ($\omega = \omega_c$), the dynamic model is obtained in a synchronous rotating reference frame.

The equations (3.53) to (3.60) we get the following matrix expression,

$$\begin{bmatrix} \dot{i}_{\alpha s} \\ \dot{i}_{\beta s} \\ \dot{\lambda}_{\alpha r} \\ \dot{\lambda}_{\beta r} \end{bmatrix} = \begin{bmatrix} \frac{-1}{\sigma L_s}(R_s + \frac{L_m^2}{L_r T_r}) & 0 & \frac{1}{\sigma L_s}\frac{L_m}{L_r}\frac{1}{T_r} & \omega_r \frac{1}{\sigma L_s}\frac{L_m}{L_r} \\ 0 & \frac{-1}{\sigma L_s}(R_s + \frac{L_m^2}{L_r T_r}) & -\omega_r \frac{1}{\sigma L_s}\frac{L_m}{L_r} & \frac{1}{\sigma L_s}\frac{L_m}{L_r}\frac{1}{T_r} \\ \frac{L_m}{T_r} & 0 & \frac{-1}{T_r} & -\omega_r \\ 0 & \frac{L_m}{T_r} & \omega_r & \frac{-1}{T_r} \end{bmatrix} \begin{bmatrix} i_{\alpha s} \\ i_{\beta s} \\ \lambda_{\alpha r} \\ \lambda_{\beta r} \end{bmatrix} + \frac{1}{\sigma L_s} \begin{bmatrix} v_{\alpha s} \\ v_{\beta s} \\ 0 \\ 0 \end{bmatrix} \tag{3.62}$$

where ,

$$\sigma = 1 - \frac{L_m^2}{L_r L_s} \quad \text{and } T_r = \frac{L_r}{R_r}$$

Doing the same analysis for a synchronous rotating reference frame, the matrix equation now looks like

$$\begin{bmatrix} i^e_{ds} \\ i^e_{qs} \\ \lambda^e_{dr} \\ \lambda^e_{qr} \end{bmatrix} = \begin{bmatrix} \frac{-1}{\sigma L_s}(R_s + \frac{L_m^2}{L_r T_r}) & \omega_e & \frac{1}{\sigma L_s}\frac{L_m}{L_r}\frac{1}{T_r} & \omega_r \frac{1}{\sigma L_s}\frac{L_m}{L_r} \\ -\omega_e & \frac{-1}{\sigma L_s}(R_s + \frac{L_m^2}{L_r T_r}) & -\omega_r \frac{1}{\sigma L_s}\frac{L_m}{L_r} & \frac{1}{\sigma L_s}\frac{L_m}{L_r}\frac{1}{T_r} \\ \frac{L_m}{T_r} & 0 & \frac{-1}{T_r} & \omega_e - \omega_r \\ 0 & \frac{L_m}{T_r} & -(\omega_e - \omega_r) & \frac{-1}{T_r} \end{bmatrix} \begin{bmatrix} i^e_{ds} \\ i^e_{qs} \\ \lambda^e_{dr} \\ \lambda^e_{qr} \end{bmatrix} + \frac{1}{\sigma L_s} \begin{bmatrix} v^e_{ds} \\ v^e_{qs} \\ 0 \\ 0 \end{bmatrix} \tag{3.63}$$

The above induction motor model is used in vector control of induction motor drive.

3.4 Vector Control

It is very important to choose a specific conformation of the field/flux positioning of induction motors which is appropriate and supportive for a highly effective drive. The two fundamental methods in achieving field orientation are direct field orientation and indirect field orientation. Additionally, the synchronous reference structure could be brought in line with an air gap, a stator or a rotor flux [70]. This section will deals only with the indirect rotor field orientation (IRFO) control of induction motor.

3.4.1 Indirect Rotor Field Orientation

This technique is one of the oldest and was proposed in the late 1960s [71]. It is based on imposing the required slip into the machine so that rotor field orientation is forced using rotor flux and stator currents as state variables, and assuming a synchronous frame of reference aligned with the rotor flux ($\lambda_{qr} = 0$),

$$v_{ds} = R_s i_{ds} + \sigma L_s p i_{ds} - \omega_e \sigma L_s i_{qs} + \frac{L_0}{L_r} p\lambda_{dr} \tag{3.64}$$

$$v_{qs} = R_s i_{qs} + \sigma L_s p i_{qs} + \omega_e \sigma L_s i_{ds} + \frac{L_0}{L_r} p\lambda_{ds} \tag{3.65}$$

$$\lambda_{dr} = \frac{L_0 i_{ds}}{1 + T_r p} \tag{3.66}$$

$$\omega_{sl} = \frac{L_0 R_r}{L_r \lambda_{dr}} i_{qs} \tag{3.67}$$

The above equations can be simplified by considering operation below base speed at constant flux ($p\lambda_{rd} = 0$) to,

$$v_{ds} = R_s i_{ds} + \sigma L_s p i_{ds} - \omega_e \sigma L_s i_{qs} \tag{3.68}$$

$$v_{qs} = R_s i_{qs} + \sigma L_s p i_{qs} + \omega_e \sigma L_s i_{ds} \tag{3.69}$$

$$\lambda_{dr} = L_0 i_{ds} \tag{3.70}$$

$$\omega_{sl} = \frac{i_{qs}}{T_r i_{ds}} \tag{3.71}$$

The equation (3.71) gives us a mathematical condition for the slip that should be employed to force field orientation in the machine. The flux angle is obtained by integration of the electrical speed that in turn is obtained by adding the calculated slip and the measured rotor speed. This is described in Figure 3.8.

This method employs quick current loops for the machine to appear having been fed with current and thus the stator dynamics could be ignored. The large bandwidth of the current controllers is facilitating the usage of the reference currents in place of the ones measured for calculation of the machine slip.

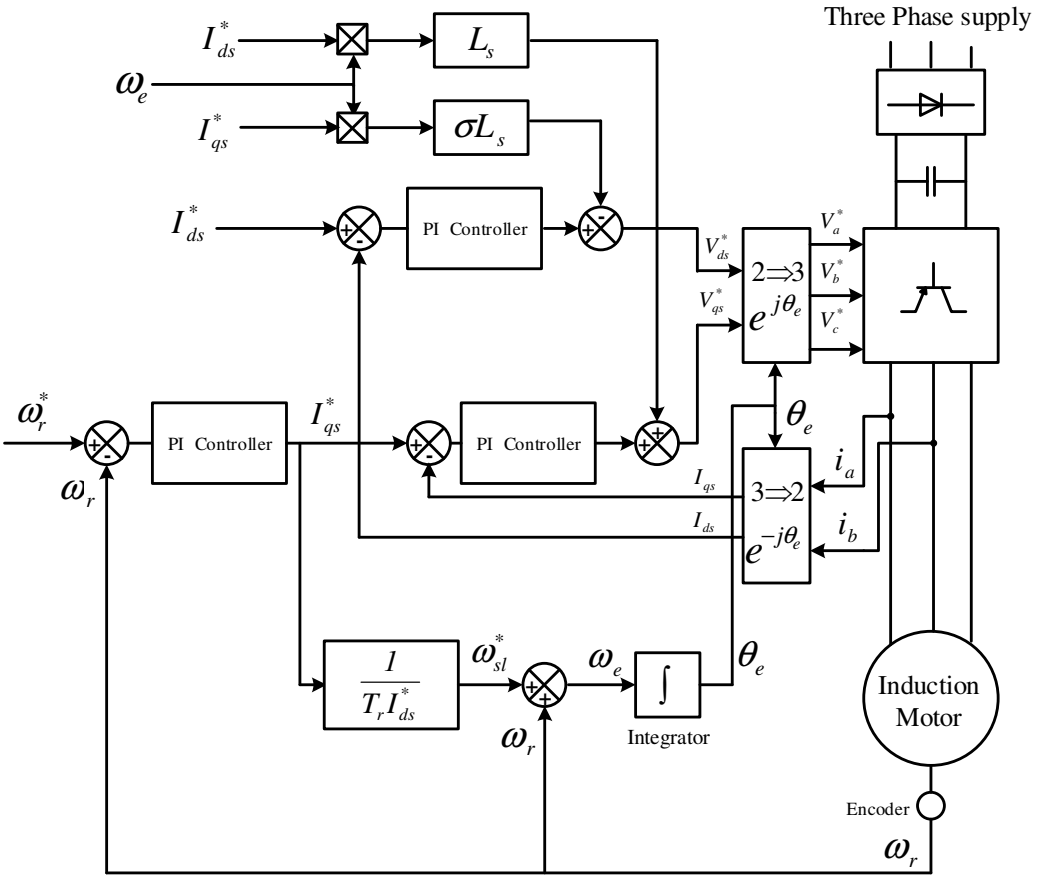

Figure 3.8: Indirect rotor flux orientation implementation

Proper field orientation depends entirely on rotor time constant and equation (3.66) proves independency of the rotor flux from the q-axis current. This method is very efficient due to the deployment of basic techniques of adaptation of the rotor time constant. The IRFO can be employed at a still state due to the dissociation of field orientation from rotational speed. A large bandwidth of the current controller aids in providing a decent torque response for the system. Total decoupling is achieved and hence, big changes in 'i_{qs}' at the time of transients will not alter the flux.

The performance of the IRFO with field weakening is quite poor. The equation $\lambda_{dr} = L_0 i_{ds}$ will not hold true when $_{rd}$ does not remain constant. Hence, the slip in the machine has to be computed using equation (3.67) instead of equation (3.71). Here, field orientation is not entirely dependent on 'T_r', but also on L_0 and 'λ_{dr}'. Since these three quantities vary greatly due to saturation effects [72], it is difficult to keep good filed orientation during field weakening.

3.5 Summary

In this chapter, the study of dynamic behavior of the Z-source inverter, induction motor under transient and steady state conditions was made, appropriate mathematical models of the induction motor was developed in the stationary reference frame by using d-q reference frame theory. Moreover, d-q modeling approach used for the practical implementation of indirect rotor field orientation controlled induction motor drives.

Chapter - 4

Pulse Width Modulation Schemes for Z-Source Inverter

Many pulse width modulation (PWM) control methods (e.g. SPWM, SVPWM) are being in used in voltage source inverters. The voltage source inverter has six active states and two null/zero states. In addition to these states one new state is also created which is called shoot-through state. In this state, the load terminals are shorted through the either lower or upper switches. The Z-source inverter has seven shoot-through states n representing the short-circuiting of one phase-leg, two phase-legs or all three phase-legs. These shoot through states again boost the DC-link voltage and can partially supplement the null states within a fixed switching cycle without altering the normalized volt sec average. Since both states similarly short-circuit the inverter three-phase output terminals, producing zero voltage across the load. Therefore, the shoot-through states can be inserted to existing pulse width modulation state patterns of a conventional voltage source inverter to derive different modulation strategies for controlling a three-phase-leg Z-source inverter.

The shoot-through states can be inserted to existing pulse width modulation state patterns of a conventional voltage source inverter to derive different modulation strategies for controlling a three-phase-leg Z-source inverter.

4.1 Simple Boost Control

The traditional pulse width modulation control is shown in Figure 4.1. The traditional pulse width modulation control is three phases, where the three reference signals 'V_a', 'V_b', and 'V_c' are sinusoidal. The frequency of the triangular carrier signal is significantly higher than that of the reference signals. So, during one cycle of the carrier signal the reference signals can be safely approximated as straight lines [27].

The control of inverter depends on the comparison of reference signals with carrier signal. Whenever reference signals 'V_a', 'V_b', and 'V_c' are higher than carrier signal, the control for switch 1, 3 and 5 is logic-on and whenever the reference signals 'V_a', 'V_b', and 'V_c' are lower than the carrier signal, the control for the switch 1, 3 and 5 is logic-off. The control for the switches 2, 4 and 6 is just the inversion of the switches 1, 3 and 5.

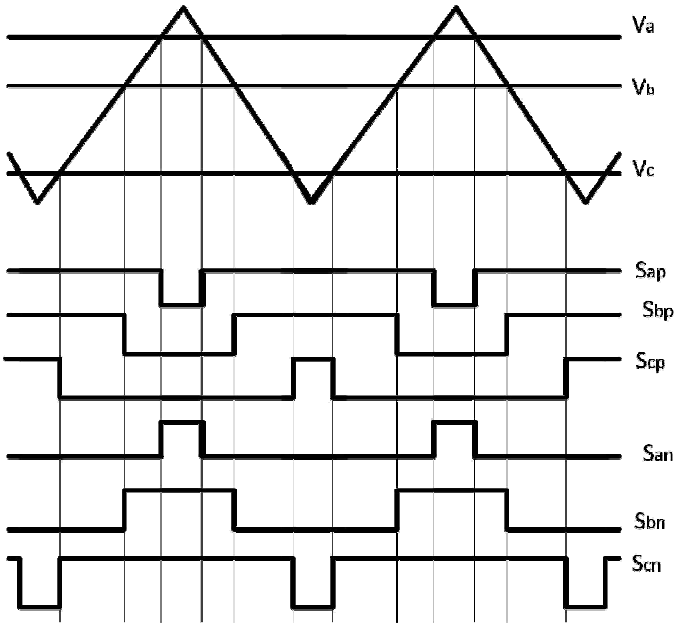

Figure 4.1: Switching pulses from conventional pulse width modulation technique

If the desired AC voltage requirement is met by the DC voltage, the traditional pulse width modulation is used. But in cases where the DC voltage is not high enough to generate the desired output voltage, a modified pulse width modulation technique is used to boost voltage by introducing shoot through as shown in Figure 4.2. As shown in Figure 4.1, the zero state is when all of the upper (or lower) switches are gated off simultaneously creating zero voltage across the load.

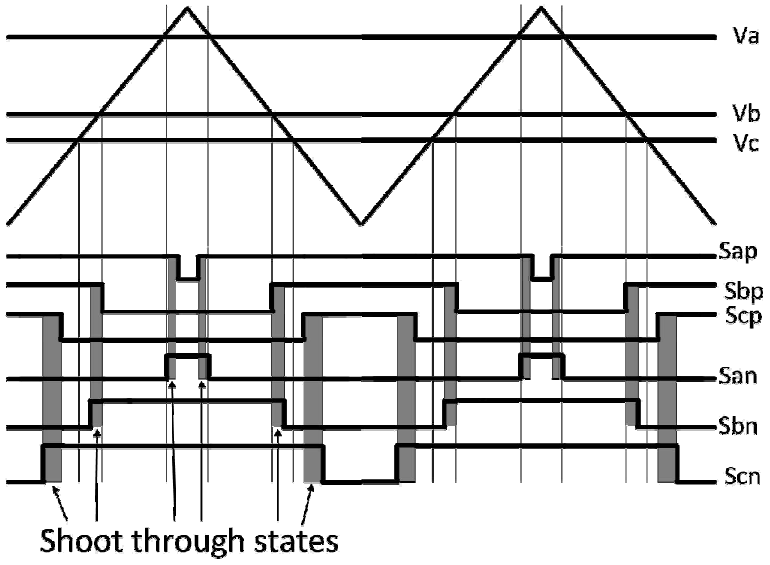

Figure 4.2: Modified pulse width modulation with shoot-through zero states

Introducing the shoot through will obviously create zero voltage across the load, therefore the shoot through does not change the operation of the pulse width modulation. From Figure 4.2, it can be inferred that the shoot through is created by turning on both the switches in any phase leg, where both control signals 'S_{ap}' and 'S_{an}' are both logic-high. The shoot through is applied to the zero states and as a result this will not alter the pulse width modulation as there is no change in voltage across the load. This shoot through period is equally divided into each phase. For a complete switching period, 'T_s' is total switching period, 'T_{sh}' is the zero state time period and 'D_{sh}' is the shoot-through duty ratio.

$$B = \frac{1}{1-2D_{sh}} = \frac{1}{1-2\frac{T_{sh}}{T_s}} \tag{4.1}$$

Voltage gain (G) of the inverter is,

$$G = \frac{\hat{v}_{ac}}{\frac{v_{in}}{2}} \tag{4.2}$$

Where 'V_{ac}' is AC output voltage and 'V_{in}' is input DC voltage. The voltage gain of the inverter with the simple boost control can be written as,

$$G = m \times B = \frac{\hat{v}_{ac}}{\frac{v_{in}}{2}} = \frac{m}{2m-1} \tag{4.3}$$

Then the modulation index can be related with the voltage gain of the inverter as,

$$m = \frac{G}{2G-1} \tag{4.4}$$

The voltage stress across the power switches can be,

$$V_s = B \times V_{in} = (2G-1)V_{in} \tag{4.5}$$

The simple boost control method employs two straight envelops equal to or greater than the peak value of the three phase sinusoidal reference signals to control shoot-through duty ratio in a traditional sinusoidal PWM. The circuit is in shoot through state when the high frequency triangular carrier is greater than the upper straight line envelope or lesser than the lower straight line envelope. In this method the voltage stress across the switches is quite high, which restrict the obtainable voltage gain because of the limitation of device voltage rating. As during shoot through all the switches are ON, switching losses are high.

4.2 Maximum Boost Control

Maximum boost control turns all traditional zero states into shoot-through state, as shown in Figure 4.3. The voltage stress across the switching devices is greatly reduced by fully utilizing the zero states. Indeed, turning all zero states into shoot-through state can minimize the voltage stress; however, a shoot-through duty ratio varying in a line cycle, which causes inductor current ripple, this will require a high inductance for low frequency or variable-frequency applications.

Maximum boost control method maintains the six active states unchanged and turns all zero states into shoot-through zero states. Thus maximum shoot-through time 'T_{sh}' and boosting 'B' are obtained for given modulation index 'm', without distorting the output waveform. Reducing the voltage stress under a desired voltage gain now becomes important to the control of Z-source inverter. As analyzed in simple boost control method, the voltage gain is defined as '$m \times B$' and the voltage stress across the switches is '$B \times V_{dp}$'. Therefore, to minimize the voltage stress for any given voltage gain, we have to minimize `B' and maximize 'm', with the restriction that their product is the desired value. On the other hand, we should maximize 'B' for given modulation index to achieve the maximum voltage gain. Consequently, from the above discussion, we have to make the shoot-through duty ratio as large as possible [32].

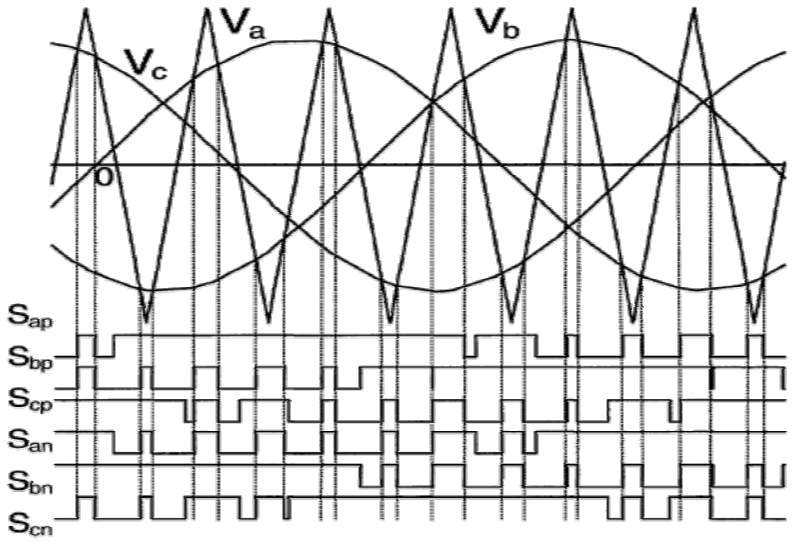

Figure 4.3: Maximum boost control strategy

It can be seen from Figure 4.3, the circuit is in shoot through state when the triangular carrier wave is either greater than the maximum curve of the references (V_a, V_b and V_c) or smaller than the minimum of the references.

$$B = \frac{1}{1-2D_{sh}} = \frac{1}{1-2\frac{T_{sh}}{T_s}} \tag{4.6}$$

$$D_{sh} = \frac{2\pi - 3\sqrt{3}\pi}{2\pi} \tag{4.7}$$

The maximum shoot-through duty ratio can be written as,

$$m = \frac{\pi G}{3\sqrt{3}G - \pi} \tag{4.8}$$

From the above equation we get the voltage stress on the switch as,

$$V_s = B \times V_{dp} = \frac{\pi}{3\sqrt{3}G - \pi} V_{dp} \tag{4.9}$$

This increases the shoot through duty ratio to maximum which raises the boost factor achieved for a specific modulation index without disturbing the output waveform. The possible range of operation for this technique is much wider than the simple control method. This allows a greater modulation index that can be used corresponding to any given voltage which reduces the voltage stress across the switches. The third harmonic injection can be used in three-phase inverter systems to widen the range for the modulation index as shown in Figure 4.4. An increase in modulation index will result in higher voltage gain. A maximum modulation index of $m = \frac{2}{\sqrt{3}}$ can be achieved at 1/6 of third harmonic injection. This increase in modulation index corresponds to a greater voltage gain range. Though the third harmonic injection does not create any voltage stress reduction, it allows for greater voltage gain.

This method turns all the zero states into shoot through state thus minimizing the voltage stress across the switches. However it causes shoot through duty ratio to vary in each cycle, thus increasing the ripple content in inductor current. When the output frequency is low, the inductor ripple becomes significant and a large inductor is required. This increases the cost and size of the circuit.

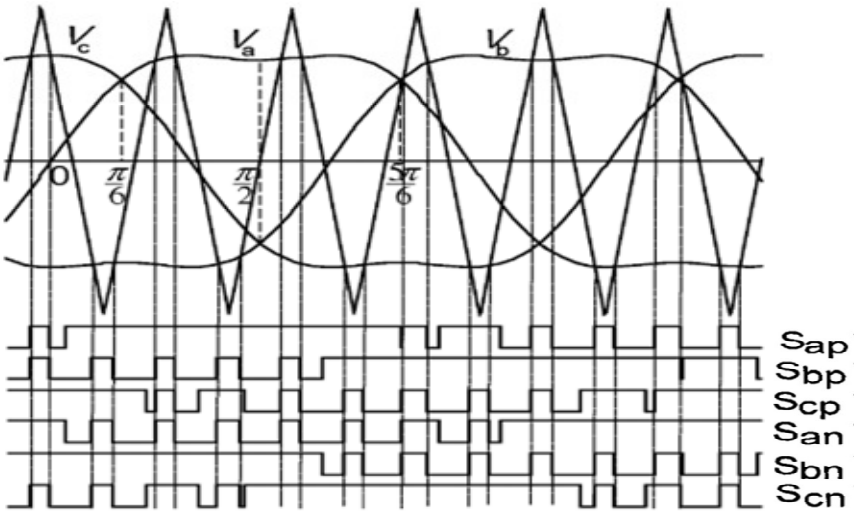

Figure 4.4: Maximum boost control with third harmonic injection strategy

4.3 Maximum Constant Boost Control

The maximum constant boost control technique is employed to attain the highest possible voltage gain while keeping the boost level constant as seen from the Z-source system. This control has the added advantage of not producing low-frequency ripple related to the output frequency [33]. This method can also significantly lower the inductance and capacitance requirements of the Z-source network. Figure 4.5 shows the generation of switching pulses by maximum constant boost control method, which achieves the maximum voltage gain while always keeping the shoot-through duty ratio constant.

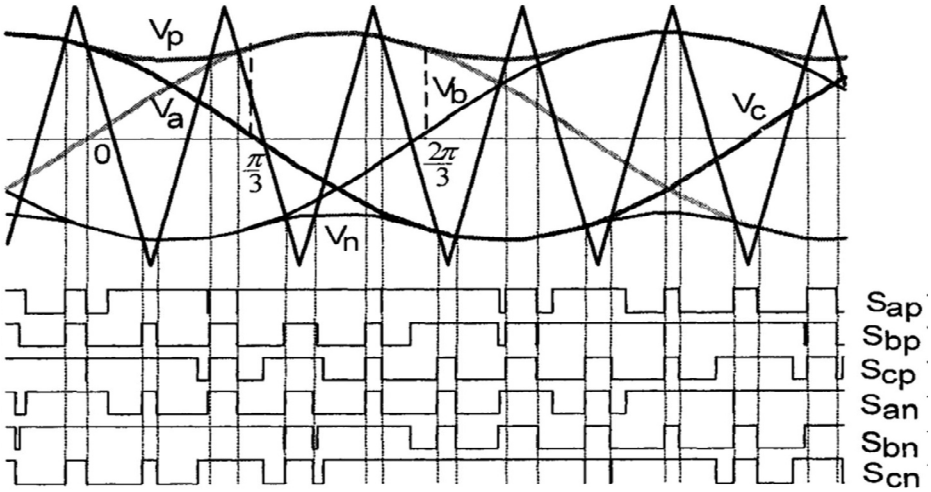

Figure 4.5: Maximum constant boost control strategy

There are five modulation curves used in this method, three reference signals 'V_a', 'V_b', and 'V_c' and two so called shoot-through envelope signals, 'V_p' and 'V_n'. The two envelope curves are periodical and have a frequency that is thrice that of the output. The shoot through zero state is implemented, when the carrier triangle wave is above the upper shoot through envelope 'V_p' or beneath the lower shoot-through envelope 'V_n'. The intermediate stages remain exactly the same as in the conventional carrier-based pulse width modulation technique. The shoot-though duty cycle which determines the boost factor, must be kept uniform so as to maintain a constant boost factor. The basic motive here is to maximize the boost factor while keeping it constant throughout.

The shoot through duty ratio is,

$$D_{sh} = \frac{2-\sqrt{3}m}{2} = 1 - \frac{\sqrt{3}m}{2} \tag{4.10}$$

$$B = \frac{1}{1-2\frac{T_{sh}}{T}} - \frac{1}{\sqrt{3}m-1} \tag{4.11}$$

The voltage gain can be expressed as,

$$G = m \times B = \frac{m}{\sqrt{3}m-1} \tag{4.12}$$

The voltage stress across the device can be,

$$V_s = B \times V_{dp} = (\sqrt{3}G - 1)V_{dp} \tag{4.13}$$

The method can be realized using third harmonic injection in Figure 4.6.

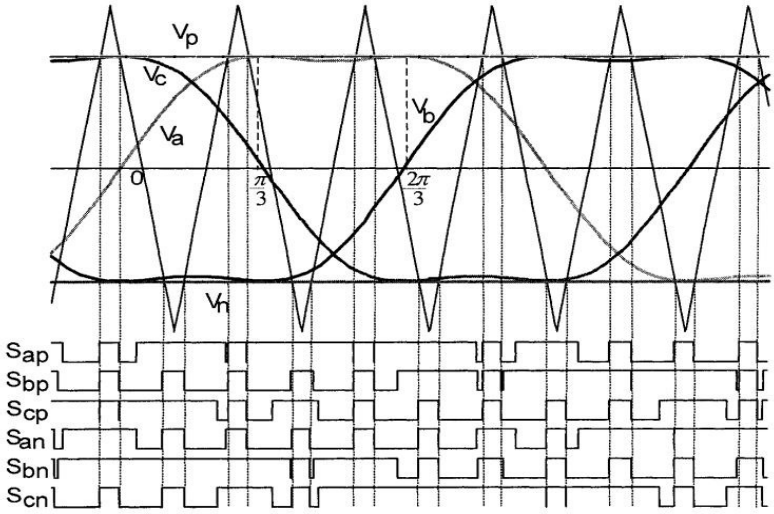

Figure 4.6: Maximum constant boost control with third harmonic injection strategy

The harmonic injection with 1/6 of third harmonic gives us a unique advantage of utilizing just two straight lines, 'V_p' and 'V_n' to control the shoot through duty ratio. By states we can obtain a voltage gain ranging from zero to infinity. The duty ratio for the shoot-through period remains constant and is expressed as,

$$B = \frac{T_{sh}}{T} = 1 - \frac{\sqrt{3}m}{2} \tag{4.14}$$

where 'T_{sh}' is the time interval for shoot-through, 'T' is remainder of the switching time and 'm' is the modulation index.

The boost factor B and the voltage gain are written as,

$$B = \frac{1}{1 - 2\frac{T_{sh}}{T}} = \frac{1}{\sqrt{3}m - 1} \tag{4.15}$$

$$\frac{\frac{V_{ac}}{V_m}}{2} = m.B = \frac{m}{\sqrt{3}m - 1} \tag{4.16}$$

where 'V_{ac}' is the output AC voltage and 'V_{in}' is the input voltage.

This method achieves maximum boost while keeping shoot through duty ratio constant all the time, thus reducing ripple content in inductor current compared to maximum boost control method.

4.4 Modified Space Vector Pulse Width Modulation Control

The space vector pulse width modulation technique cannot be directly applied to the Z-source inverter with the inclusion of the shoot-through states and needs to be altered without causing loss in the active space vectors [73]. This section discusses the modified space vector modulation control for Z-source networks.

The space vector pulse width modulation method for a voltage source inverter,

Modulation index $(m) = \frac{U_{ref}}{\frac{2}{3}U_d}$;

Time for active voltage vector, $T_1 = \frac{T_s\, m \sin\frac{\pi}{3} - \gamma}{\sin\frac{\pi}{3}}$ and $T_2 = \frac{T_8\, m \sin\gamma}{\sin\frac{\pi}{3}}$

Time for zero vectors is, $T_7 = T_8 = \frac{T_{sh}}{2}$

The combination of a modified space vector pulse width modulation with the shoot-through state for a Z-source inverter can be used to achieve AC voltages higher than $\left(\frac{2}{\pi}\right)V_{dp}$, which is the maximum value achieved by a traditional voltage source inverter with space vector pulse width modulation technique as shown in the Figure 4.7. The Figure 4.8 shows the voltage vector realized using the modified space vector pulse width modulation technique.

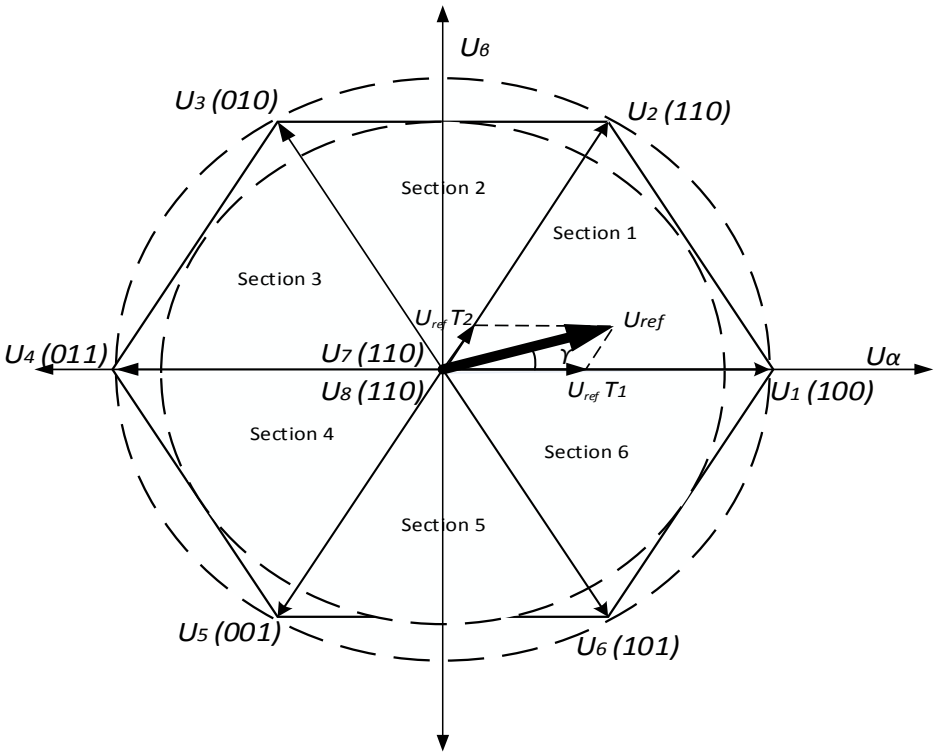

Figure 4.7: Space vector pulse width modulation of voltage source inverter

The realization of Z-source inverter to utilize the shoot-through, the space vector pulse width modulation technique should be modified as shown in Figure 4.8. Figure 4.9 show both the conventional and modified switching patterns for the Z-source converter at each sector. In Figure 4.9, a new time (T) should be added to the switching time (T_1, T_2, and T_0) of the conventional space vector pulse width modulation in order to boost the DC-link voltage of the Z-source inverter and to produce the sinusoid AC output voltage. In the Table 4.1, the modified space vector pulse width modulation switching time of the upper and lower switches in a Z-source inverter is summarized.

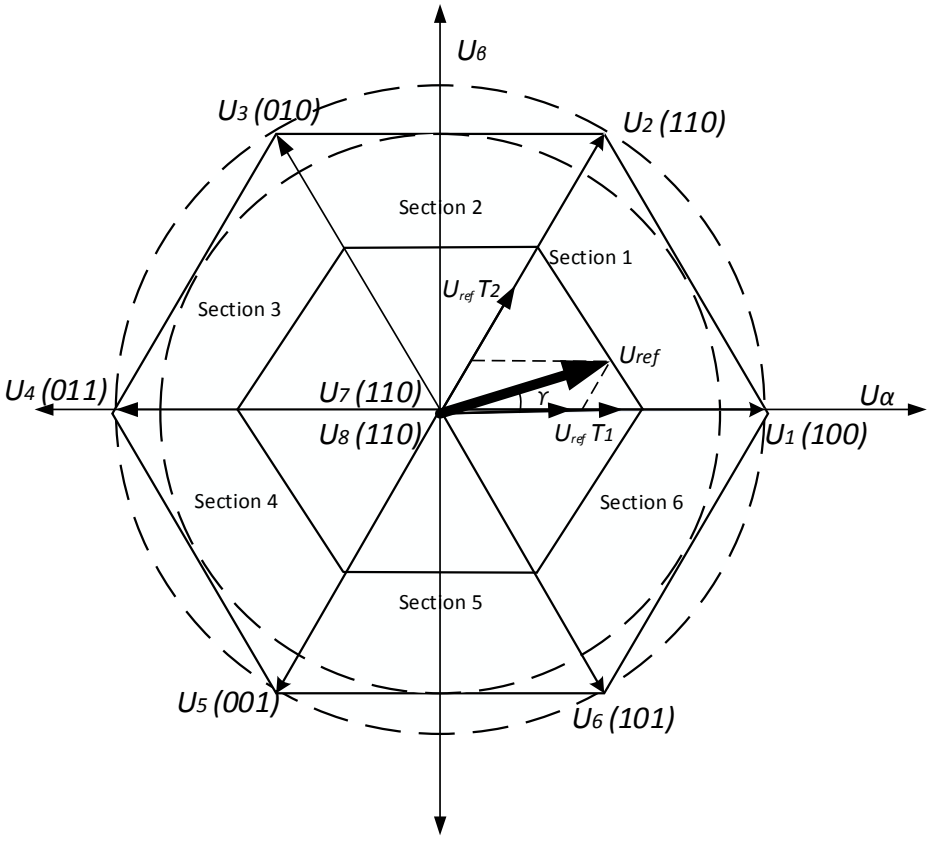

Figure 4.8: Modified space vector pulse width modulation of Z source inverter

In the Z-source inverter, the peak value of phase voltage can be

$$\hat{V}_{ac} = m\frac{V_{dp}}{2} = m.B\frac{V_{in}}{2} \tag{4.17}$$

Where $B = \dfrac{T_z}{T_{nsh} - T_{sh}} = \dfrac{1}{1 - 2\dfrac{T_{sh}}{T_s}}$

'B' is called a boost factor, 'm' is modulation index, 'V_{dp}' is the peak DC-link voltage. $T_z = T_{sh} + T_{nsh}$; 'T_z' is the switching period, 'T_{sh}' is the total duration of shoot-through zero vectors during 'T_z' and 'T_{nsh}' is the total duration of nonshoot-through switching vectors during 'T_z'.

From equation (4.17), the peak value of inverter output voltage (V_{ac}) definitely depends on both the modulation index (m) and the boost factor (B). Moreover, sum of the modulation index ($m = T_{nsh}/T_z$) and the ratio $T_{nsh} = T_z$ is always equal to unity. The boosted rate of the DC-link voltage is dependent on the total duration ($T_{sh} = 3T$) of

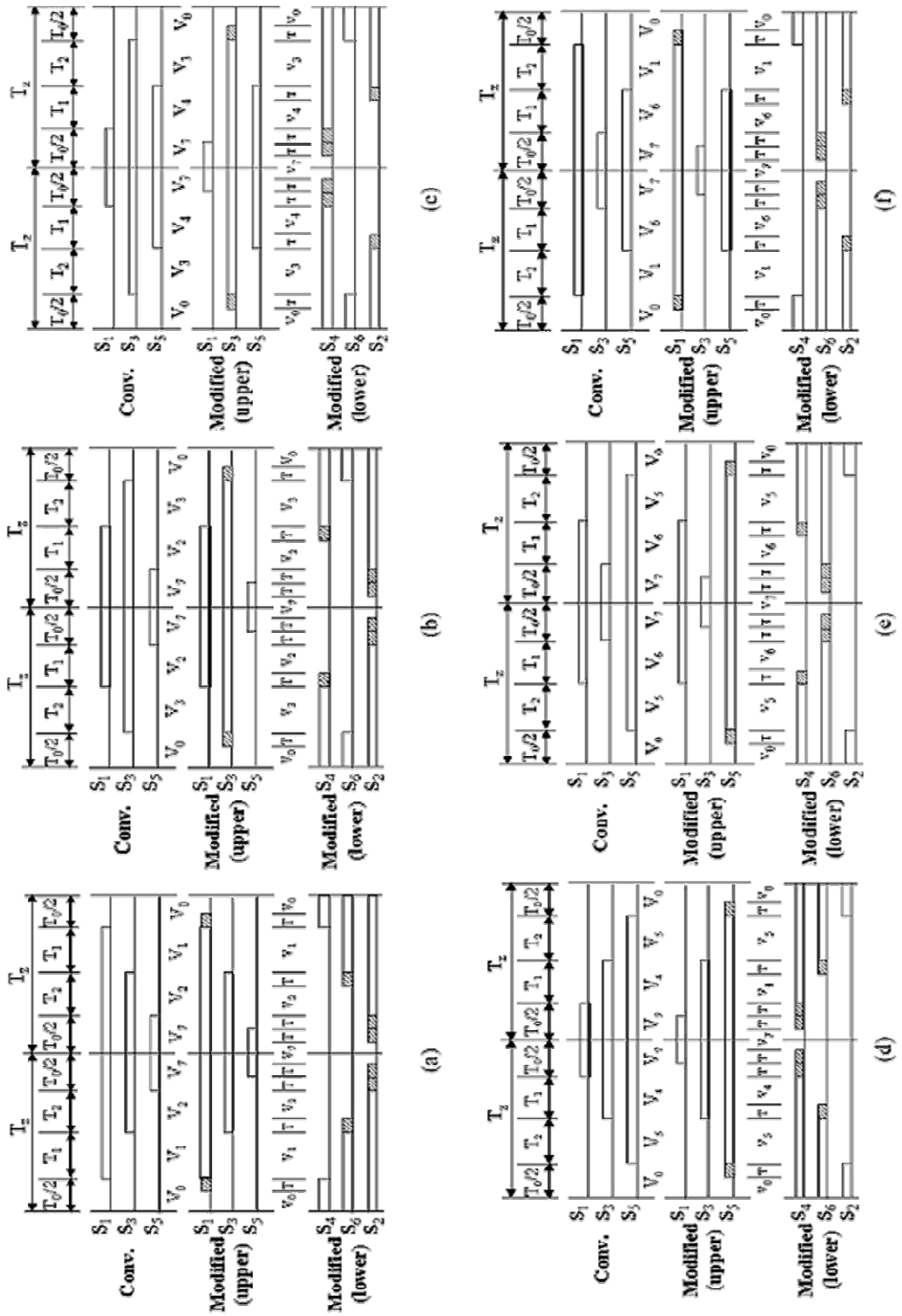

Figure 4.9: Modified space vector pulse width modulation implementation

(a) Sector 1, (b) Sector 2, (c) Sector 3, (d) Sector 4, (e) Sector 5 and (f) Sector 6

shoot-through zero vectors that simultaneously turn on both power switches in a leg. In Figure 4.9, each phase still switches on and off once per switching cycle (T_z), and has only one shoot-through zero state (T) over one period (T_z) in any sector without the change of total zero vectors (V_0, V_7, and T) and total nonzero switching vectors (V_1-V_6). Even if the output voltage of inverter and DC-link voltage can be controlled by adjusting 'T_{sh}', the maximum available shoot-through interval (T_{sh}) to boost the DC-link voltage (V_{dp}) is limited by the zero vector duration ($T_0 = 2$).

Table 4.1: Switching time duration at each sector

Sector	Upper (S_1, S_3, S_5)	Lower (S_4, S_6, S_2)
1	$S_1 = T_1 + T_2 + (T_0/2) + T$	$S_4 = (T_0/2)$
	$S_3 = T_2 + (T_0/2)$	$S_6 = T_1 + (T_0/2) + T$
	$S_5 = (T_0/2) - T$	$S_2 = T_1 + T_2 + (T_0/2) + 2T$
2	$S_1 = T_1 + (T_0/2)$	$S_4 = T_1 + (T_0/2) + T$
	$S_3 = T_1 + T_2 + (T_0/2) + T$	$S_6 = (T_0/2)$
	$S_5 = T_0/2 - T$	$S_2 = T_1 + T_2 + (T_0/2) + 2T$
3	$S_1 = (T_0/2) - T$	$S_4 = T_1 + T_2 + (T_0/2) + 2T$
	$S_3 = T_1 + T_2 + (T_0/2) + T$	$S_6 = (T_0/2)$
	$S_5 = T_2 + (T_0/2)$	$S_2 = T_1 + (T_0/2) + T$
4	$S_1 = (T_0/2) - T$	$S_4 = T_1 + T_2 + (T_0/2) + 2T$
	$S_3 = T_1 + (T_0/2)$	$S_6 = T_2 + (T_0/2) + T$
	$S_5 = T_1 + T_2 + (T_0/2) + T$	$S_2 = (T_0/2)$
5	$S_1 = T_2 + (T_0/2)$	$S_4 = T_1 + (T_0/2) + T$
	$S_3 = (T_0/2) - T$	$S_6 = T_1 + T_2 + (T_0/2) + 2T$
	$S_5 = T_1 + T_2 + (T_0/2) + T$	$S_2 = (T_0/2)$
6	$S_1 = T_1 + T_2 + (T_0/2) + T$	$S_4 = (T_0/2)$
	$S_3 = (T_0/2) - T$	$S_6 = T_1 + T_2 + (T_0/2) + 2T$
	$S_5 = T_1 + (T_0/2)$	$S_2 = T_1 + (T_0/2) + T$

The modified space vector pulse width modulation, the shoot-through current for each phase is twice the inductor current, which increase the current stress on the switch. Also, in high power range the PWM strategy with six shoot-through state insertions in one switching cycle brings more losses than its counterpart of two shoot-through state insertions in one switching cycle and higher switching frequency makes the efficiency gap become larger. On the other hand, in low output power range, the PWM strategy with six shoot-through state insertions is superior

Table 4.2: MSVPWM Control algorithm observations

Input voltage (V_{in})	Modulation index (m)	Duty ratio ($D_{sh\_max} = 1\text{-}m$)	Shoot through time (Tsh μs)	Boost factor (B)	Peak DC-link voltage (V_{dp})	Capacitor voltage [$V_C = (V_{dp} + V_{in})/2$]	
						Theoretical	Experimental
50 *V*	0.9	0.1	10	1..25	62.5 *V*	56.25 *V*	57
	0.8	0.2	20	1.66	83 *V*	66.5 *V*	65
	0.7	0.3	30	2.5	125 *V*	87.5 *V*	86

The real time implementation and validation of proposed modified space vector pulse width modulation technique for Z-source inverter is tabulated in Table 4.2 and capacitor voltage is shown in Figure 4.10.

Sample calculation:

Let be the, input voltage, V_{in} = 50 *V*, modulation index, m = 0.9 and switching frequency, f_s =10 kHz.

switching time T_s = 100 μs

The maximum shoot-through duty ratio D_{sh_max}

$$D_{sh\_\max} = 1 - m = 1 - 0.9 = 0.1$$

Shoot through time $T_{sh} = D_{sh} \times T = 0.10 \times 100 = 10$ μs

Boosting factor, $$B = \frac{1}{1 - 2\frac{T_{sh}}{T_s}} = \frac{1}{1 - 0.2} = 1.25$$

The peak DC-link voltage is $V_{dp} = B \times V_{in} = 1.25 \times 5\ 0 = 62.5\ V$

The capacitor voltage is $V_c = (V_{dp} + V_{in})/2 = (62.5 + 50)/2 = 56.25\ V$

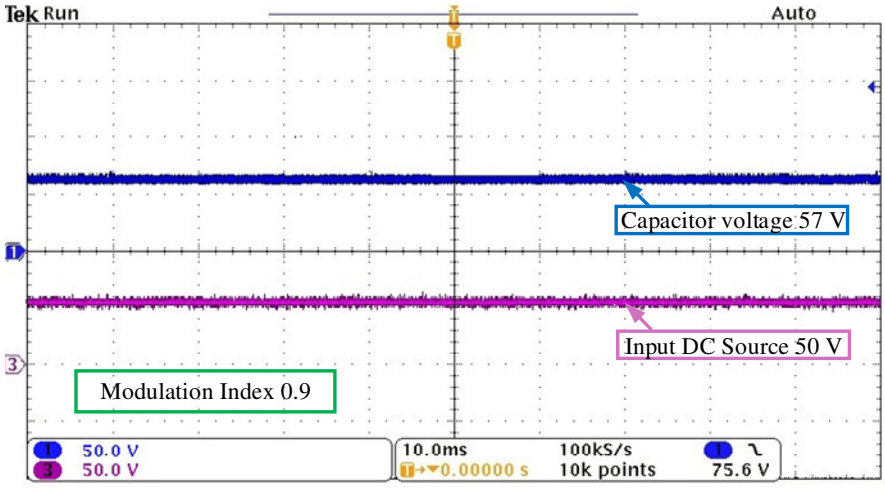

(a)

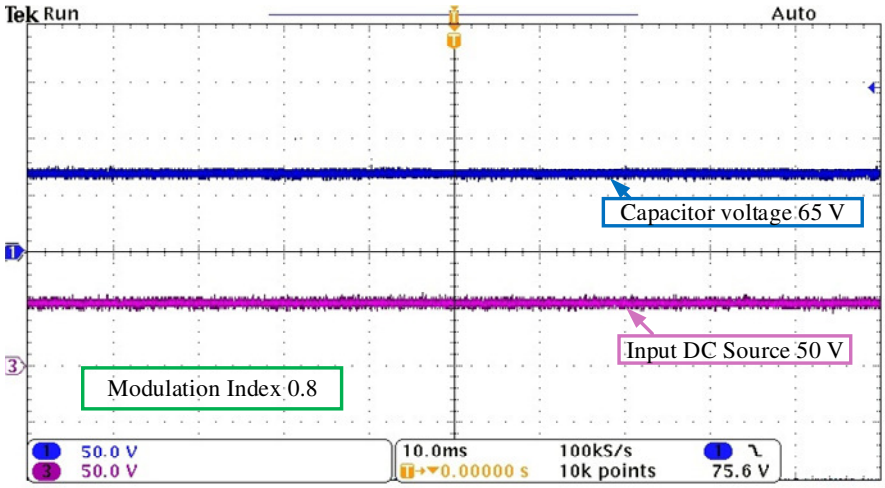

(b)

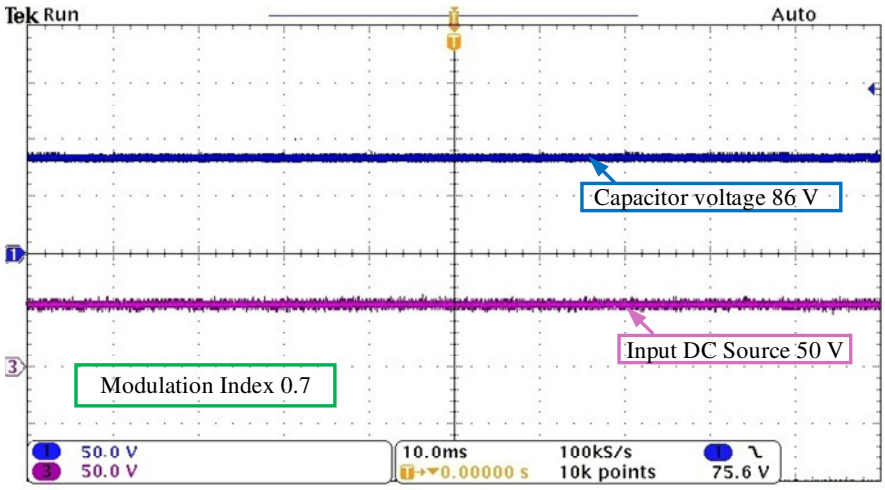

(c)

Figure 4.10: Capacitor voltage variation for different modulation index '*m*'

4.5 Double Space Vector Pulse Width Modulation (DSVPWM)

In the other modified pulse width modulation control methods modulation index has to be minimum to get maximum boost factor. But the voltage stress increases with minimum modulation index. This limitation is eliminated in the newly proposed double space vector pulse width modulation (DSVPWM) method.

This control method has the following features over the other traditional control methods

- Number of shoot through states per cycle of carrier wave is increased when compared to other methods.
- Switching loss is reduced as only one of the phase legs is gated during shoot through states.
- It involves alternative active state and shoot through state and no zero states. Hence, it reduces the ripple content in inductor current.
- The voltage stress across the switches is reduced as modulation index could be kept high.

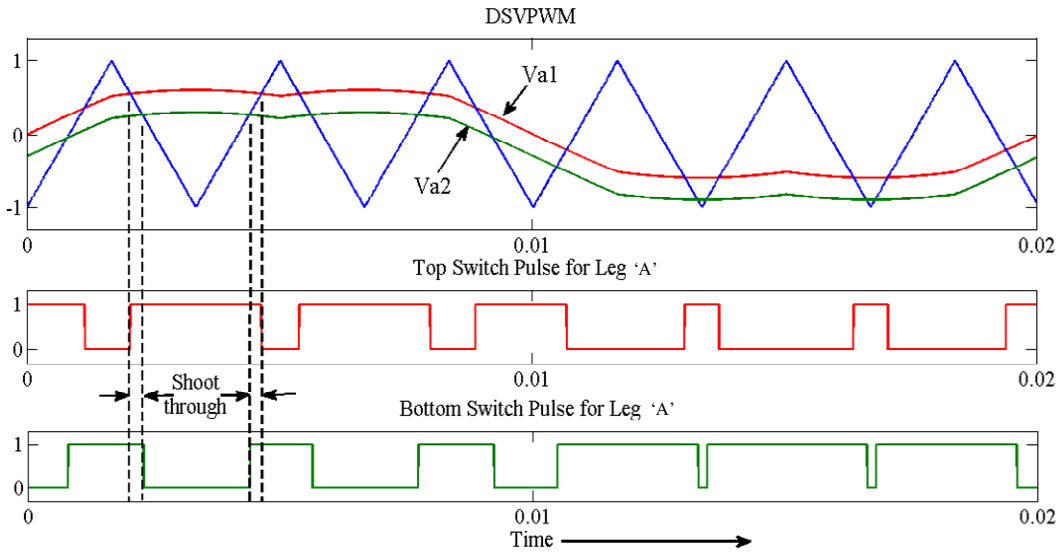

Figure 4.11: Double space vector pulse width modulation pulses for phase 'A'

The double space vector pulse width modulation (DSVPWM) technique uses two sets of three phase signals as reference signals and a high frequency triangular wave as carrier signal [74][75]. Let 'V_{a1}', 'V_{b1}', 'V_{c1}' be the first set of reference signals generated by space vector pulse width modulation technique for required modulation

'*m*' of input voltage. Let 'V_{a2}', 'V_{b2}', 'V_{c2}' be the second set of reference signals generated by adding a finite negative DC offset (V_{offset}) to the first set. The reference signals 'V_{a1}' and 'V_{a2}' will generate pulses are top and bottom switch of phase '*A*' respectively as shown in Figure 4.11. The offset results in a shoot through time 'T_{sha}' per switching period in that leg. For high switching frequencies, the reference signals 'V_{a1}' and 'V_{a2}' can be approximated as constants during a switching cycle. The relation between the shoot through time 'T_{sha}' and 'V_{offset}' can be established as follows: In Figure 4.12, consider similar triangles '*xyz*' and '*XYZ*'.

$$xy = \left(\frac{yz}{YZ}\right) \times XY$$

$$\frac{T_{sha}}{2} = \left(\frac{V_{offset}}{1-(-1)}\right) \times \left(\frac{T}{2}\right) \tag{4.18}$$

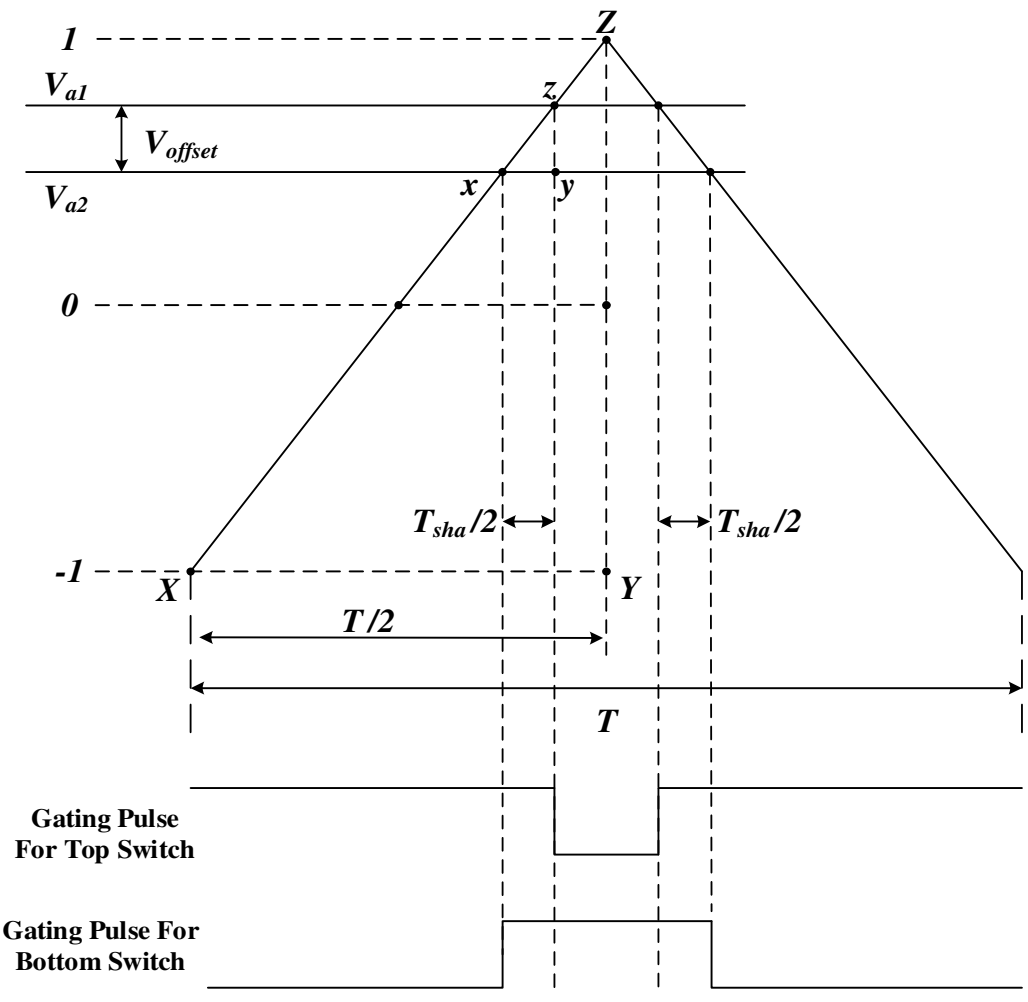

Figure 4.12: DSVPWM Shoot-through in phase 'A' of inverter

Shoot through time of phase '*A*',

$$T_{sha} = (V_{offset}) \times \left(\frac{T}{2} \right) \tag{4.19}$$

The shoot through time in all three legs of the inverter remains same whereas the instants at which they occur during a switching period vary. So, the shoot through time in phases '*B*' and '*C*' is,

$$T_{shb} = T_{shc} = T_{sha} = (V_{offset}) \times (T/2)$$

The total shoot through time T_{sh} per switching period can be written as,

$$T_{sh} = 3 \times T_{sha} = 3 \times (V_{offset}) \times (T/2) \tag{4.20}$$

The shoot through duty ratio D_{sh} can be defined as,

$$D_{Sh} = \frac{\text{Shoot through time}(T_{sh})}{\text{Total switchingtime}(T)} \tag{4.21}$$

$$D_{Sh} = 3 \times \frac{V_{Offset}}{2} \tag{4.22}$$

$$V_{Offset} = 2 \times \frac{D_{sh}}{3} \tag{4.23}$$

The double space vector pulse width modulation technique introduces 'V_{offset}' to extend the pulse width of the bottom switch into the top switch pulse width to result in shoot-through time. When the Z-source inverter is operated at a space vector pulse width modulation's modulation index of '*m*', the minimum pulse-width of the top switch is (1 - *m*) *T*/2 and it occurs in a switching period during the negative half cycle of the fundamental wave. The bottom switch pulse width during this switching period is (1 + *m*) *T*/2 when 'V_{offset}' is zero. As 'V_{offset}' increases, the bottom switch pulse width increases from (1 + m) *T*/2 to a maximum of `T' at a maximum offset voltage 'V_{offset_max}'. On further increase in 'V_{offset}', space vector pulse width modulation operation enters into over-modulation region. So, the maximum limit 'V_{offset_max}' can be obtained as follows:

At maximum offset voltage 'V_{offset_max}' condition, if 'T_{sha_max}' is the maximum shoot through time of phase 'A',

$$T_{sha\_\max} = T - (1+m) \times \frac{T}{2}$$

$$T_{sha\_\max} = (1-m) \times \frac{T}{2} \tag{4.24}$$

From (4.19)

$$T_{sha\_\max} = (V_{offset\_\max}) \times \frac{T}{2} \tag{4.25}$$

Substituting (4.24)

$$(V_{offset\_\max}) \times \frac{T}{2} = (1-m) \times \frac{T}{2} \tag{4.26}$$

$$V_{offset\_\max} = 1-m \tag{4.27}$$

From equation (4.22) and (4.27), the maximum shoot-through duty ratio $D_{sh\_\max}$ is,

$$D_{sh\_\max} = 3 \times \frac{(1-m)}{2} \tag{4.28}$$

Table 4.3: DSVPWM Control algorithm observations

Input voltage (V_{in})	Modulation index (m)	V_{DC_offset}	Shoot through time (T_{sh} µs)	Boost factor (B)	Peak DC-link voltage (V_{dp})	Capacitor voltage (V_C)	
						Theoretical	Experimental
50 *V*	0.9	0.1	15	1.428	71.42 *V*	60.71 *V*	60 *V*
	0.8	0.2	30	2.5	175 *V*	87.5 *V*	88 *V*
	0.7	0.3	45	10	500 *V*	275 *V*	274 *V*

The real time implementation and validation of double space vector pulse width modulation technique for different modulation index is tabulated in Table 4.3. The Z-network input and capacitor voltages are shown in Figure 4.13. The double space vector pulse width modulation technique is boost the DC-link voltage more than the modified pace vector pulse width modulation technique for same modulation index in Z-source inverter.

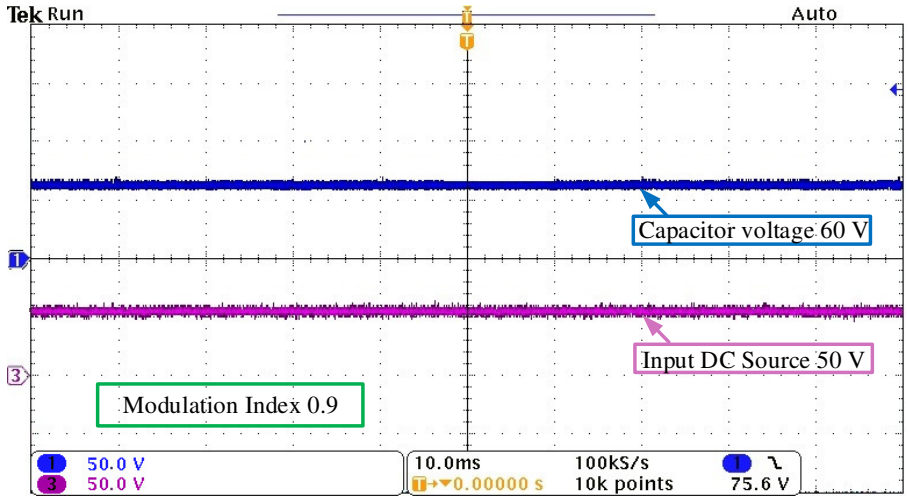

(a)

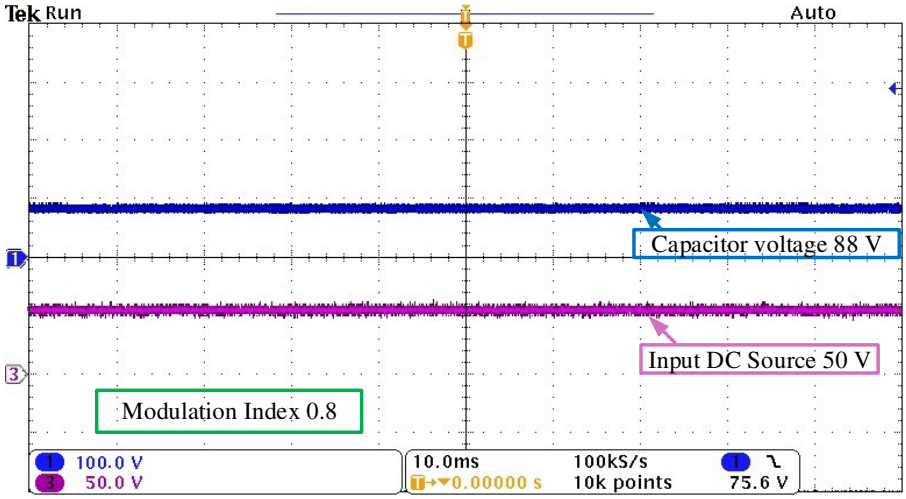

(b)

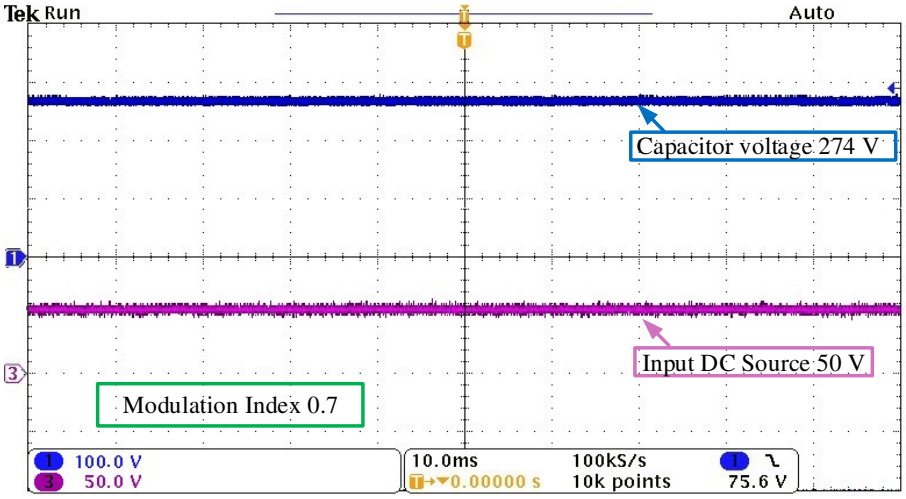

(c)

Figure 4.13: Capacitor voltage variation for different modulation index '*m*'

Sample calculation:

Let be the, in put voltage V_{in} = 50 *V*, modulation index (*m*) = 0.9 and Switching frequency f_s = 10 kHz , Switching time T_s = 100 μs.

From equation (4.28), the maximum shoot-through duty ratio $D_{sh\_\max}$

$$D_{sh\_\max} = 3\frac{(1-0.9)}{2} = 0.15,$$

Shoot through time, $T_{sh} = D_{sh} \times T = 0.15 \times 100 = 15$ μs

Boosting factor, $B = \frac{1}{1-2\frac{T_{sh}}{T_s}} = \frac{1}{1-0.3} = 1.428$

The peak DC-link voltage is $V_{dp} = B \times V_{in} = 1.428 \times 50 = 71.42$ *V*

The capacitor voltage is $V_c = (V_{dp} + V_{in})/2 = (71.42 + 50)/2 = 60.71$ *V*

The double space vector pulse width modulation technique gave more boosting in the voltage than the modified space vector pulse width modulation method for same modulation index shown in Figure 4.13 and Tables 4.2. However, the inverter output voltage was found to be lesser than that of modified space vector pulse width modulation (DSVPWM utilizes a part of active state for boosting the DC-link voltage). This drawback restricted the double space vector pulse width modulation in the application of speed control of induction motor.

4.6 Summary

Various control methods, simple control, maximum boost control, maximum constant boost control and double space vector pulse width modulation have been presented in this chapter. Maximum boost control achieves lowest voltage stress across the devices. However this method will also result in line frequency current through Z-source inductor thus increases the requirement for the inductor. The maximum constant boost control minimizes the voltage stress across the device on the basis that there is no line frequency current ripple through the Z-source inductor. Moreover, a modified space vector pulse width modulation for voltage-fed Z-source inverter suitable for variable frequency AC drives has been discussed. With the modified space vector pulse width modulation, the AC voltage obtainable from Z-source inverter is no longer limited and can be boosted beyond the limit constrained by conventional voltage source inverter.

Chapter - 5

Peak DC-Link Voltage Control Strategies

This chapter mainly focuses on the peak DC-link voltage control through the linear/ non-linear (hybrid) controller, to get high performance of the drive under all operating conditions. Normally an induction motor drive employs a DC-DC boost converter for boosting the low voltage from battery and then followed by a voltage source inverter. The additional boost converter unit adds the cost and lowers the efficiency and reliability of the drive system. The variations in DC-link voltage adversely affect the drive operating performance, many time lead to break down in drive system. Also the VSI fed drives with current regulation (load change), the current regulator saturates if the DC-link voltage drops below the 20% - 50% of nominal value. The induction motor drive, under a standard V/f speed control, if input DC-link voltage drops then inverter may not be able to deliver the required voltage to the motor at a certain speed [76]. The Z-source inverter fed induction motor drive is shown in Figure 5.1. The DC-link voltage is pulsating with high frequency (approx. = 3*fs*) in nature between zero and peak DC-link voltage as shown in Figure 5.1(a). Therefore, DC-link voltage needs to be regulated and its precise control of peak DC-link voltage of the inverter is very essential for reliable drive operation. Normally, a proportional integral (PI) controller is used for peak DC-link voltage control.

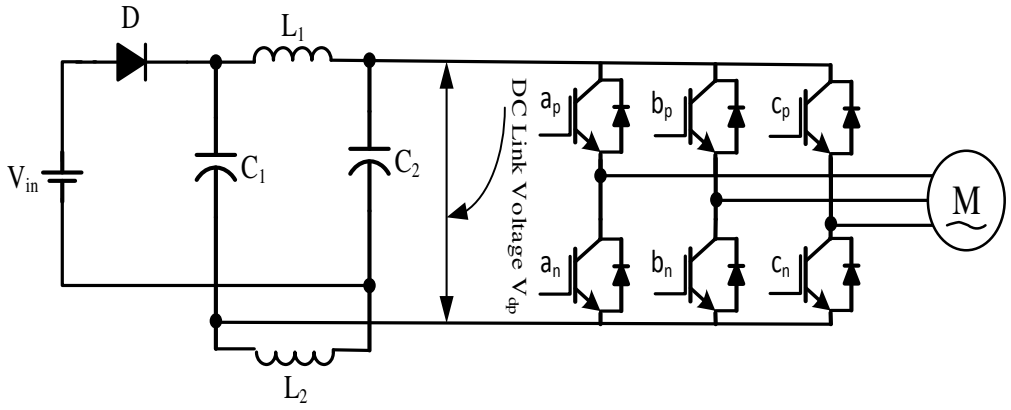

Figure 5.1(a): Z-source inverter fed induction motor

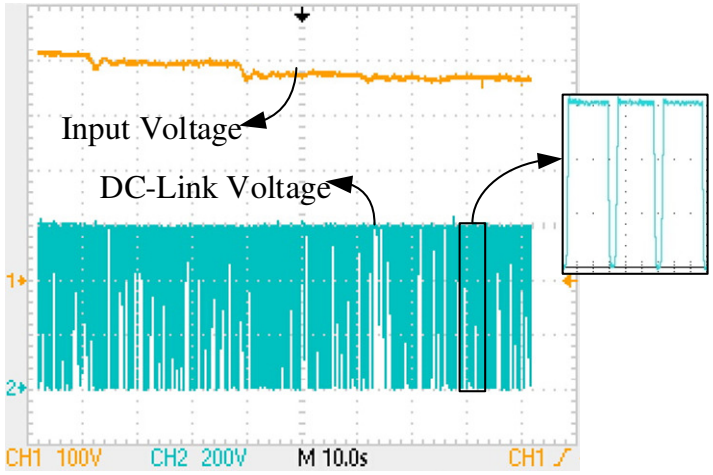

Figure 5.1(b): DC-link voltage and input voltage

The DC-link voltage is pulsating. It's direct peak measuring and control is difficult. Hence, the peak DC-link voltage is controlled through the capacitor voltage control. The capacitor voltage control block diagram is shown in Figure 5.2. G_{vin} is the input to capacitor voltage transfer function and G_{vd} is the control to capacitor voltage transfer function. The reference value of capacitor voltage (V_{cRef}) can be calculated based on the peak DC-link voltage and the input voltage. By properly controlling the capacitor voltage value [$V_{c\text{Ref}} = (V_{in} + V_{dp\text{Ref}})/2$] through the PI controller $G_c(s)$ then the peak DC-link voltage can be controlled precisely, so the performance of the input voltage interruption elimination can be improved [77][78]. The detailed performance analysis is shown in Chapter 7.

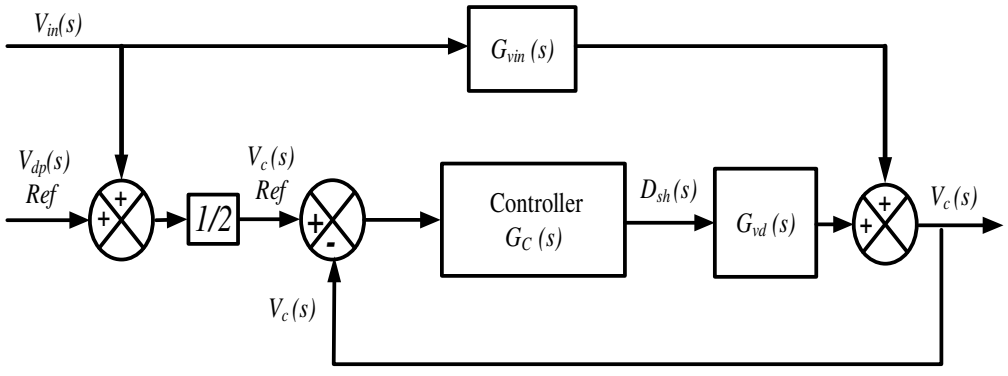

Figure 5.2: Block diagram for capacitor voltage control

5.1 Control Devices

Feedback control systems have been integral part of all engineering application as shown in Figure 5.3. This reinforces the importance of control in engineering. The electrical vehicle technology demands for highly precise systems for voltage control, speed and torque.

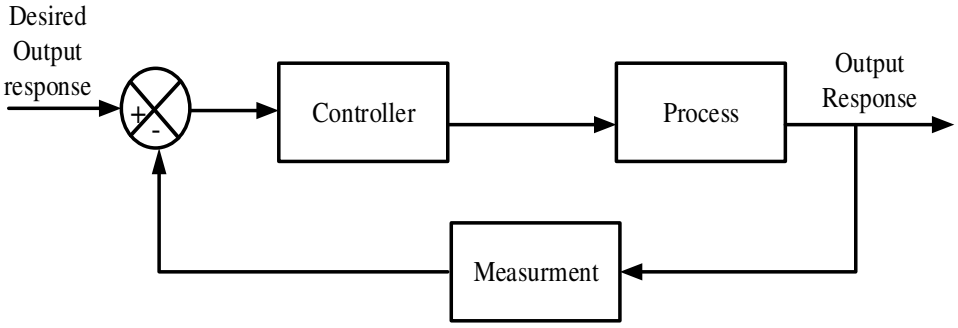

Figure 5.3: PID controller with plant

5.1.1 PID Controller

Each of the letters in PID controller stand for three basic modes, proportional, integral and derivative mode. PID controllers have evolved through the ages to adapt to changes in mechanics and pneumatics to microprocessor chip through electronic transistors and integrated circuits. The implementation of the voltage and speed control algorithm requires the selection of these modes and specification of the parameters or settings for each mode. The microprocessors have had lasting impact on the controllers and have presented avenues of developing additional characteristics like the auto tuning, gain scheduling and continuous adaptation [79][80][81].

5.1.1.1 Tuning of Controller's Parameters

The process of tuning a feedback control loop translates to the arrangement of the loop parameters to optimal values to realize the required control response [82]. Here, stability might seem like the only major factor to be taken care of, but inevitably different systems tend to pose different behaviors under different conditions. Theoretically, the process of tuning would be regarded as straight forward with having to modulate only three parameters to arrive at the desired results, but in practicality it is not an easy task as the complex criteria at the PID limit should be satisfied. The science of tuning a PID

control is primarily heuristic in nature but the numerous objectives that have to be achieved compel the need to tackle problems like short transient, non-linearity and the possibility of heavy divergence in output due to unstable input which may lead to saturation and mechanical breakdown.

The stability of the output of a system is essential for its efficient operation and should not have any oscillations in any set point conditions or perturbations. Characteristics like rise time, overshoot, settling time are the important factors which influence the process of tuning the modes of control in the system. The realization of optimum conditions of the system depends on the arrangement of the gain factors 'k_p', 'k_i' and 'k_d' or the values of 'k_c', 't_i' and 't_d' according to the system characteristics.

There are many more prevalent tuning methods most of them are basic methods. In this section we will discuss only the Ziegler-Nichols tuning method, as it is widespread and most commonly accepted tuning method in electronics applications.

5.1.1.1.1 Zeigler-Nichols Tuning Method

A classical PI controller is widely used in the automation and real time industry. It has a high capability and a simple structure. It has high capability of solving practical control problems. The PI controller involves two separate parameters: integral (*I*) and the proportional (*P*) values. These values could be interpreted using time: '*P*' is dependent on the present error and '*I*' on the accumulation of past errors.

The PI controller can be expressed as follows:

$$G(s) = K_p + \frac{K_i}{S} \tag{5.1}$$

where 'K_p' is the proportional gain and 'K_i' is the integral gain.

The discrete-time equivalent expression for PI controller is used in this thesis as:

$$u(k) = K_p e(k) + K_i T_s \sum_{i=1}^{k} e(i) \tag{5.2}$$

Here, '$u(k)$' is the control signal, '$e(k)$ ' is the error between the reference and the output of the process, '*Ts*' is the period of sampling used in the controller. '*Kp*' and '*Ki*', are the parameters of the PI controller which, can be manipulated in various ways and the results can be converted into various response curves for a given process by finding optimal adjustments of a controller.

The determination of parameters of the controller to meet the steady-state and transient specifications of the closed loop system requires a mathematical model of the plant. In cases where the mathematical model of the system cannot be obtained, we cannot apply the analytical and computational approaches to design the PID controller. In such scenarios we rely on experimental approaches to establish the control parameters [83][84][85].

Zeigler and Nichols tuning method describing some suggestive rules to tune the PID controller based on the results of experimental step responses or the value of 'K_p' that achieves marginal stability, when only the proportional control is in action. The Zeigler-Nichols rules which are briefly discussed here are extremely useful in situations where the mathematical models of the system are unknown. These rules assign few specific initial values to 'K_p', 'T_d' and 'T_i' which will lead to stability in the operation of the system. However, the plant may still exhibit large maximum overshoot in the step response, which is not acceptable. In such cases further tuning of the values needs to be done to achieve the overall performance specification of the system. Thus the Zeigler-Nichols tuning rules are some well directed starting point for setting up the parameter values for the tuning process, rather than an accurate setting of the values at once. The rules proposed by Zeigler and Nichols for obtaining the proportional gain 'K_p', integral time 'T_i' and derivative time 'T_d' are taken from the transient response characteristics of a given system. There are 2 types of Zeigler-Nichols tuning methods.

5.1.1.1.2 Type 1

This method is determined through the unit step response of the system. The absence of both integrators and dominant complex conjugate poles results in the unit-step response curve being an S-shaped one. This method is suitable to the systems which present an S-shaped response as shown in Figure 5.4. Such step-responses can be obtained experimentally or dynamically simulating the plant. The S-shaped unit-step response curve can be characterized by two constants, time constant 'T' and delay time 'L'. These two constants 'T' and 'L' are calculated by drawing a tangent line at the point of inflection of the S-shaped unit-step response curve and intercepting the points of intersection of the tangent at the inflection point with the line $c(t) = K_e$ then approximated by a first order system which has transport lag as follows:

The values of 'K_p', 'T_i' and 'T_d' suggested by Zeigler-Nichols are given in the Table 5.1.

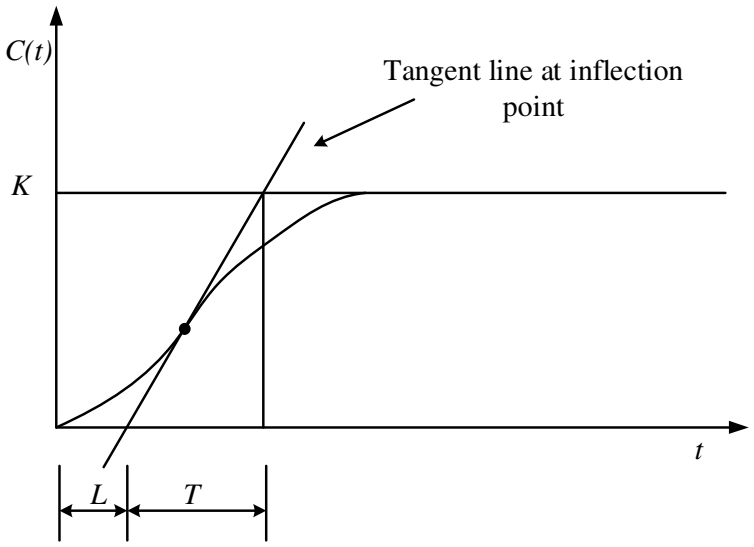

Figure 5.4: S-shaped response curve

Table 5.1: The Zeigler-Nichols PID controller tuning type 1 parameters

Type of controller	K_p	T_i	T_d
P	$\frac{T}{L}$	∞	0
PI	$0.9\frac{T}{L}$	$\frac{L}{0.3}$	0
PID	$1.2\frac{T}{L}$	$2L$	$0.5L$

5.1.1.1.3 Type 2

In this method, first begin with adjusting the values of 'T_i' to infinity and 'T_d' to '0'. After that increase 'K_p' from '0' to a critical value 'K_{cr}' at which the output first exhibits sustained oscillations using only the proportional control action. This method is not applied to systems which do not exhibit sustained oscillations for any value of 'K_p'. Hence, the critical gain value 'K_{cr}' and period 'P_{cr}' corresponding to it are experimentally obtained. Zeigler and Nichols suggested the values for these parameters 'K_p', 'T_i' and 'T_d' which are given in Table 5.2. Zeigler-Nichols tuning rules have been used extensively to design PID controllers which in-turn used in process control systems in which the plant dynamics are not precisely known. Zeigler-Nichols tuning rules are also applicable to plants whose dynamics are unknown.

Table 5.2: The Zeigler-Nichols PID controller tuning type 2 parameters

Type of controller	K_p	T_i	T_d
P	$0{:}5Kcr$	∞	0
PI	$0.45Kcr$	$\frac{1}{1.2}P_{cr}$	0
PID	$0.6Kcr$	$0{:}5Pcr$	$0{:}125Pcr$

The fixed controller parameters will have to be chosen through a (Ziegler-Nichols) optimal method. However, because of the high non-linearity of the system, the PI controller with fixed parameters will not be able to provide satisfactory control and peak DC-link voltage control performance. Hence, the usage of linear PI control technique for controlling a nonlinear system results in a tuning configuration that must be adjusted when a change occurs in the dynamic operating conditions. The resulting fuzzy gain scheduling (FGS) to adjust the controller parameters of PI controller's technique has to be solved based on non linear control problems. The fuzzy gain scheduling PI controller is combination of fuzzy logic and classical PI controller. Where PI controller tuned from type 2 tuning method of Zeigler-Nichols tuning method, because the peak DC-link voltage of Z-source inverter control is complex.

5.2 Fuzzy Logic

Fuzzy logic techniques have been extensively applied in all fields of today's society. Fuzzy logic is analogous to the human abilities of reason and inference [86]. It is different from the classical logic in that it depends more on range-to-point or range-to-range interpretation than point-to-point interpretation. The output from a fuzzy based control strategy is determined from the fuzzification of input signals and output signals with the help of associated membership functions. A crisp input will be juggled through a set of interface member functions to interpret its value and then arrive at an output, which consolidates the interpretations of all the membership functions.

Fuzzy Logic is implemented to real time application in three basic steps:

1. Fuzzification: This process converts crisp input data into fuzzy data or membership functions (MFs). Data is converted to linguistic variables which are similar to human configuration of data unlike machines which read data purely as either true or false.
2. Fuzzy Inference Process: This process concatenates the MF's (membership functions) with the control rules to obtain the fuzzy output. The most important rule for the fuzzy inference process is the control rule and these rules are directly related to feeling of a human beings and their intuition.
3. De-fuzzification: This process uses many different methods to obtain each associated output and arrange them into a table called the lookup table. Then the output is picked up from the lookup table corresponding to the current input during an application. This output is then translated to the required crisp output from linguistic variables.

A fuzzy process is a process of crisp-fuzzy-crisp for a real system. The given input and the output must be crisp variables and the intermediate process is a fuzzy inference process [87]. There is a reason for why anyone has to change a crisp to a fuzzy variable is that, from the view of fuzzy control or a human beings intuition, no absolute crisp variable exists in the real world. Any physical parameter may have some other components. For instance, if someone says: the temperature is high here. This high temperature contains some middle and even low temperature components. From this point of view, fuzzy control uses universal or global components, not just a limited range of components as the classical variables did.

5.2.1 Fuzzy Sets

Concepts of fuzzy sets are an extension of a classical or crisp set concept. The classical set only takes a limited number of value of membership such as 0 or 1, or certain range of data which is of limited value of membership whereas fuzzy sets allow for more diversity in its fold. Thus, the fuzzy set is basically a broader set compared to the classical or crisp set [88][89].

5.2.2 Fuzzification

The fuzzy set is a very useful tool allowing the representation of members or objects in a indefinite or abstract manner. The fuzzy set also gives a way which is similar to a human beings intuition and thought process. However, only the fuzzy set itself cannot assure any practical and useful industrial products until the fuzzy inference process is used.

Fuzzification is the basic step to apply a fuzzy inference system. Almost all variables in our world are crisp or classical variables. Fuzzification mainly contains two processes: derivation of the membership functions for input and output variables and their representation in linguistic variables. This process is analogous to converting or mapping classical sets to fuzzy sets in varying values. In practice, membership functions can have multiple forms, such as the triangular waveform, trapezoidal waveform, gaussian waveform, bell-shaped waveform, sigmoid wave-form and S-curve waveform. The exact type depends and subject to actual applications. For those systems that need significant dynamic variation in a short period of time, a triangular or trapezoidal waveform should be utilized whereas for systems that need very high control accuracy, a gaussian or S-curve waveform should be selected.

5.2.3 Fuzzy Control Rules

Fuzzy control rule is similar to the knowledge and concepts of an expert in any similar field of application. The fuzzy rule is represented by a sequence of the form IF-THEN, leading to algorithms describing what action should be taken in terms of the currently observed information, which includes both input and feedback in a closed-loop control system. The design of the fuzzy rules is dependent on a human beings knowledge or experience with the application. A fuzzy IF-THEN rule associates a condition described using linguistic variables as premise and fuzzy sets to an output or a conclusion [90][91]. The IF part is mostly used in the elastic conditions. The THEN part may be used to give the conclusion or output in linguistic variable form. This IF-THEN rule is extensively used by the fuzzy inference system for computing the value to which the input data matches the conditions of a rule.

Fuzzy mapping rules provide a plot of the inputs and the outputs using linguistic variables. The foundation of a fuzzy mapping rule is a fuzzy graph, which explains the relationship between the fuzzy output and the fuzzy input. Sometimes it is very hard to

get an exact relationship between the output and the input, or relationship between those inputs and outputs is too complex to work it out. Fuzzy mapping rules work in a similar way to human behavior or intuition, and each of those rule only approximates a limited number of elements of that particular function, so set of fuzzy mapping rules are used to approximate entire function.

5.2.4 Defuzzification

The control output or conclusion obtained from the concatenation of output, input membership functions and fuzzy rules is still indefinite fuzzy element which needs to be made crisp. To obtain that fuzzy output or conclusion available to industrial applications, a defuzzification process is most needed. The defuzzification process is meant to convert the fuzzy output back to the crisp or classical output to the control objective. The fuzzy output or conclusion is still a linguistic variable, and this variable needs to be converted to the crisp variable via the defuzzification process.

There are three techniques which are commonly used in the defuzzification process:

- Mean of Maximum (MOM) Method: The Mean of Maximum (MOM) defuzzification method calculates the mean of those fuzzy outputs or conclusions that have the highest degrees.
- Centre of Gravity Method (COG) Method: The Centre of Gravity method (COG) is the most popular defuzzification technique and is extensively used in actual industrial applications. This method is same as the formula for calculating the centre of gravity in physics. The weighted mean of the membership function or the centre of the gravity of the area bounded by the membership function curve is computed to be the crispest value of the fuzzy quantity.
- The Height Method: This defuzzification technique is only true for some cases in which the output membership function is an aggregated union result of symmetrical functions.

In fuzzy control, linguistic descriptions of human expertise in controlling a process are represented as fuzzy rules. This knowledge base is used by an inference mechanism, in conjunction with some knowledge of the states of the process in order to determine control actions. Although they do not have an apparent structure of PI controllers, fuzzy logic controllers may be considered nonlinear PI controllers whose

parameters can be determined on-line based on the error signal. In the following section, an on-line gain scheduling scheme of the PI controller based on fuzzy rules is introduced.

5.3 Fuzzy Gain Scheduling

An on-line gain scheduling scheme of a fuzzy rules and reasoning based PI controller is introduced [92][93]. The fuzzy logic based controller has many advantages as it is very suitable to handle problems which deal with uncertainty and unstructured systems. It also handles inaccurate data in a proper manner and allows proper functioning of operating systems [94][95]. In this research work, fuzzy logic is utilized to fine-tune the gains of the PI controller adaptively under dynamic conditions, so it is named a Fuzzy Gain Scheduling-PI (FGS-PI) controller as shown in Figure 5.5.

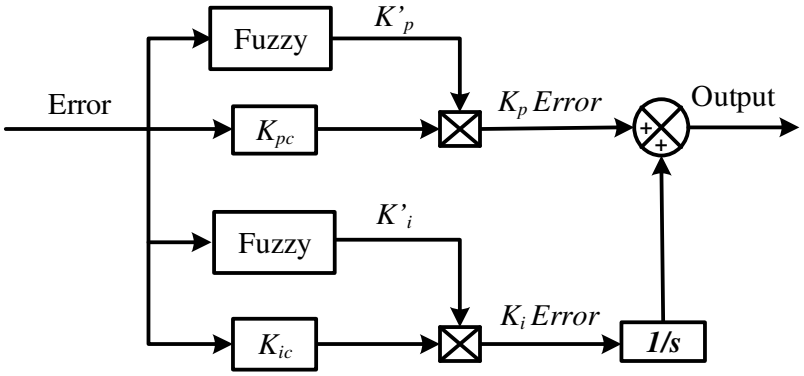

Figure 5.5: Functional block diagram for FGS-PI controller

In this proposed approach, we take advantage of fuzzy rules and reasoning to determine the controller parameters '$K_p^{'}$' and '$K_i^{'}$'. These controller parameters are multiplied with 'K_{pc}'(proportional gain) and 'K_{ic}'(integral gain) of the classical PI controller from the Ziegler-Nichols method. The modified parameters are determined based on the current error $e(k)$.

$$K_p = K_{pc} K_p^{'} \tag{5.3}$$

$$K_i = K_{ic} K_i^{'} \tag{5.4}$$

Figure 5.6 shows an example of a desired time response. At the beginning, i.e., around 'p_1', we need a big control signal in order to achieve a faster time rise. In order to produce a big control signal, the PI controller should have a large proportional gain ($K_p^{'}$) and a small integral gain ($K_i^{'}$). Around the point 'q_1' in Figure 5.6, we require a small control signal to avoid a large overshoot. That is, the PI controller should have a small proportional gain ($K_p^{'}$) and a large integral gain ($K_i^{'}$). The output response of fuzzy controller parameters, proportional gain ($K_p^{'}$) and the integral gain ($K_i^{'}$) are shown in Figure 5.7.

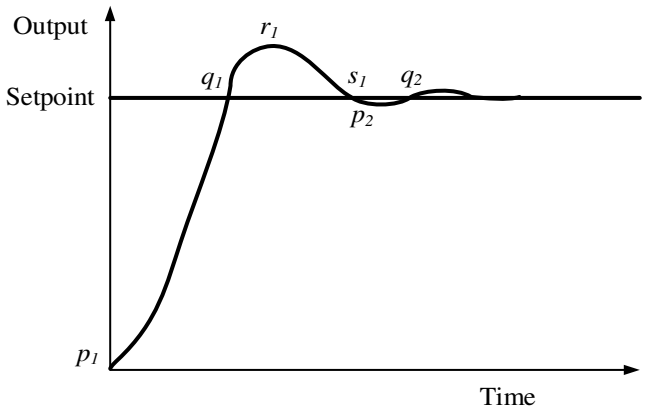

Figure 5.6: Process step response

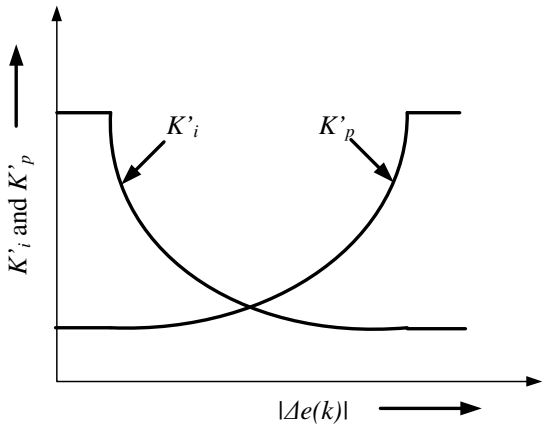

Figure 5.7: Fuzzy controller parameters for $K_p^{'}$ and $K_i^{'}$

The fuzzy rules are extracted from the operator's expertise. Here the rules are driven experimentally based on the step response of the process.

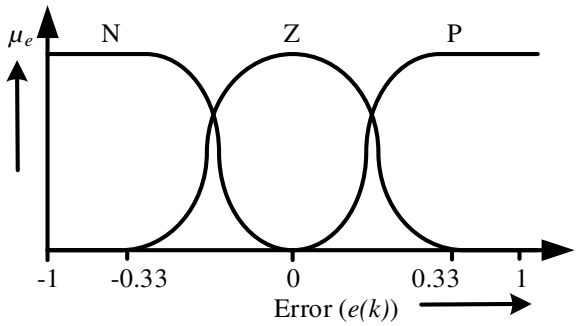

Figure 5.8: Membership functions for $e(k)$

if $e(k)$ is A_m then $K_p^{'}$ is X_m for K_p control.

if $e(k)$ is A_m then $K_i^{'}$ is Y_m for K_i control.

$m = 1, 2, 3 \ldots n$;

Here, A_m, X_m and Y_m are fuzzy sets on the corresponding supporting sets; The membership functions (MF) of these fuzzy sets for $e(k)$ is shown in Figure 5.8.

where, N = negative, P = positive and Z = approximately zero.

The set of fuzzy sets of $e(k)$ are made for determining the parameters $K_p^{'}$, $K_i^{'}$ as follows:

For $K_p^{'}$,

if $e(k)$ is NE then Out is HO,
if $e(k)$ is ZE then Out is MO,
if $e(k)$ is PE then Out is HO.

For $K_i^{'}$,

if $e(k)$ is NE then Out is LO,
if $e(k)$ is ZE then Out is MO,
if $e(k)$ is PE then Out is LO.

where, 'NE' is negative error; 'ZE' is zero error; 'PE' is positive error; 'HO' is high output; 'MO' is medium output; 'LO' is low output.

The m^{th} rule is μ_m is obtained by

$$\mu_m = \mu A_m[e(k)] \tag{5.5}$$

where 'μA_m' is the *MF* value of the fuzzy set 'A_m' given a value of $e(k)$. Based on 'μ_m', the values of '$K_p^{'}$', '$K_i^{'}$' for each rule are determined from their corresponding membership functions. By using the membership functions in Figure 5.8, we have the following condition:

$$\sum_{m=1}^{n} \mu_m = 1 \tag{5.6}$$

Then defuzzification yields the following

$$K_p^{'} = \sum_{m=1}^{n} \mu_m X_m \tag{5.7}$$

$$K_i^{'} = \sum_{m=1}^{n} \mu_m Y_m \tag{5.8}$$

Here, 'X_m' and 'Y_m' are the values of '$K_p^{'}$' and '$K_i^{'}$' corresponding to the grade for the m_{th} rule. The proposed fuzzy gain scheduling-PI controller is implemented in simulation and real time. Their response is analyzed in greater details in Chapter 6.

5.4 Summary

In this chapter, tuning of PI controller's parameters using Zeigler-Nichols method and the fuzzy logic controller has been discussed in detail. The appropriateness of fuzzy gain scheduling PI controller for speed control under dynamical conditions is explored.

Chapter - 6

Digital Implementation of Z-Source Inverter Fed IM Drive

Traditionally, the speed drives are designed using analog controllers with low price discrete components as they are easily available. The drawbacks of analog systems like aging, temperature drift, and poor sensitivity render them unreliable. Regular maintenance is required for these controllers. Moreover, any upgradation is difficult as they are designed through hardware. A high performance digital signal processor (DSP) or micro-controller eliminates drifts and external influences. They perform with high-resolution control, multi-tasking operations and minimize control loop delays. These improvements reduce offset errors, improve dynamic behavior and consequently lead to the reduction of the system size, cost and improved reliability.

To align with above advantages this chapter presents the real time implementation of the Z-source inverter fed induction motor drive. The speed and torque of induction motor was controlled by indirect field oriented control method with modified space vector pulse width modulation technique using TMS320F28335 DSP [96-97]. The schematic of digital implementation of speed control is given in Figure 6.1. The entire proposed algorithm is implemented in 6 levels. The CCS5.4 software with GUI composer by Texas instruments facilitates integrated environment for development of target application [98-99]. The algorithm is programmed using CCS5.4 software, sequences are shown in flow chart in Figure 6.2. The DSP executes the algorithm using the analog inputs to generate gating pulses for the inverter switches with required modulation and shoot-through time for speed and DC-link voltage control.

6.1 Level 1: Implementation of Space Vector Pulse Width Modulation

The field oriented control mainly works on decoupling the torque and flux like DC machine. Here, the torque is related to the line voltage and the speed is related directly to the frequency. For space vector pulse width modulation inverter fed induction motor has the line voltage relationship as given below,

$$V_L = 0.707\, mV_{DC} \tag{6.1}$$

where 'm' is the modulation index, 'V_{DC}' is the DC voltage supplied to the inverter.

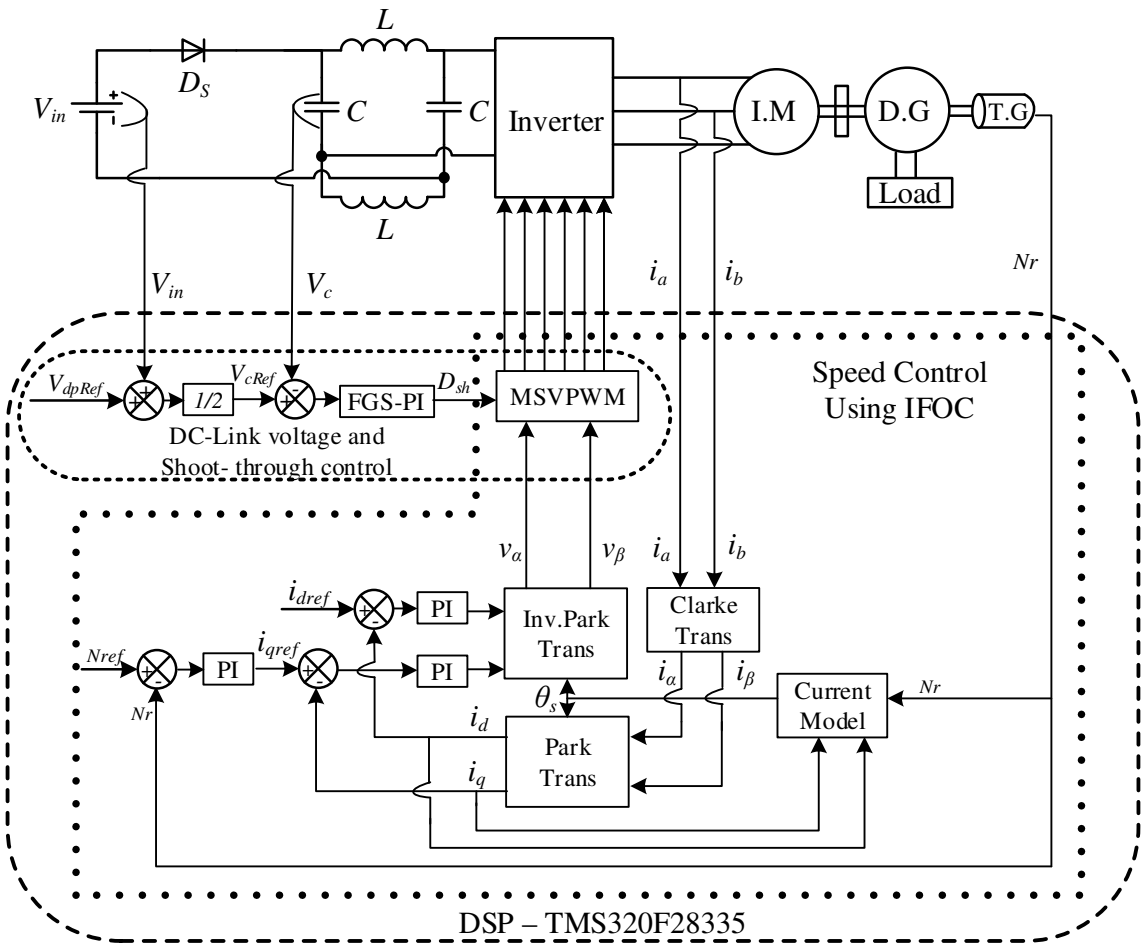

Figure 6.1: Schematic diagram of Z-source inverter fed induction motor coupled with DC generator

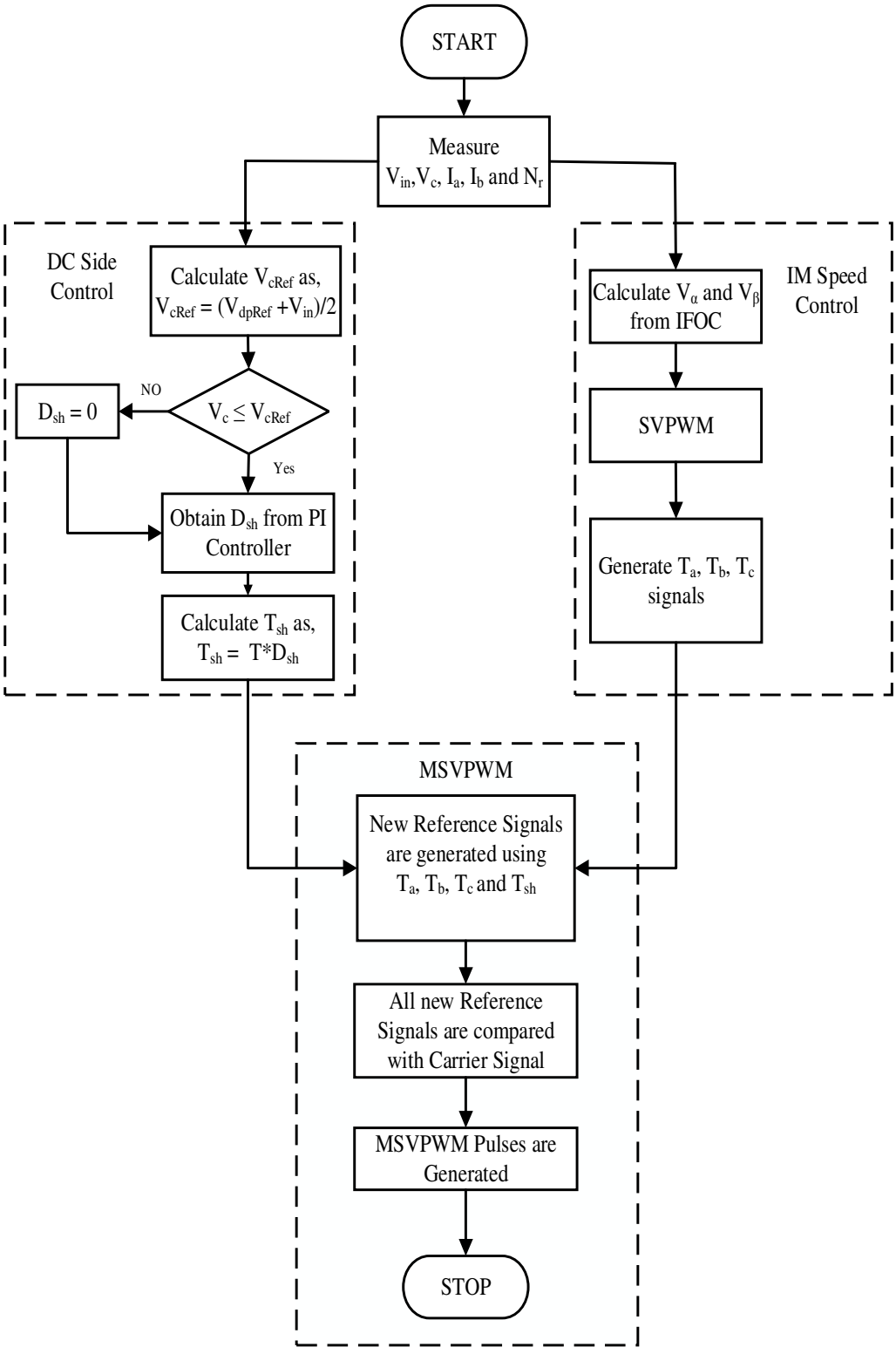

Figure 6.2: Flow chart of IFOC-modified space vector pulse width modulation

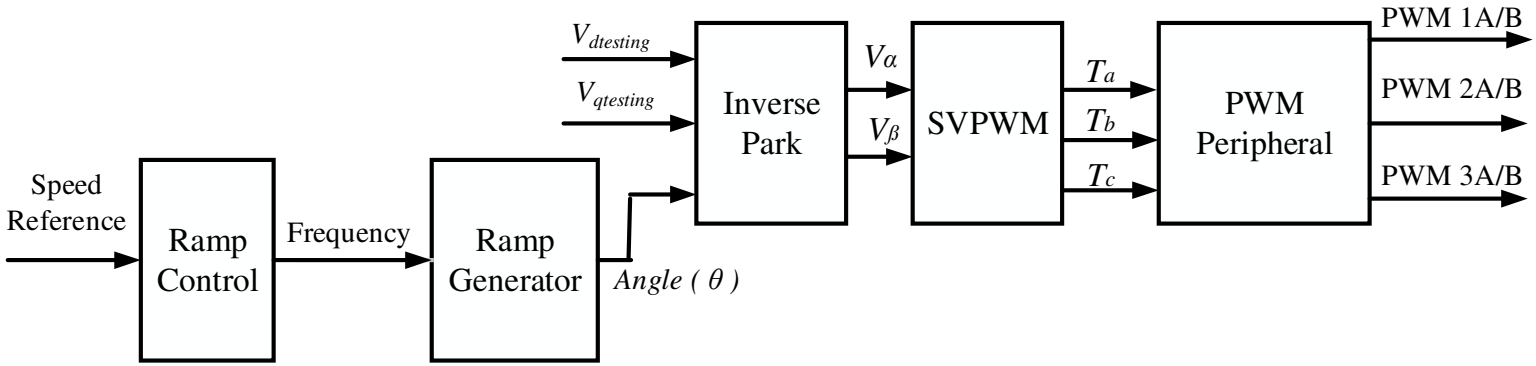

Figure 6.3: Level 1: Space vector pulse width modulation implementation

Here, all quantities will be expressed in the per unit system. The base values are as follows:

- Speed = 3000 rpm
- Line-line voltage = 565 V
- Current = 3.5 A

The frequency supplied to the motor directly affects the speed of the motor and the relation stands as.

$$n = 120\frac{f_{supply}}{P} \tag{6.2}$$

where '*f*' signifies the frequency and '*P*' is the number of poles in a motor. Thus frequency and voltage magnitude can independently change in this model. The signal flow graph of level-1 is shown in Figure 6.3.

The level-1 consists of five modules namely:

i Ramp controller module

ii Ramp generator module

iii Inverse park module

iv Space vector generator module and

v PWM module

The speed reference 0.25 corresponding to a 750 rpm speed given as input to the ramp controller module as a target value. This module provides a constant output, which is then given as an input to the ramp generator module.

The ramp generator module output is synchronous angle 'θ', which is given as an input to the inverse park transformation module that signifies the frequencies of the output AC voltages of the inverter. The other testing inputs to the inverse park transformation module are '$V_{dtesting}$' and '$V_{qtesting}$' which determine the modulation index '*m*', which in turn determines the magnitude of generated AC voltage from equtaion (6.1)

The space vector generator module inputs are stationary reference frame voltages, these will come from the inverse park transformation module. The inverse park transformation module performs the following equations [100].

$$V_\alpha = V_{dtesting}\cos\theta - V_{qtesting}\sin\theta \tag{6.3}$$

$$V_\beta = V_{dtesting}\sin\theta + V_{qtesting}\cos\theta \tag{6.4}$$

The outputs of inverse park module are 'V_α' and 'V_β' shown in Figure 6.4, which are two sinusoidal waves of equal magnitude with a phase difference of 90 degrees. The peak magnitude of these sine waves is given by

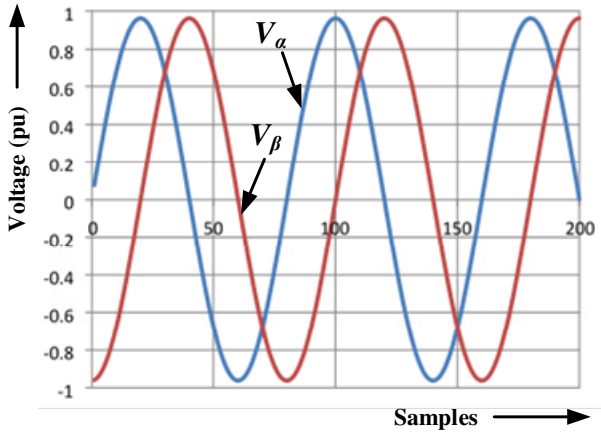

Figure 6.4: The V_α and V_β outputs of the inverse park module

$$\hat{V}_\alpha = \hat{V}_\beta = \sqrt{V^2_{dtesting} + V^2_{qtesting}} \tag{6.5}$$

These 'V_α' and 'V_β' sine waves are supplied as inputs to the space vector pulse width modulation generator module. This module adds third harmonic oscillations and generates three sinusoidal wave forms which difference in phase by 120 degrees with a peak magnitude equal to the peak magnitude of 'V_α' and 'V_β' wave-forms shown in Figure 6.5.

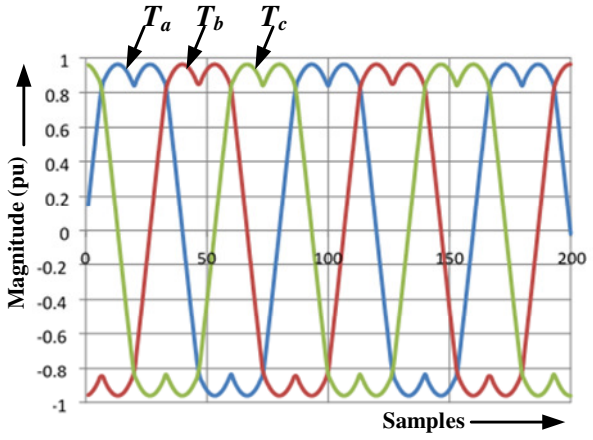

Figure 6.5: The T_a, T_b, T_c outputs of the space vector generator module

These three waves actually signify the duty ratios of pulse width modulated register values. These three wave-forms are given as input to the pulse width modulation (PWM) module; it has an inbuilt high frequency (10K Hz) triangular wave generator. The three wave forms are compared with triangular wave and then the pulses are generated depending on a modulation index value '*m*'. The three inputs given to this PWM module are used to generate the pulses which control the 1, 3 and 5 switches of the inverter. The pulses to control 2, 4 and 6 switches are completely out of phase signals of the three signals used to control 1, 3 and 5 switches.

6.2 Level 2: Implementation of Feed-Back System

The system in Level 1 is improved to include two more modules, namely Clark and Park transformation modules. The clark transformation module converts balanced three-phase induction motor currents into balanced two-phase orthogonal stationary systems. The park transformation module converts vectors in balanced two-phase orthogonal stationary systems into an orthogonal rotating reference frame.

The stator currents and voltages are sensed from current sensors (LA-55P) and voltage sensors (LV-25P) respectively. The sensor outputs are fed to the ADCs of the DSP shown in Figure 6.6. The feed-back circuit consists of a current sensor and a DC offset circuit. The necessity of this DC offset circuit is due to ADC which can take an input voltage between 0 to 3 V. The digital output of the ADC is manipulated to obtain the actual stator current values in pu. The two sensed stator currents are 'I_A' and 'I_B', which correspond to the line currents of the '*A*' and '*B*' legs of the induction motor. The motor currents are balanced then,

$$I_A + I_B + I_C = 0 \tag{6.6}$$

where 'I_A', 'I_B' and 'I_C' are the phase currents.

$$I_A = I\cos\theta \tag{6.7}$$

$$I_B = I\cos(\theta - 120^\circ) \tag{6.8}$$

$$I_C = I\cos(\theta - 240^\circ) \tag{6.9}$$

This Clarke module implements the following equations:

$$I_\alpha = I_A \tag{6.10}$$

$$I_\beta = \frac{(2I_B + I_A)}{\sqrt{3}} \tag{6.11}$$

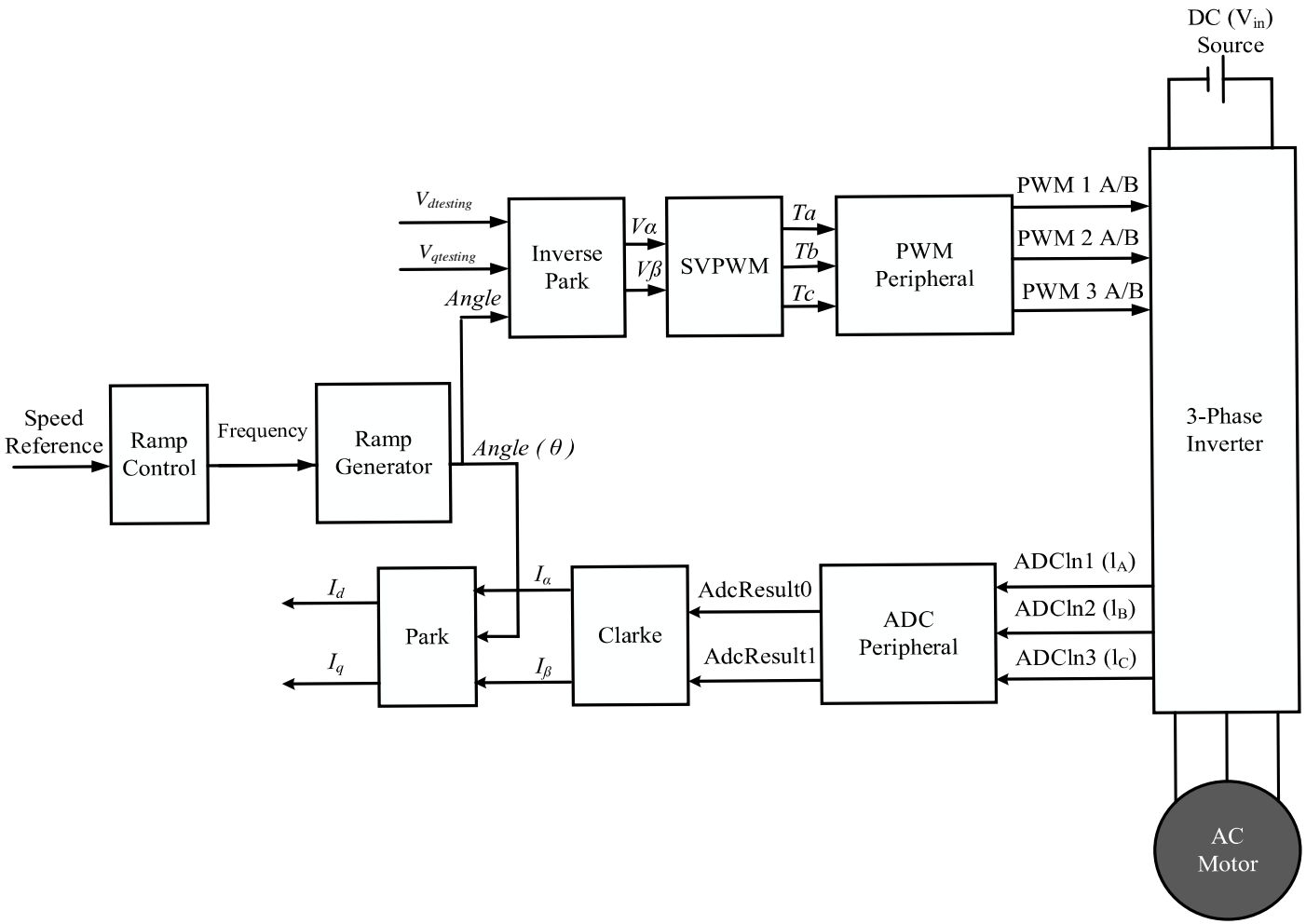

Figure 6.6: Level 2: Incremental system of ADC feed-back system

which result in,

$$I_\alpha = I\cos\theta \tag{6.12}$$

$$I_\beta = I\sin\theta \tag{6.13}$$

The outputs of the ADC are given as input to the clarke module, as shown in Figure 6.7. The clarke module converts balanced three phase quantities into balanced two phase quadrature quantities [101].

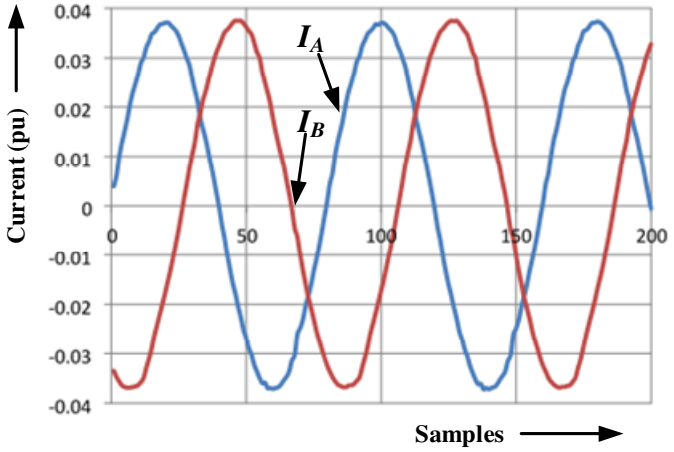

Figure 6.7: Inputs of the Clark module

The outputs of the clarke module are denoted as 'I_α' and 'I_β' which are two sinusoidal waves of equal magnitude with `A' phase difference of 90 degrees as shown in Figure 6.8.

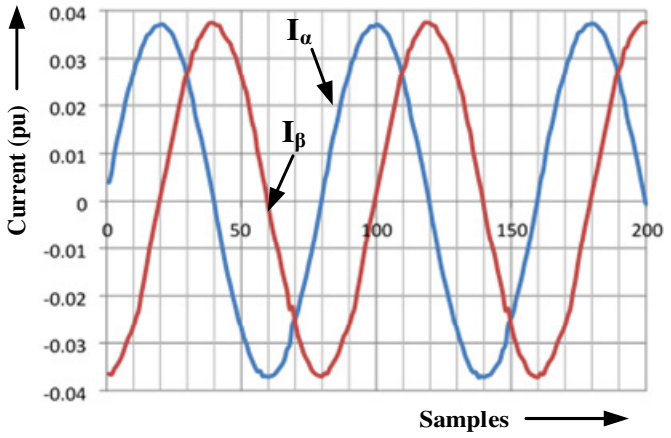

Figure 6.8: Outputs of the Clark module

These are provided as an input to the park transformation module which converts the 'I_α' and 'I_β' constraints to 'I_d' and 'I_q' in the rotating frame. This module implements the following equations:

$$I_d = I_\alpha \cos\theta + I_\beta \sin\theta \tag{6.14}$$

$$I_q = I_\beta \cos\theta - I_\alpha \sin\theta \tag{6.14}$$

This transformation converts vectors in 2-phase orthogonal stationary system into the rotating reference frame shown in Figure 6.9.

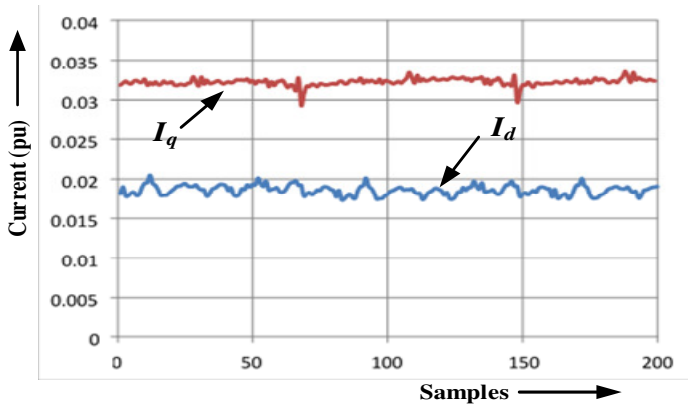

Figure 6.9: Outputs of the Park module

6.3 Level 3: Implementation of PI controller

The system in level 2 is improved to form the level 3 model shown in Figure 6.10. In level 3, torque and flux PI controllers are implemented. The park module outputs 'I_q' and 'I_d' which are given to the torque and flux PI controllers as shown in Figure 6.10. The outputs 'V_q' and 'V_q' of PI controllers are given to the inverse park module.

6.3.1 PI Controller

This PI Controller module implements a basic summing of P & I control law with the following features:

- Programmable output saturation
- Independent reference weighting on proportional path
- Anti-windup integrator reset

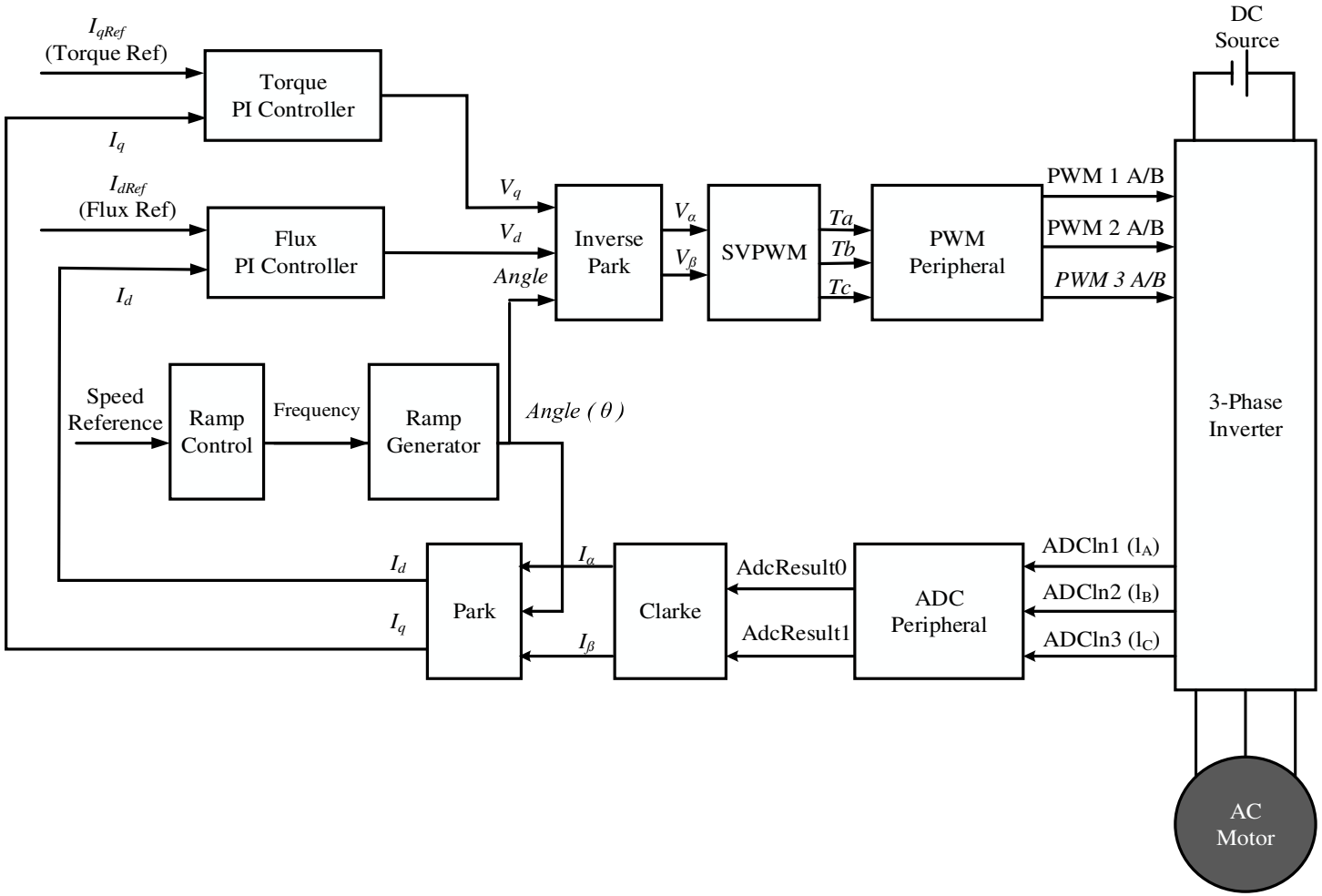

Figure 6.10: Level 3: Incremental system of PI controllers

The PI controller is a sub-set of the PID controller. A block diagram of the internal controller structure is shown in the Figure 6.11.

1. **Proportional Path:** The proportional path is a direct connection between the error term and a summing junction with the integral path. The error term is

$$e(k) = r(k) - y(k) \tag{6.16}$$

2. **Integral Path:** The integral path consists of a discrete integrator which is pre-multiplied by a term derived from the output block. The term w_1 is either zero or one, and provides a means to disable the integrator path when output saturation occurs. This prevents the integral term from 'winding up' and improves the response time on recovery from saturation. The integrator law used is based on a backwards approximation.

$$u_i(k) = u_i(k - 1) + K_i e(k) \tag{6.17}$$

3. **Output Path:** A block diagram of the PI controller structure is shown Figure 6.11.

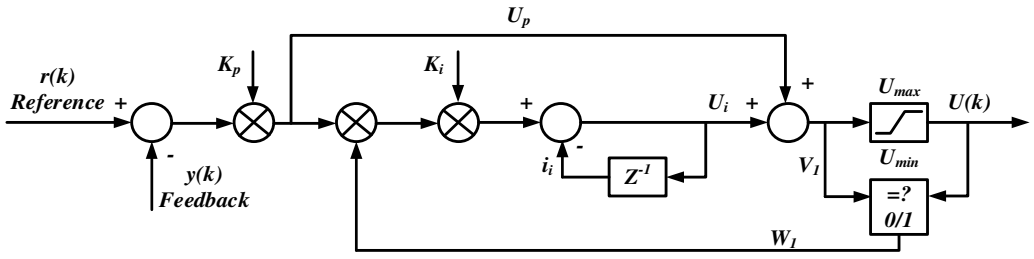

Figure 6.11: PI controller block diagram

The output path contains a summing block to sum the proportional (K_p) and integral (K_i) controller terms. The result is then saturated according to user programmable upper ($U_{\max}$) and lower ($U_{\min}$) limits to give the controller output. The pre-and post-saturated terms are compared to determine whether saturation has occurred, and if so, a zero or one result is produced which is used to disable the integral path. The output path law is defined as follows:

$$v_1(k) = u_p(k) + u_i(k) \tag{6.18}$$

$$u(k)=\begin{cases} U_{\max} : v_1(k) > U_{\max} \\ U_{\min} : v_1(k) < U_{\min} \\ v_1(k) : U_{\min} < v_1(k) < U_{\max} \end{cases} \tag{6.19}$$

$$w_1(k)=\begin{cases} 0 : v_1(k) \neq u(k) \\ 1 : v_1(k) = u(k) \end{cases} \tag{6.20}$$

Tuning of PI controller: A suggested general technique for Zeigler-Nichols based tuning the controller is now described.

Step 1: The integral is set to zero and proportional gain is set to one.

Step 2: Gradually the proportional gain variable (K_P) is adjusted while observing the step response to achieve optimum rise time and overshoot compromise.

Step 3: If necessary, integral gain (K_i) is gradually increased to optimize the return of the steady state output to nominal. The controller will be very sensitive to this term and may become unstable so be sure to start with a very small number. Integral gain will result in an increase in overshoot and oscillation, so it may be necessary to slightly decrease the K_P term again to find the best balance. It should be noted that if the integral gain is used then set to zero, a small residual term may persist in u_i.

6.4 Level 4: Implementation of Speed Sensor

The system in level 4 is improved to include an extra block namely the speed converter module as shown in Figure 6.12. The induction motor speed is measured by AC tacho-generator. The outputs of this tacho-generator is sinusoidal AC voltage, it has peak-peak voltage is around 70 V. This much high voltage we cannot give to the conteoller, because controller input pins are take unipolar voltage in between 0 to 3V. Due that tacho-generator output sinusoidal AC voltage is step down and converted into pulses through the OP-AMP based concerter circuit. The converter circuit converts sinusoidal wave-form into pulses, the pulse converter circuit descried in 'Appendex-A'. These pulses are supplied to the CAP module of DSP controller, which converts the pulses in form of count. These count will give to the speed converter module, it calculates speed of the induction motor.

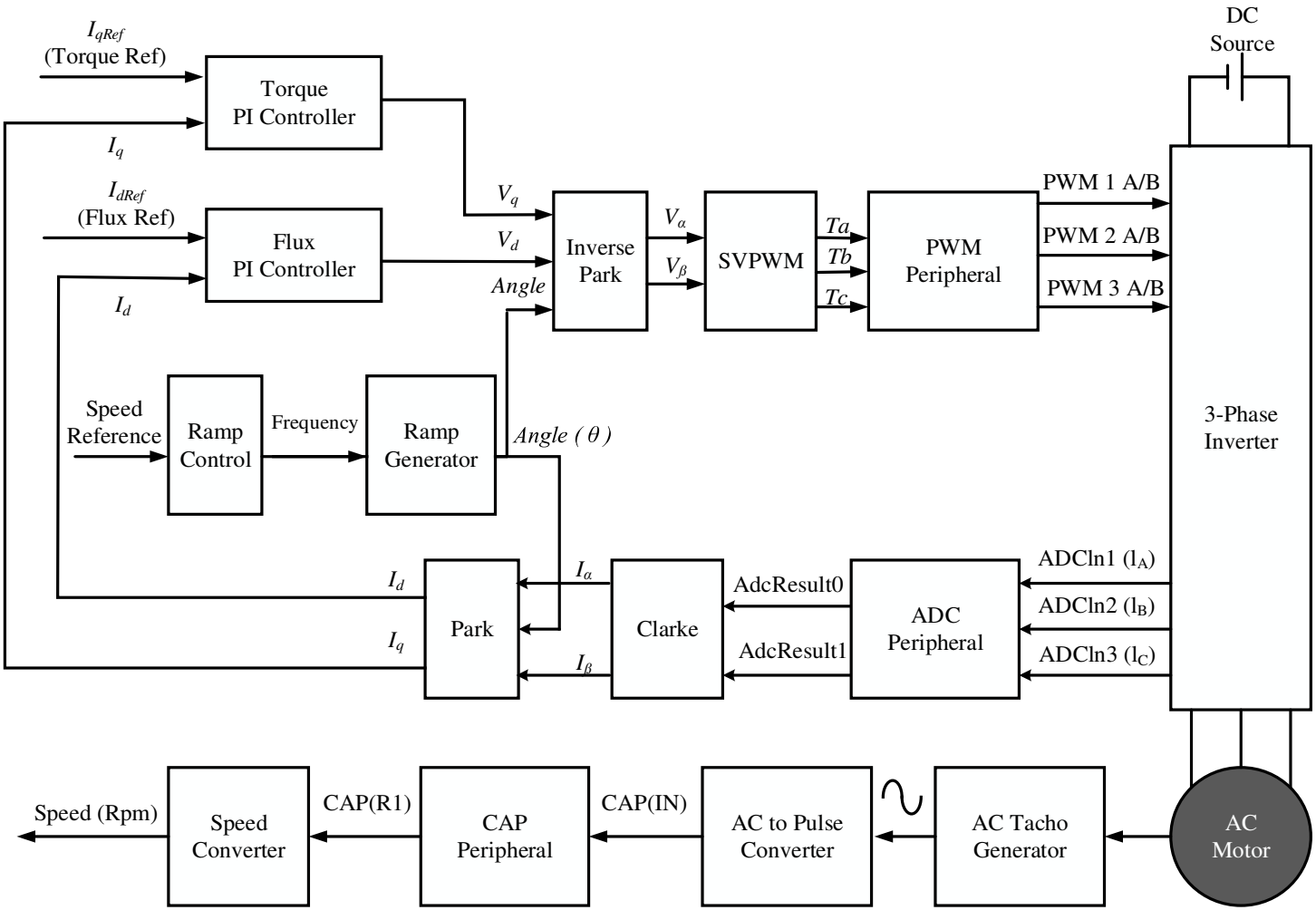

Figure 6.12: Level 4: Incremental system of speed sensor

6.5 Level 5: Implementation of Current Model and Speed PI Controller

In level 5 synchronous theta is calculated, this module takes the input as the speed that is output from speed module which is from the tacho-generator in level 4, along with the outputs of the park module, 'I_d' and 'I_q'. This information is taken and is used to calculate the synchronous angle (θ). For speed control, reference speed and measured speeds are given to the speed PI controller. The speed PI controller output is the 'I_{qref}' (torque reference) shown in Figure 6.13.

6.5.1 Current Model

With the asynchronous drive, the mechanical rotor angular speed is not equal to the rotor flux angular speed. This implies that the necessary rotor flux position cannot be detected directly by the mechanical position sensor used with tachometer. The current model module generates the synchronous theta or angle with help of motor currents and speed.

The current model consists of implementing the following two equations of the motor in *d*, *q* reference frame:

$$i_d = T_r \frac{di_{mR}}{dt} + i_{mR} \tag{6.21}$$

$$f_s = \frac{1}{\omega_b}\frac{d\theta}{dt} = n + \frac{i_q}{T_R i_{mR} \omega_b} \tag{6.22}$$

where, 'θ' is the rotor flux position, 'i_{mR}' is the magnetizing current, $T_R = \frac{L_R}{R_R}$ is the rotor time constant with 'L_R' the rotor inductance and 'R_R' the rotor resistance, 'f_s' is the rotor flux speed, 'ω_b' is the electrical nominal flux speed.

The rotor time constant is critical to the correct functioning of the current model as it is this system that outputs the rotor flux speed that will be integrated to get the rotor flux position.

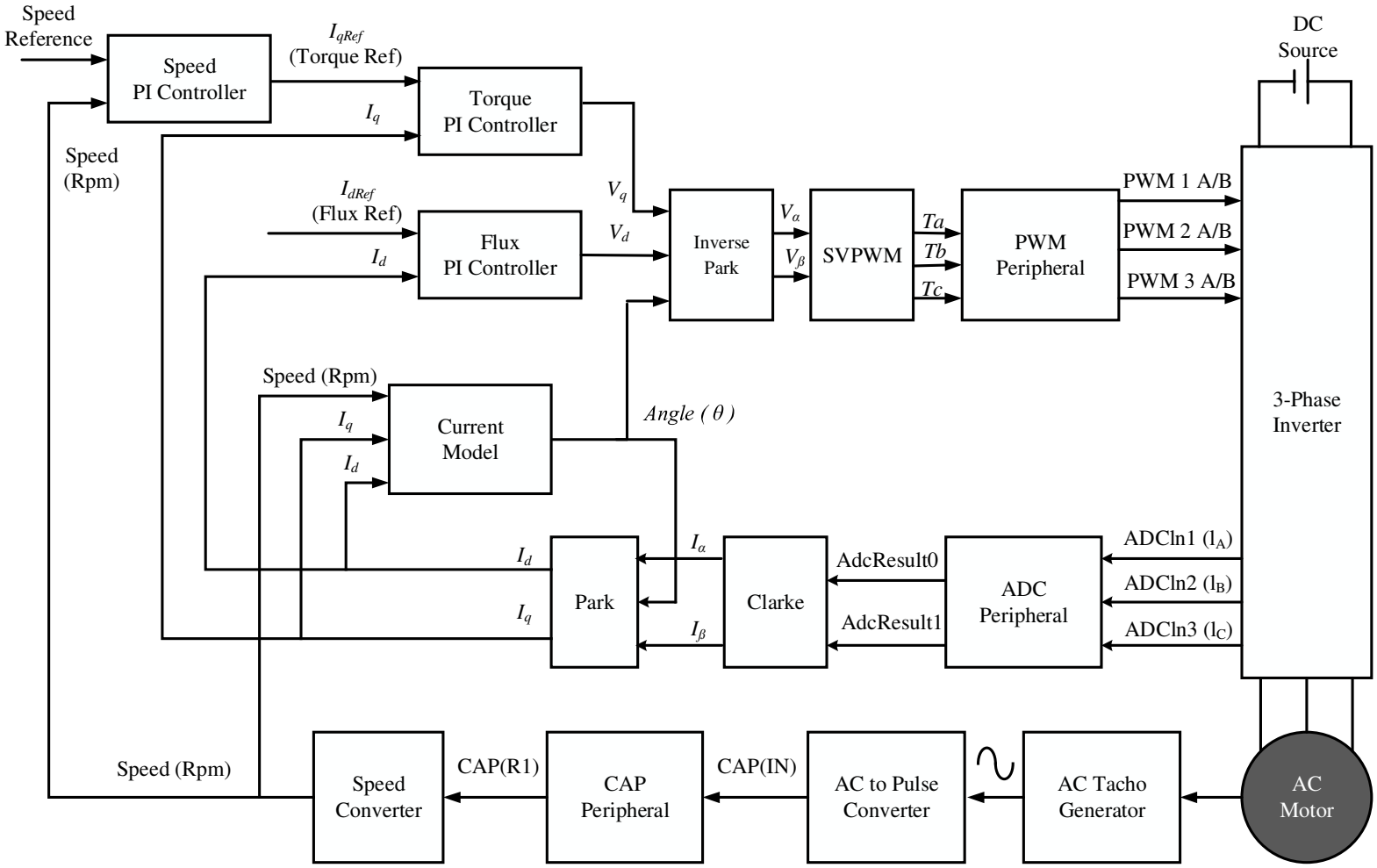

Figure 6.13: Level 5: Incremental system of current model and speed PI controller

Assuming that $i_{qk=1} \approx i_{qk}$ the above equations can be discretized as follows:

$$i_{mR_{k+1}} = i_{mR_k} = \frac{T}{T_R}(i_{dk} - i_{mRk}) \tag{6.23}$$

$$f_{Sk+1} = n_{k+1} + \frac{1}{T_R \omega_b} \frac{i_{qk}}{i_m R_{k+1}} \tag{6.24}$$

In this equation system, '*T* 'represents the main loop control period.

Let the two equations constants $\frac{T}{T_R}$ and $\frac{1}{T_R \omega_b}$ be renamed respectively K_t and K_R.

Once the motor flux speed (f_s) has been calculated, the necessary rotor flux position in per-unit (θ) is computed by the integration formula:

$$\theta = \theta_{k-1} + K f_{sk} \tag{6.25}$$

where, $K = Tf_b$.

The current model module constants depend on the motor parameters and need to be calculated for each type of motor. The information needed to do so is the rotor resistance, the rotor inductance (which is the sum of the magnetizing inductance and the rotor leakage inductance.

6.6 Level 6: Implementation of DC-Link Voltage Control

The DC-link voltage is pulsating and it is controlled by employing the capacitor voltage control as shown in Figure 6.14. The reference value of the capacitor (V_{cRef}) is calculated based on the reference DC-link voltage and the input voltage of the Z-network structure. By controlling the capacitor value [$V_{cRef} = (V_{in} + V_{dp})/2$] through the capacitor voltage PI controller then the peak DC-link voltage is controlled precisely. Additionally, the input voltage interruption elimination is also improved. The capacitor voltage PI controller parameters are tuned using Ziegler-Nichols method, and then the peak DC-link voltage control is not satisfactory under dynamic conditions. The fuzzy logic controller is the nonlinear and fast controller. Due to this fuzzy based hybrid PI controller is implemented, that is fuzzy gain scheduling PI controller. The fuzzy gain scheduling PI controller is already discussed in Chapter 5.

The all six levels are implemented in simulation, hardware and the results are discussed in Chapter 7.

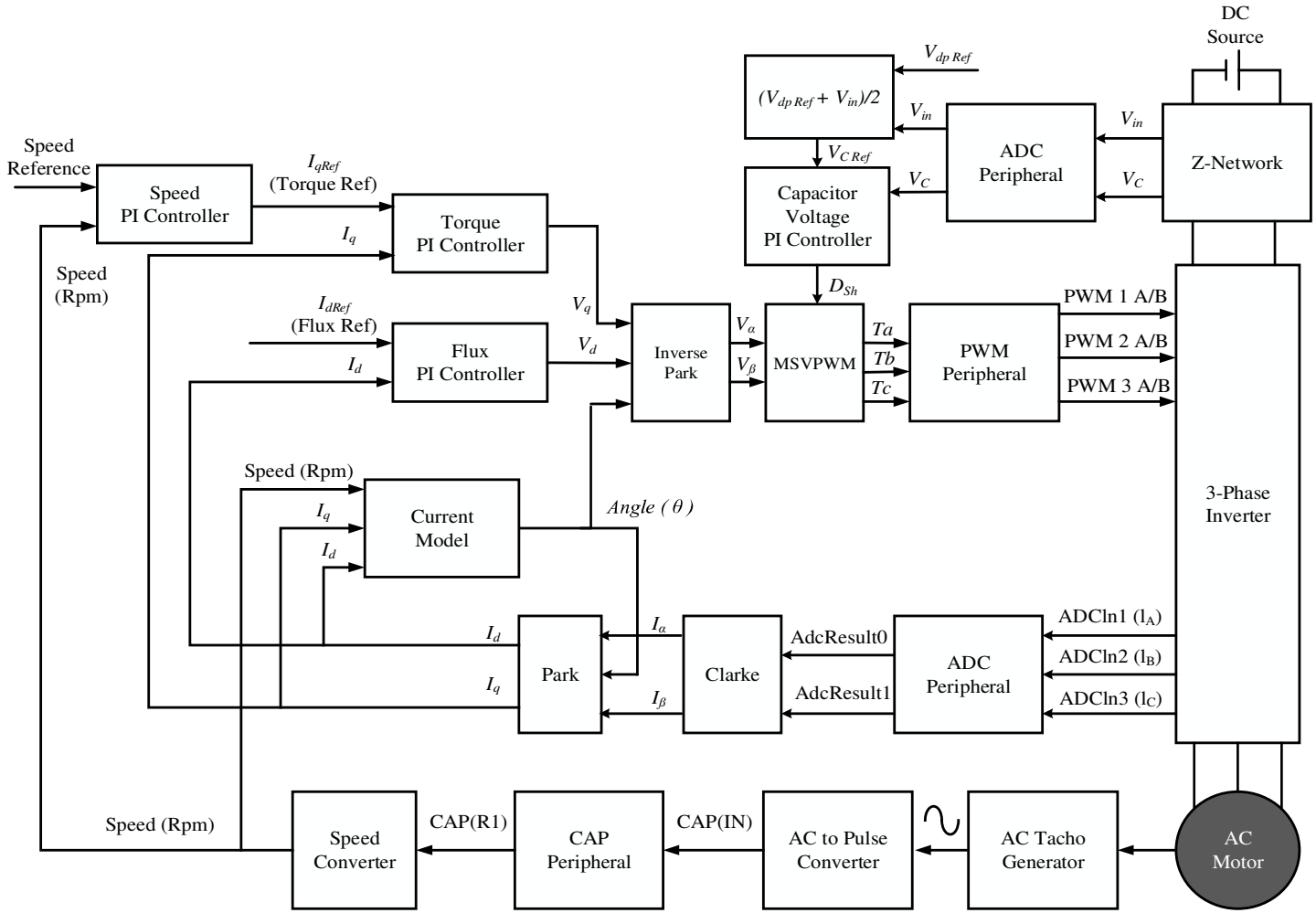

Figure 6.14: Level 6: Incremental system of peak DC-link voltage control

6.7 Summary

The sequential digital implementation of speed control of Z-source inverter fed induction motor drive with IFOC is explained in six levels.

Chapter - 7

Simulation and Experiment: Results and Analysis

In this chapter, the proposed algorithm is tested on MATLAB/SIMULINK plate form and the same is validated on prototype Z-source inverter (ZSI) fed induction motor setup in laboratory. The Z-source inverter fed induction motor emulating electrical vehicle (EV) subjected to various dynamical conditions, speed and DC-link voltage were measured. The investigations were carried out the inferences on the performance of the drive were drawn and presented in subsequent sections.

7.1 VSI Fed Induction Motor Drive

The induction motor set up is simulated with voltage source inverter (VSI) and the results are obtained for various operating conditions. The DC-link voltage of inverter is 600 V. The simulation diagram is shown in Figure 7.1 and the motor parameters are given in Table 7.1.

The system has a reference speed of 750 rpm and simulation is performed for 2 cases:

1. Change in load-torque with Speed Constant (emulation of hill climbing of electrical vehicle).
2. Change in speed with load (acceleration and deceleration emulation of stop and go of the electrical vehicle).

7.1.1 Change in Load-Torque with Speed Constant: Hill Climbing of Electric Vehicle

The load-torque is changed in different steps to study the response of the system. The initial load torque on the system is 5 N.m and is changed gradually. The motor speed is kept constant at 750 rpm throughout the process.

Now, when the load-torque is increased from 5 N.m to 12.5 N.m, there is drastic undershoot in the speed of the motor. There is a swivel that persists before it returns to the true value of 750 rpm. The corresponding DC-link voltage drops as expected. As load-torque is increased to 25N.m, there is an even further undershoot with a larger settling time in the speed response of the induction motor. The final change in load torque is 25 N.m to 35 N.m.

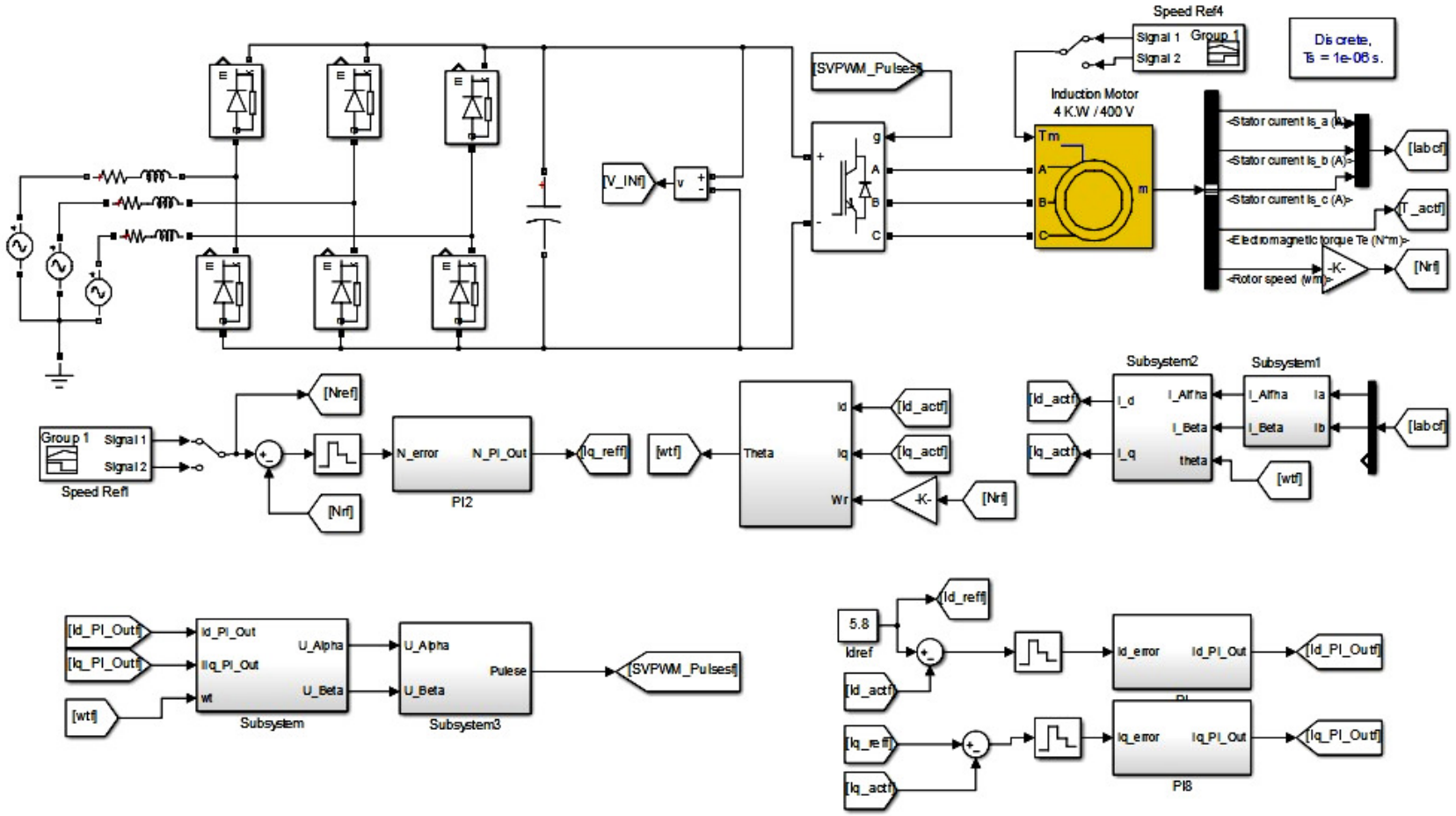

Figure 7.1: Simulation diagram of VSI fed induction motor drive

Table 7.1: Induction motor parameters

Parameters	Values
Output Power	5.4 hp
Line Voltage	400 V
Line Current	7.2 A
Frequency	50 Hz
No of Poles P	4
Speed	1430 rpm
Stator Resistance, R_s	1.405 Ohm
Rotor Resistance, R_r	1.395 Ohm
Stator Inductance, L_s	0.175 H
Rotor Inductance, L_r	0.175 H
Mutual Inductance, L_m	0.722 H

Hence, the change in load-torque of the system at constant speed does not bode well for the motor speed with a VSI. The observations are illustrated in Figure(s) 7.23a, 7.2b and 7.2c.

The characteristic responses of peak overshoot, settling time and drop in DC-link voltages of the system are summarized in the Table 7.2.

Table 7.2: The motor speed performance with step change in load torque

Load-torque	Peak undershoot	$T_{settling}$	V_{DC} drop from 600 V
5 to 12.5 N.m	11.1 %	0.25 sec	585 V
12.5 to 25 N.m	18.6 %	0.32 sec	567 V
25 to 35 N.m	15.3 %	0.29 sec	550 V

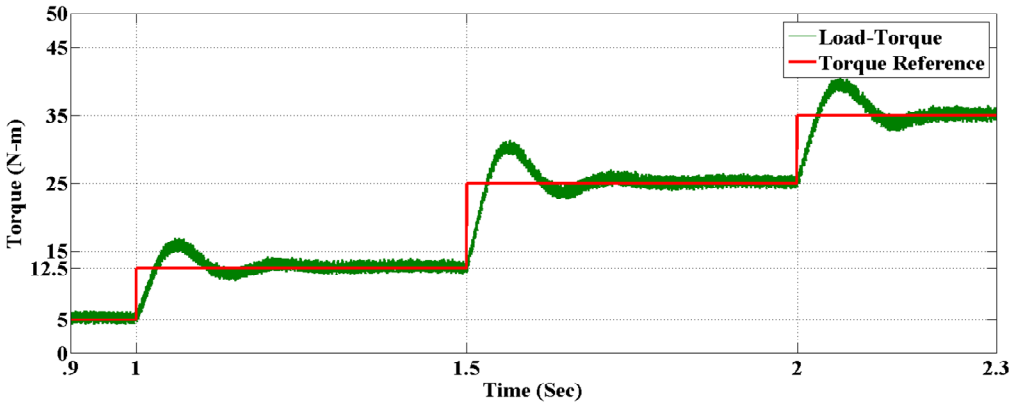

(a) Induction Motor Shaft Torque

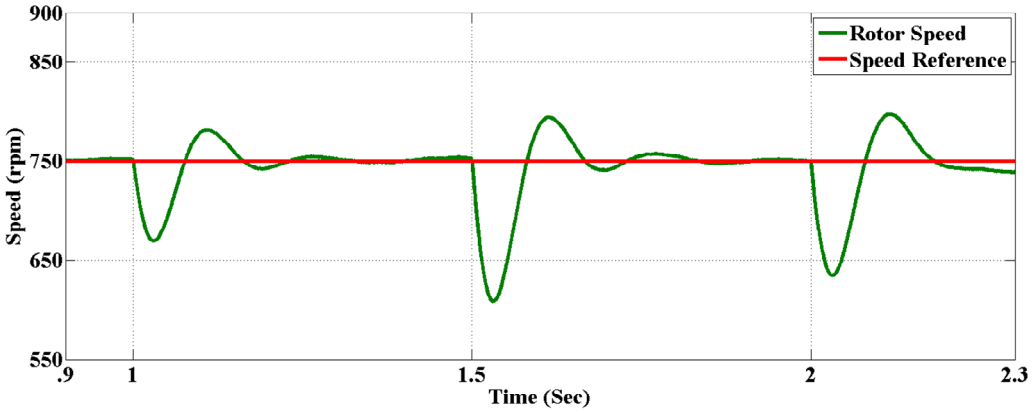

(b) Induction Motor rotor speed

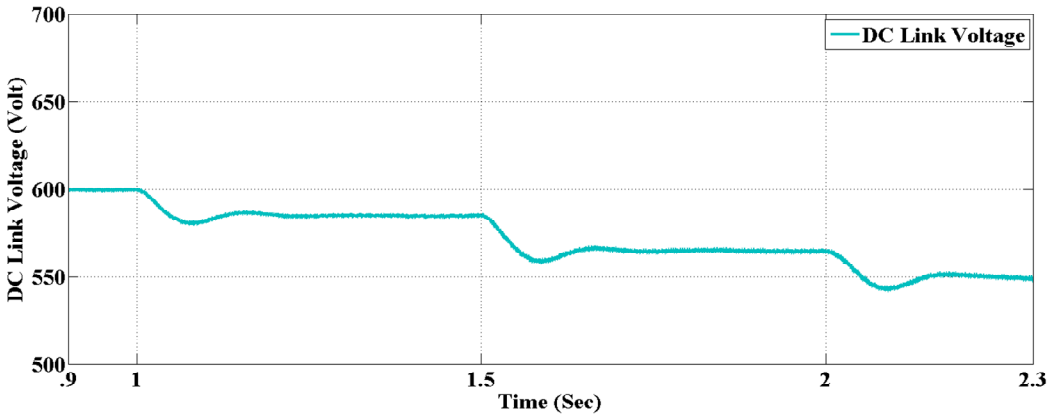

(c) DC-link Voltage

Figure 7.2: VSI Fed induction motor drive with change in load-torque

7.1.2 Change in Speed with Load: Acceleration and Deceleration of EV

The simulation of the following case has been carried out by changing the speed of the motor in a step-wise manner. Initially, the induction motor is loaded with 25 N.m. This load-torque is kept constant throughout the operation. Now, as we increase the speed from the reference of 750 rpm to a value of 1000 rpm, the load-torque shoots up before becoming constant again as expected whereas the DC-link voltage drops due to the overshoot in the speed response of the system. With a further increase in the speed to 1400 rpm, the DC-link voltage proceeds to drop further. As the speed is decreased back to 1000rpm, a large overshoot in the DC-link voltage is observed. When the speed is finally brought to reference speed 750 rpm, the DC-link voltage shoots up again. These observations are illustrated in the Figure(s) 7.3a, 7.3b and 7.3c.

The characteristic responses of speed peak overshoot and drop in DC-link voltages of the system are summarized in the Table 7.3.

Table 7.3: VSI drive speed performance with reference speed step change

Speed	Speed peak over/under shoot	V_{DC} Drop from 600 V
750 to 1000 rpm	5 %	569 V
1000 to 1400 rpm	6.8 %	532 V
1400 to 1000 rpm	5.6 %	569 V
1000 to 750 rpm	4.8 %	585 V

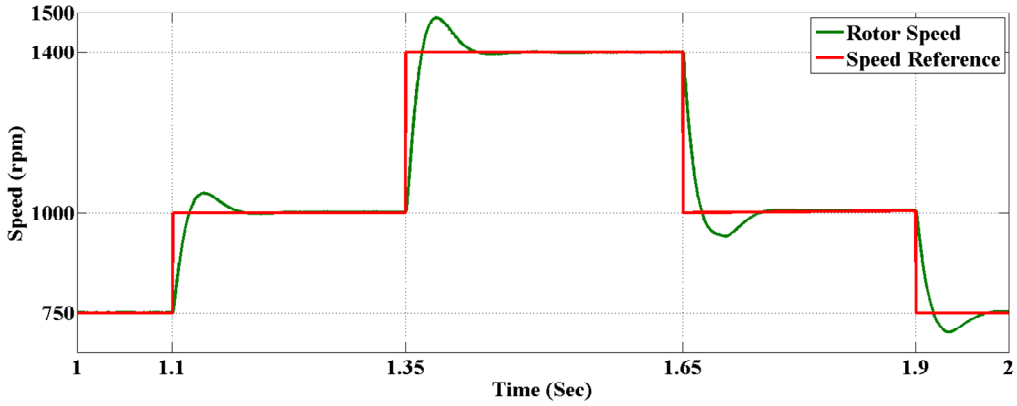

(a) Induction motor rotor speed

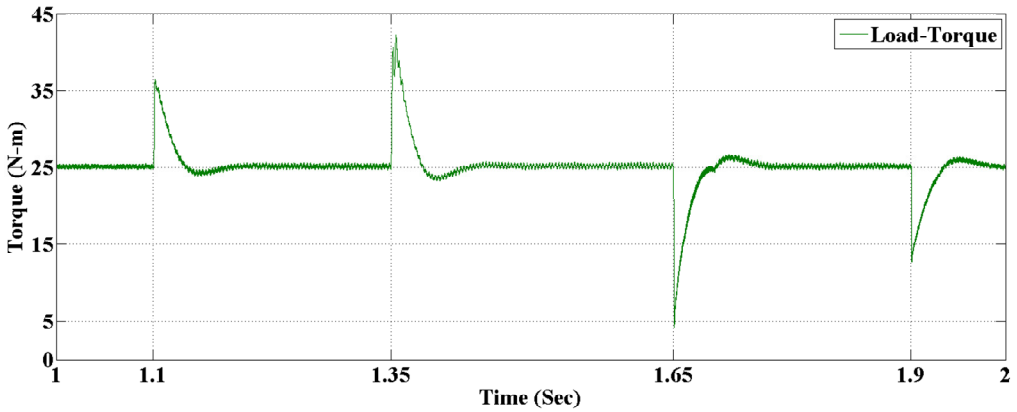

(b) Induction motor shaft torque

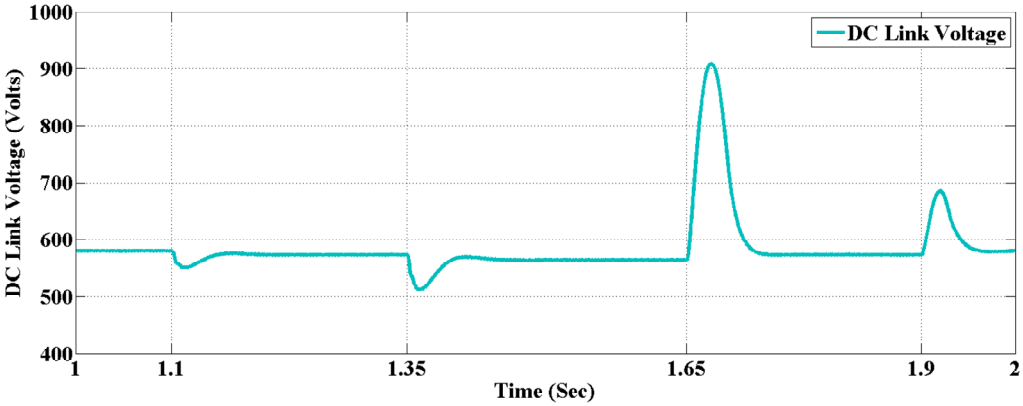

(c) DC-link voltage

Figure 7.3: VSI Fed induction motor drive with change in speed

7.2 VSI Fed Induction Motor Drive: Experimental Results

A 600V DC input voltage connected to a voltage source inverter. The inverter supplies to a 3-phase induction motor coupled to a DC generator. The DC generator is loaded with a bank of resistors. Voltage source inverter fed 3-phase induction motor drive as shown in Figure 7.4. The induction motor parameters and DC generator parameters are given in Tables 7.4 and 7.5. Since the DC generator carries a load, the Induction motor also indirectly sustaining a load. The set up has a speed reference of 750 rpm. The aim is to test the system under two scenarios:

1. Change in load-torque with speed constant (hill climbing and downing - emulation of electrical vehicle).
2. Change in speed with load (acceleration and deceleration emulation of electrical vehicle).

Table 7.4: Induction motor parameters

Parameters	Values
Output power	2.0 hp
Line voltage	400 V
Line current	2.5 A
Frequency	50 Hz
No of poles P	4
Speed	1430 rpm
Stator resistance, R_s	3.63 Ohm
Rotor resistance, R_r	3.25 Ohm
Stator inductance, L_s	0.958 H
Rotor inductance, L_r	0.958 H
Mutual inductance, L_m	0.95 H

Table 7.5: DC generator parameters

Parameters	Parameters
Output power	2 hp
Voltage	50 V
Current	30 A
Speed	1500 rpm
Armature resistance, R_a	1.2 Ohm

We will now discuss the experimental set-up and results for the VSI fed induction motor drive.

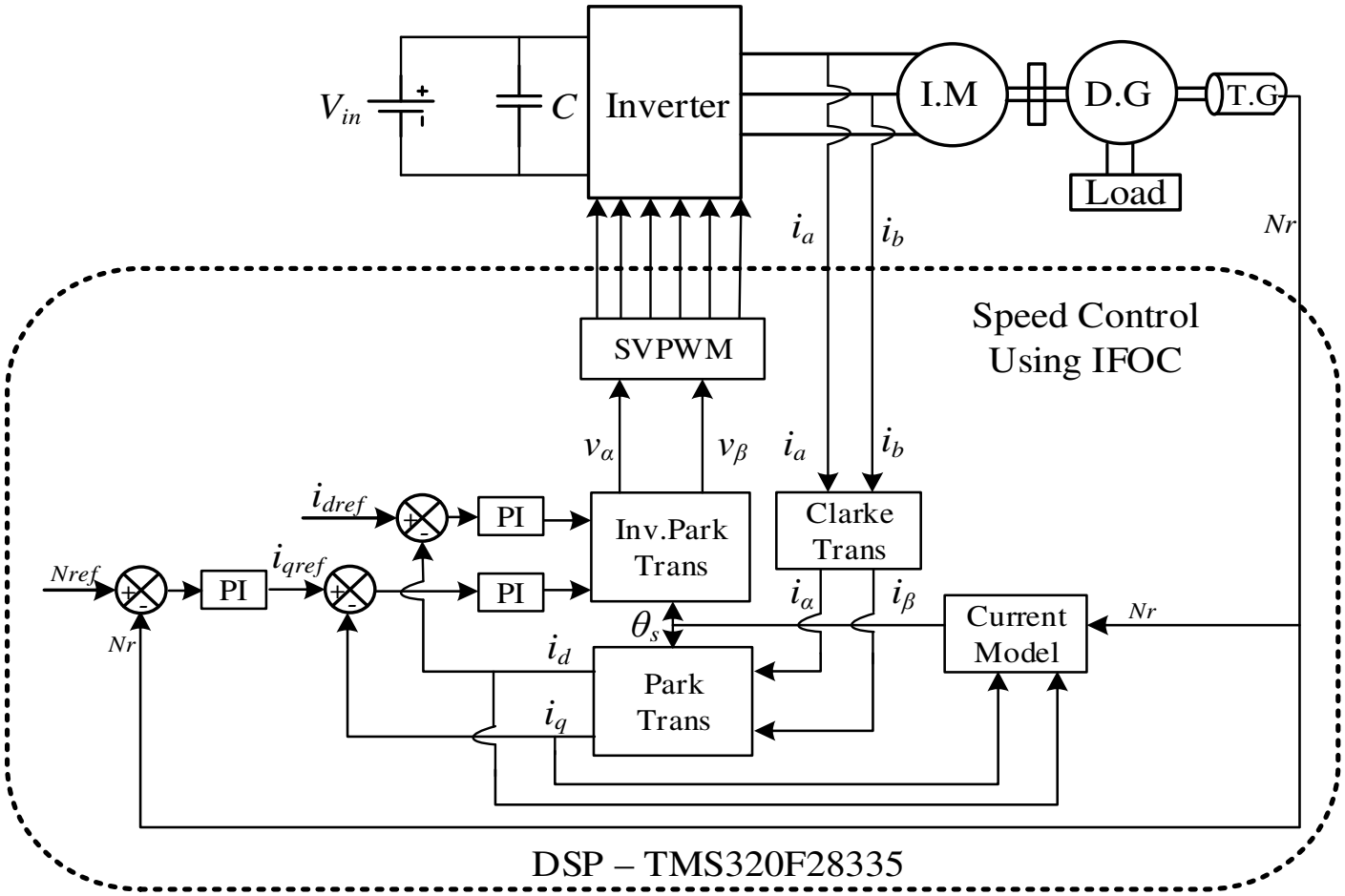

Figure 7.4: Schematic diagram of voltage source inverter fed induction motor coupled with DC generator

7.2.1 Change in Load-Torque with Speed Constant: Hill Climbing and Downing of EV

This scenario will be realized in two steps. First we consider a progressively increasing load with time from no load to overload condition. Then we consider a progressively decreasing load with time from overload to no load condition.

7.2.1.1 Increasing Load Condition: Hill Climbing of EV

The Figure 7.5(a) shows the speed response of the induction motor varying with time. The load applied across the DC generator is increased gradually from no load to overload conditions at instants 20sec (L_{1i}), 40sec (L_{2i}), 60sec (L_{3i}) and 80sec (L_{4i}). The characteristics of the systems' response at each of these instants are summarized in the Table 7.6.

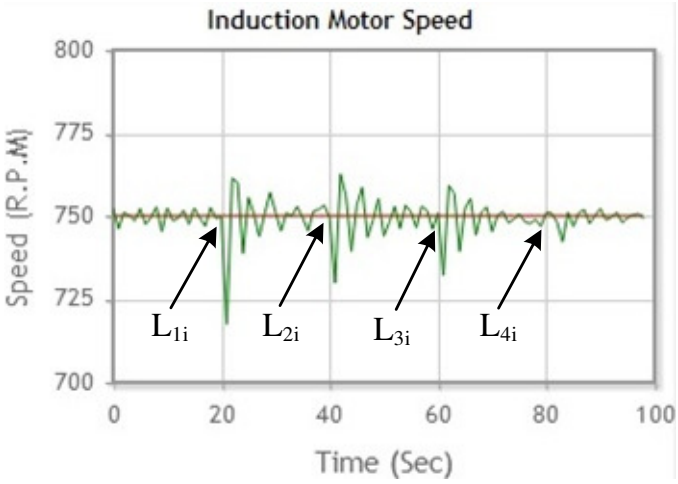

(a) Induction motor rotor speed

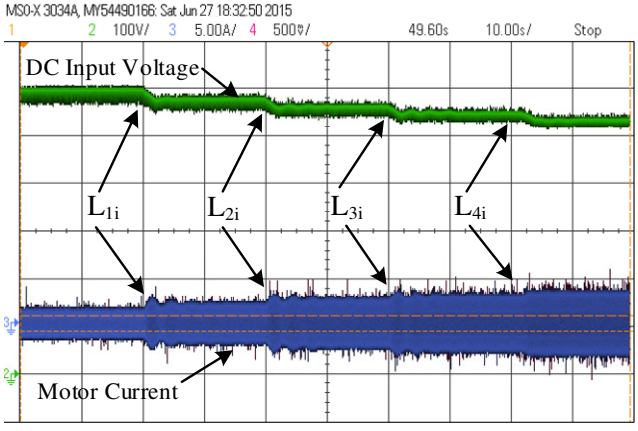

(b) DC-link voltage and induction motor line current

Figure 7.5: VSI Drive with increasing load

The Figure 7.5(b) shows the DC-link voltage and induction motor line current of the system. The drop in voltage at the instants of loading are also noted and summarized in Table 7.6.

Table 7.6: VSI Drive speed performance with increasing load

Load	Current	Peak undershoot	V_{DC} drop from 600 V
L_{1i} = 48%	1.2 A	4.4%	579 V
L_{2i} = 70%	1.8 A	2.9%	559 V
L_{3i} = 96%	2.45 A	2.1%	541 V
L_{4i} = 114%	2.85 A	2%	522 V

7.2.1.2 Decreasing Load Condition: Hill Downing of EV

The Figure 7.6(a) shows the response of the induction motor to the variation in loads at the DC generator end. The DC generator is loaded initially and then decreased from an initially 114% overloaded condition to a no load condition. The drops in load values occur at the time instants of 20sec (L_{1d}), 40sec (L_{2d}), 60sec (L_{3d}) and 80sec (L_{4d}). The Figure 7.6(b) shows the DC-link voltage from 522 V to 600 V and the induction motor line current. The key performance indicators of the system, the current at the loading instances and the corresponding gain in DC-link voltage are also computed and expressed in the Table 7.7.

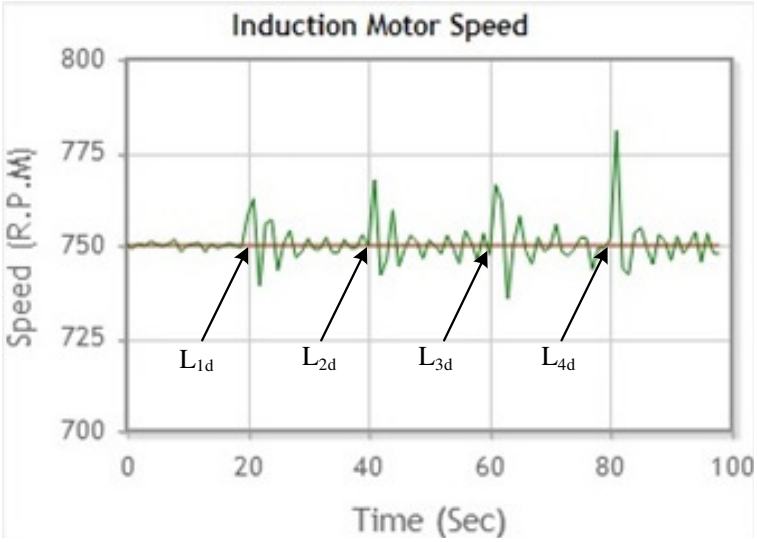

(a) Induction Motor Rotor Speed

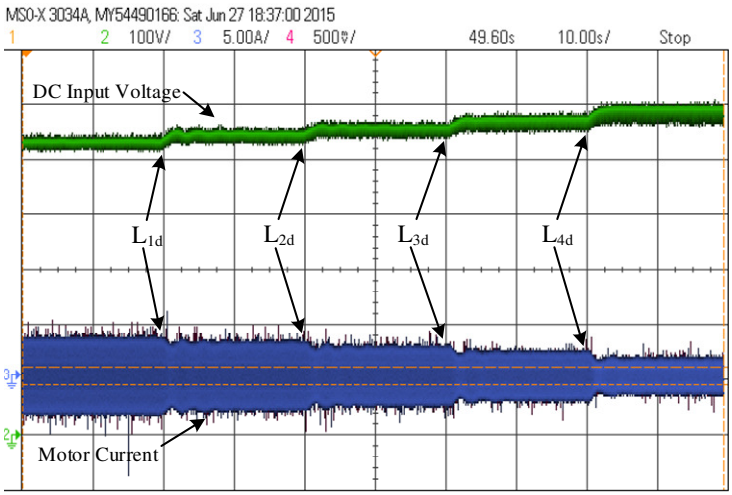

(b) DC-link voltage and induction motor line current

Figure 7.6: VSI Drive with decreasing load

Table 7.7: VSI Drive speed performance with decreasing load

Load	**Current**	**Peak over shoot**	**V_{DC} drop from 600 V**
L_{1d} = 96%	2.45 A	1.6 %	541 V
L_{2d} = 70%	1.8 A	2.1 %	559 V
L_{3d} = 48%	1.2 A	2.3 %	579 V
L_{4d} = 32%	0.8 A	4.1 %	598 V

7.2.2 Change in Speed with Load: Acceleration and Deceleration of EV

In this scenario we first load the DC generator with a set of resistors and then alter the system's speed. Intialy, the drive is load with at 70% of load and the speed is changed to six different states. The system's response characteristics: induction motor speed- peak overshoot/undershoot and changes in DC-link voltage are analyzed.

7.2.2.1 Increasing Motor Speed: Acceleration of EV

The system is initially 70% loaded at 10 sec and kept constant for the next 80 seconds. The speed reference of the system is increased in steps.

750 rpm → 850 rpm → 750 rpm: VSI drive with speed change is shown in Figure 7.7(a). The system is loaded at 'L_{1i}' mark with reference speed of 750 rpm. The

reference speed of the motor is changed from 750rpm to 850 rpm at 'N_1' mark and then kept constant till the 'N_2' mark. The speed is then brought back to 750 rpm and kept constant till the end. Finally, the system is relieved of the load at the 'L_{1d}' mark. The induction motor speed following the reference speed.

The Figure 7.7(a) shows the system response to changing speeds while the Figure 7.7(b) shows the changes in DC-link voltage and Induction motor line current. The system response characteristics, DC-link voltage change, induction motor line current and induction motor speed responses are summarized in the Table 7.8.

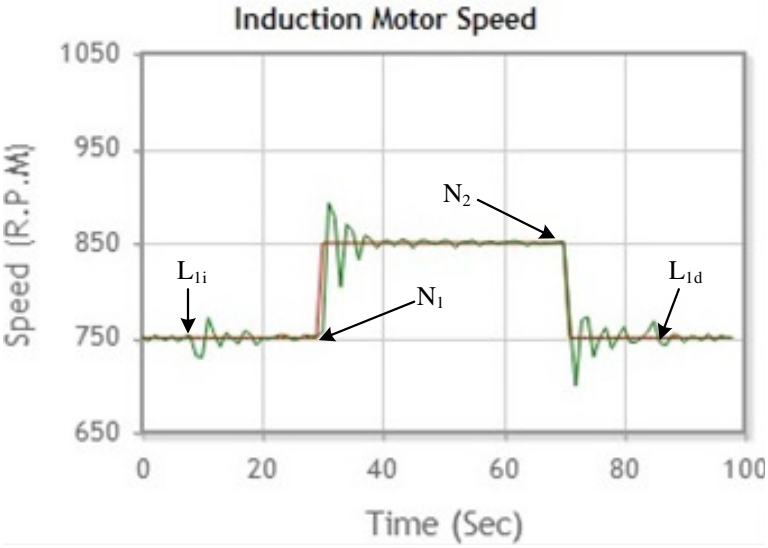

(a) Induction motor rotor speed

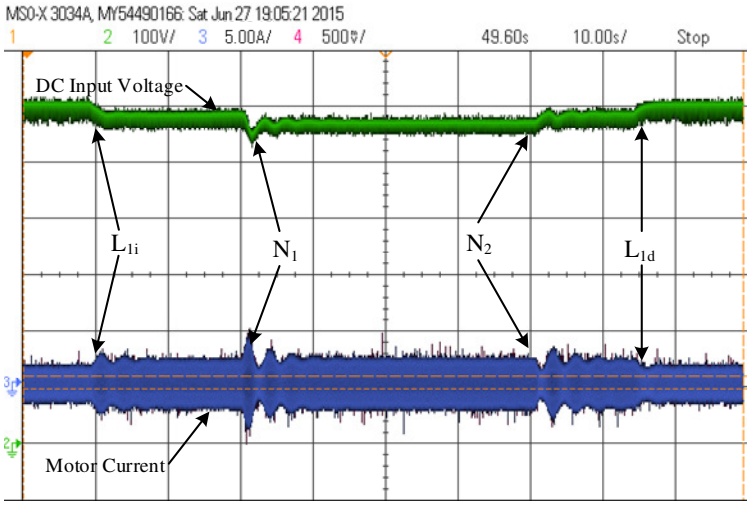

(b) DC-link voltage and induction motor line current

Figure 7.7: VSI Drive with speed change (750-850-750 rpm)

Table 7.8: VSI Drive speed performance with speed change (750-850-750 rpm)

Speed	Current	Peak over/under shoot	V_{DC} drop from 600 V
N_1 = 750-850 rpm	1.9 A	6.3%	567 V
N_2 = 850-750 rpm	1.8 A	7.3 %	580 V

750 rpm→ 950 rpm → 750 rpm: VSI fed drive with speed change is shown in Figure 7.8. Load is applied to the system at 'L_{1i}' mark with speed reference value of 750 rpm. The speed of the motor is increased from reference speed from 750 rpm to 950 rpm at 'N_3' mark and then kept stable till 'N_4' mark. The reference speed is then reverted back to 750 rpm and kept stable till the end. The system is finally unloaded at the 'L_{1d}' mark.

The Figure 7.8(a) shows the system response to changing speeds while the Figure 7.8(b) shows the changes in DC-link voltage and Induction motor line current. The system response characteristics, DC-link voltage change and induction motor speed responses are summarized in Table 7.9.

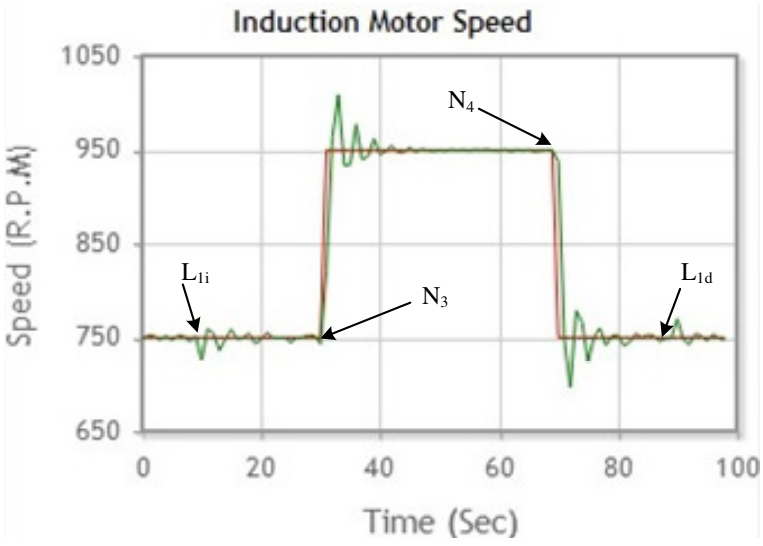

(a) Induction motor rotor speed

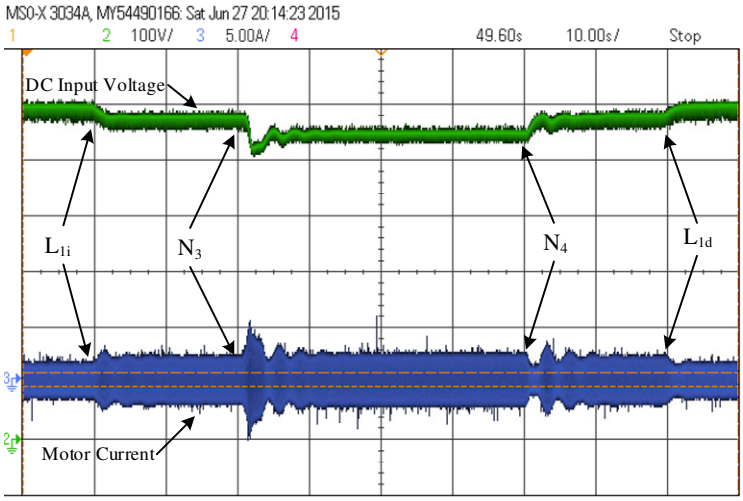

(b) DC-link voltage and induction motor line current

Figure 7.8: VSI Drive with speed change (750-950-750 rpm)

Table 7.9: VSI Drive speed performance with speed change (750-950-750 rpm)

Speed	**Current**	**Peak over/under shoot**	**V_{DC} Drop from 600 V**
N_3 = 750-950 rpm	2 A	4.7 %	540 V
N_4 = 950-750 rpm	1.8 A	6.6 %	580 V

750 rpm → 850 rpm → 950 rpm → 850 rpm → 750 rpm: VSI fed drive with speed change is shown in Figure 7.9. Here we perform the overall increase of the system speed in two steps. The system is loaded at 'L_{1i}' mark with reference speed of 750 rpm. The reference speed of the motor is first changed from 750 rpm to 850 rpm at 20 sec 'N_1' mark and it is maintained for another 20 seconds. Then the speed is again re-raised to 950 rpm at 'N_2' mark and maintained for another 20 seconds. After that the speed is relapsed to 850 rpm at 'N_3' mark. Then it is relapsed to 750 rpm at 'N_4' mark and the system is unloaded at L_{1d}' mark.

The Figure 7.9(a) shows the system response to changing speeds, while the Figure 7.9(b) shows the changes in DC-link voltage and induction motor line current. The system response characteristics, DC-link voltage change and induction motor speed responses are summarized in Table 7.10.

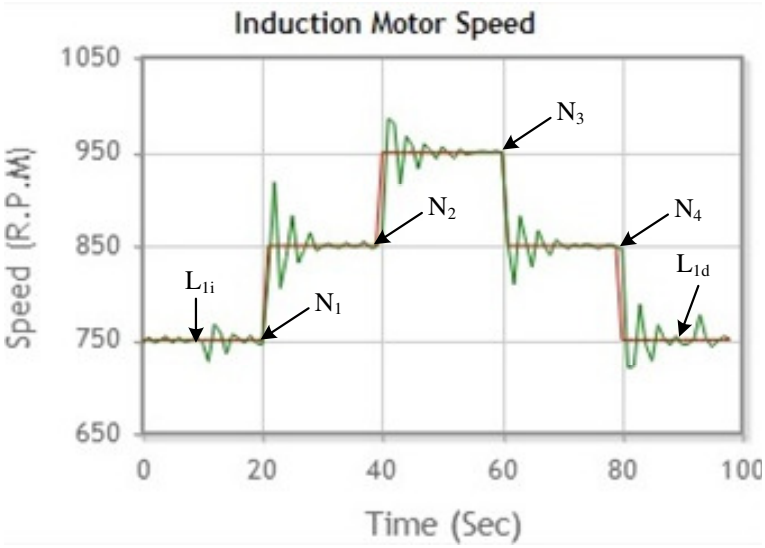

(a) Induction motor rotor speed

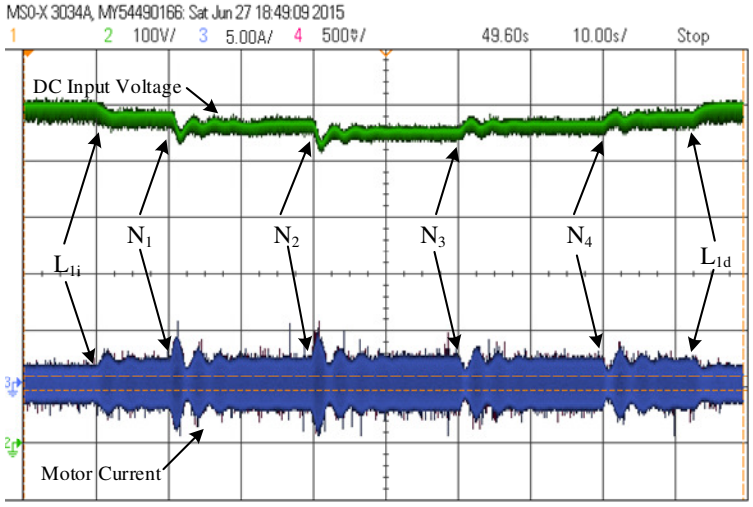

(b) DC-link voltage and induction motor line current

Figure 7.9: VSI Drive with speed change (750-850-950-850750 rpm)

Table 7.10: VSI Drive speed performance with speed change (750-850-950-850-750 rpm)

Speed	**Current**	**Peak over/under shoot**	**V_{DC} drop from 600 V**
N_1 = 750-850 rpm	1.9 A	6.4 %	567 V
N_2 = 850-950 rpm	2 A	3.5 %	547 V
N_3 = 950-850 rpm	1.9 A	4.5 %	567 V
N_4 = 850-750 rpm	1.8 A	4 %	579 V

7.2.2.2 Decreasing Motor Speed: Deceleration of EV

We have studied the effects of an increasing speed change on the system. We will now study the effects of a decreasing speed change on the system. Similar to the increasing case, the system is initially 70% loaded at 10 sec mark and kept for the next 80 seconds. The reference speed of the system is decreased in speed steps back to 750 rpm. The load of the system is then removed at the 90 sec mark.

750 rpm → 650 rpm → 750 rpm: VSI drive with speed change is shown in Figure 7.10. As in the previous case like, the system is loaded at 'L_{1i}' mark with reference speed of 750 rpm. The speed of the motor is changed from reference speed of 750 rpm to 650 rpm at the 30 sec 'N_1' mark and then kept uniform for 30 seconds. At the 60 sec 'N_2' mark, the reference speed is increased back to 750 rpm. Finally, the system is relieved of the load at the 90 sec 'L_{1d}' mark.

The Figure 7.10(a) shows the system response to changing speeds, while the figure 7.10(b) shows the changes in DC-link voltage and Induction motor line current. The system response characteristics, DC-link voltage change and induction motor speed responses are summarized in the Table 7.11.

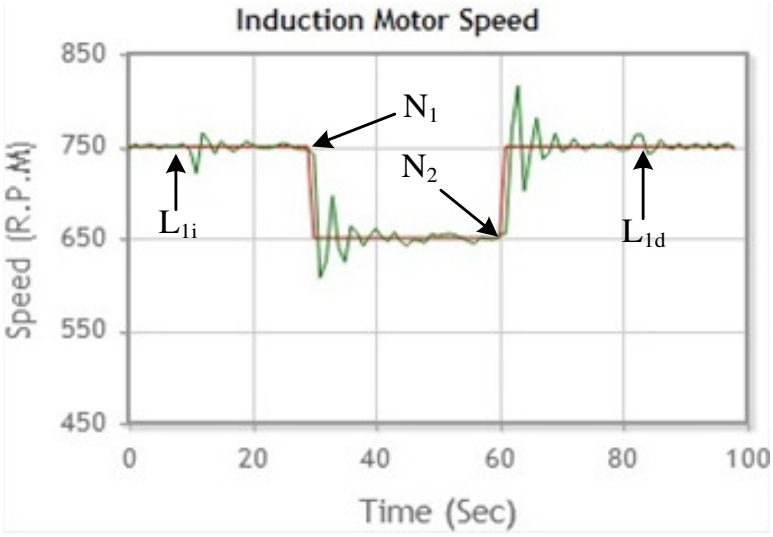

(a) Induction motor rotor speed

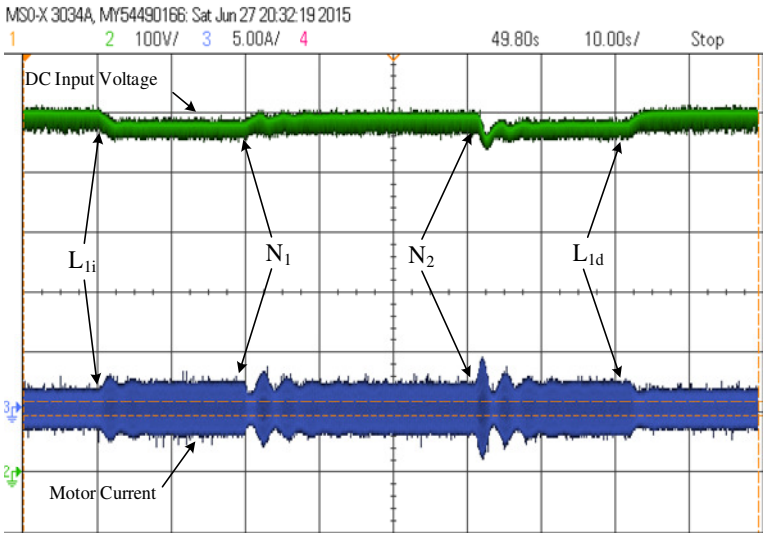

(b) DC-link voltage and induction motor line current

Figure 7.10: VSI Drive with speed change (750-650-750 rpm)

Table 7.11: VSI Drive speed performance with speed change (750-650-750 rpm)

Speed	**Current**	**Peak over/under shoot**	**V_{DC} drop from 600 V**
N_1 = 750-650 rpm	1.7 A	6.1 %	590 sec
N_2 = 650-750 rpm	1.8 A	8.6 %	580 sec

750 rpm→ 550rpm →750 rpm: VSI fed drive with speed change is shown in Figure 7.11. The system is loaded at 'L_{1i}' mark with reference speed of 750 rpm. The referenc speed of the motor is changed from 750 rpm to 550 rpm at 'N_1' mark and then kept constant till 'N_2' mark. The reference speed is then brought back to the 750 rpm and kept constant till the end. Finally, the system is brought to no-load state at 'L_{1d}' mark.

The Figure 7.11(a) shows the system response to changing speeds, while the Figure 7.11(b) shows the changes in DC-link voltage and Induction motor line current. The system response characteristics, DC-link voltage change and induction motor speed responses are summarized in Table 7.12.

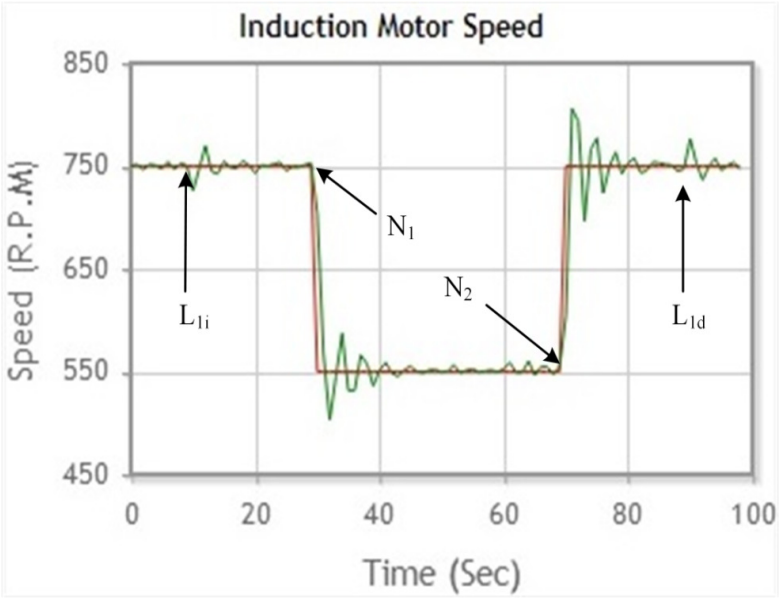

(a) Induction motor rotor speed

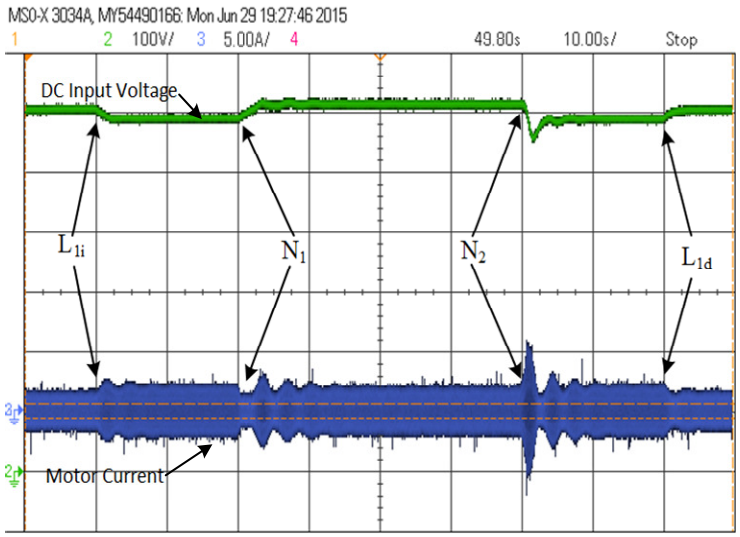

(b) DC-link voltage and induction motor line current

Figure 7.11: VSI Drive with speed change (750-550-750 rpm)

Table 7.12: VSI Drive speed performance with speed change (750-550-750 rpm)

Speed	**Current**	**Peak over/under shoot**	**V_{DC} drop from 600 V**
N_1 = 750-550 rpm	1.55 A	9.0%	595 V
N_2 = 550-750 rpm	1.8 A	7.0%	579 V

750 rpm→ 650 rpm → 550 rpm → 850 rpm →750 rpm: VSI fed drive with speed change is shown in Figure 7.12. The system is loaded at 'L_{1i}' mark with reference speed 750 rpm. The motor reference speed is reduced from 750 rpm to 650 rpm at'N_1' mark, again reduced to 550 rpm at 'N_2'mark. The speed is then relapsed to 650 rpm at'N_3' mark and finally back to 750 rpm at 'N_4' mark. Consequently, the load is removed from the system at the 90 sec (L_{1d}) mark.

The Figure 7.12(a) shows the system response to changing speeds, while the Figure 7.12(b) shows the changes in DC-link voltage and Induction motor line current. The system response characteristics, DC-link voltage change, induction motor line current and induction motor speed responses are summarized in the Table 7.13.

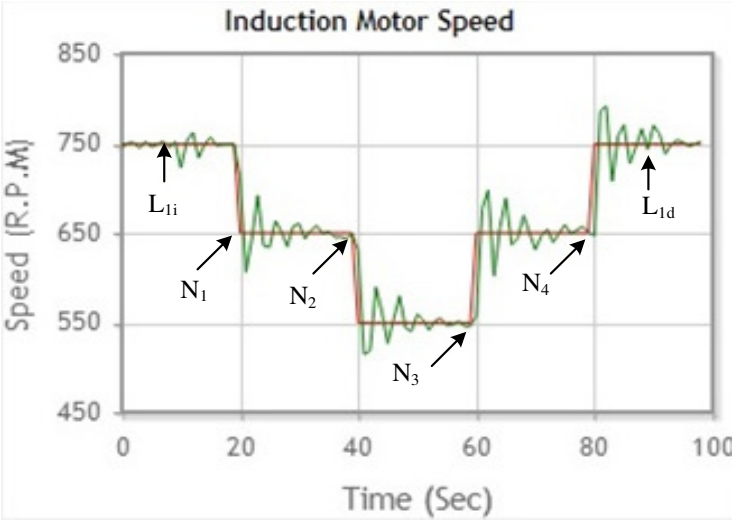

(a) Induction motor rotor speed

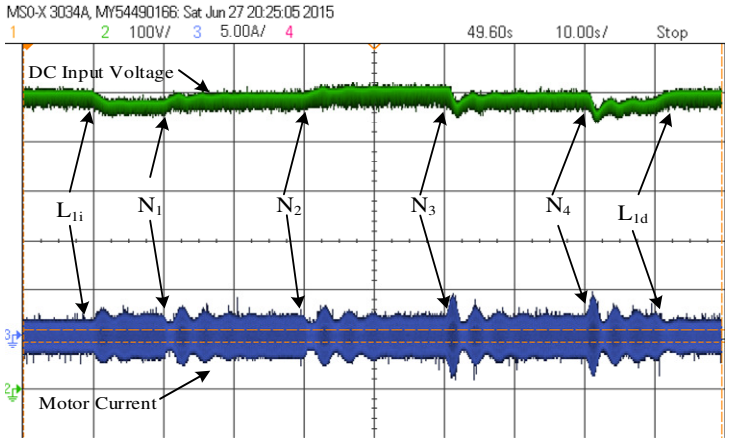

(b) DC-link voltage and induction motor line current

Figure 7.12: VSI Drive with speed change

(750-650-550-650-750 rpm)

Table 7.13: VSI Drive speed performance with speed change (750-650-550-650-750 rpm)

Speed	Current	Peak over/under shoot	V_{DC} drop from 600 V
N_1 = 750-650 rpm	1.12 A	5.8%	590 V
N_2 = 650-550 rpm	0.9 A	6.2 %	595 V
N_3 = 550-650 rpm	1.12 A	6.5 %	598 V
N_4 = 650-750 rpm	1.25 A	5.5 %	590 V

It is to be noted that in each case of simulation and experimentation.The voltage source inverter fed Induction motor drive system was operated using indirect vector control technique. The results obtained in each case contains, the DC-link voltage is changing with speed or load change. The distrabance in the DC-link voltage directly affecting the vsoltage source fed induction motor speed control in all cases. To over come this problem we went the Z source invert fed induction motor drive for electrical vehicle.

7.3 FGS-PI and Zeigler-Nichols-PI Controller Based ZSI Fed Induction Motor Drive

The proposed FGS-PI and classical Zeigler-Nichols-PI controller for the DC-link voltage control are simulated and performances are compared using MATLAB/SIMULINK tool for 5.4 hp induction motor and ZSI parameters are listed in Tables 7.1 and 7.14. The ZSI fed induction motor drive simulation diagram as shown in Figure 7.13.

Table 7.14: ZSI parameters

Parameters	Simulation	Hardware
Input voltage V_{in}	400 V	400 V
DC-link voltage V_{dp}	800 V	600 V
Z Network capacitor $C_1 = C_2$	1000 µF	1000 µF
Z Network inductor $L_1 = L_2$	2.5 mH	3.7 mH
Switching frequency f_s	10000 Hz	10000 Hz

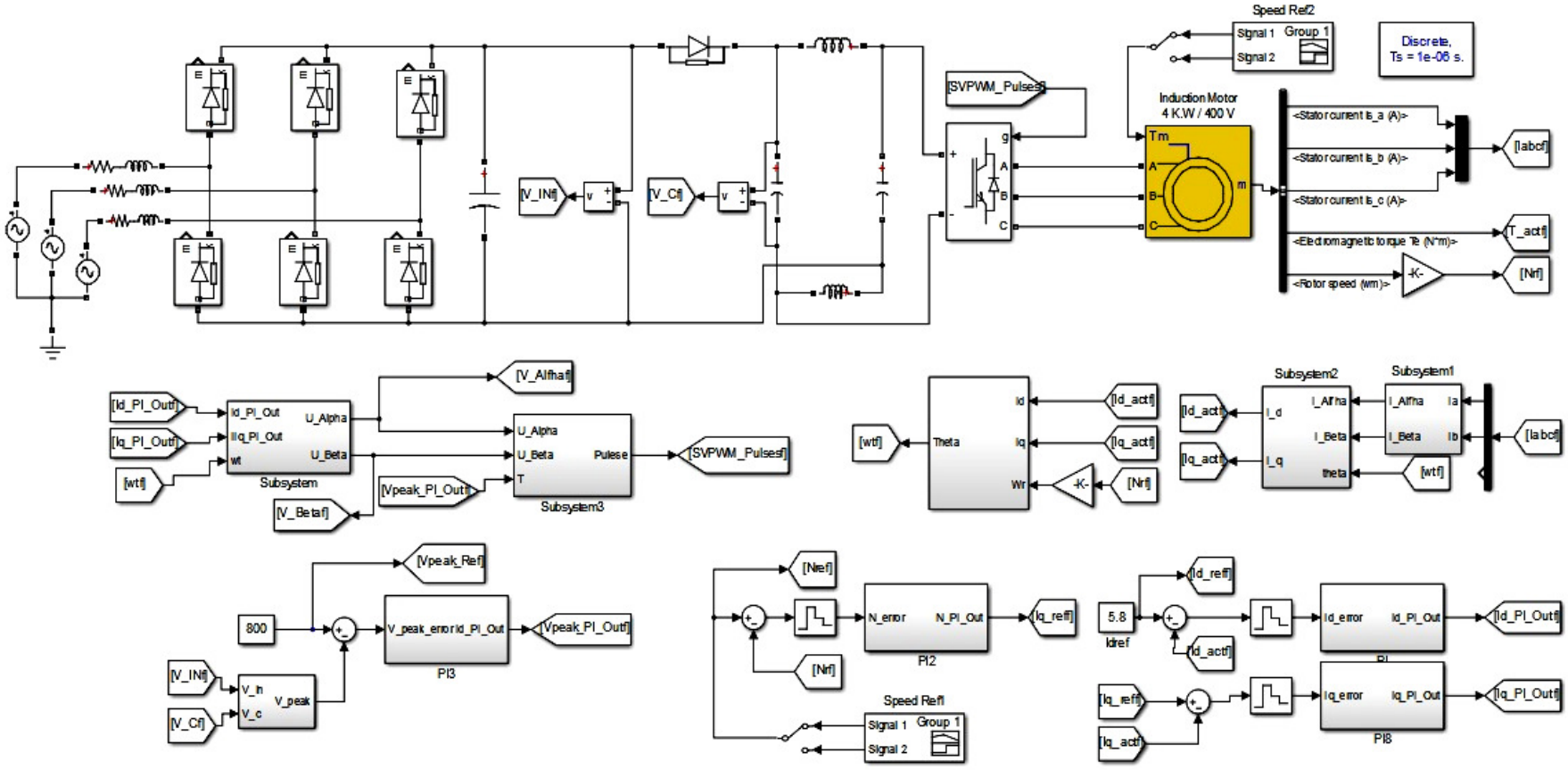

Figure 7.13: Simulation diagram of ZSI fed induction motor drive

The dynamics of DC-link voltage of Z-source fed induction motor drive are governed by the load-torque and rotor-speed changes. The impact of proposed FGS-PI on the dynamics of DC-link voltage has been studied for the following two practical cases i.e.,

1. Change in load-torque with speed constant (hill climbing of electrical vehicle).
2. Change in speed with load (acceleration and deceleration of electrical vehicle).

7.3.1 Change in Load-Torque with Speed Constant: Hill Climbing of EV

The simulation setup has a 400 V DC input which is connected to an inverter through a Z-network. This Z-network helps boost the DC-link voltage from 400 V to 800 V. The same system is now simulated first using a Zeigler-Nichols-PI controller followed by an FGS-PI controller for the case of changing load-torque on the system while maintaining constant rotor speed at reference value of 750 rpm. The system is initially loaded with a torque value of 5 N.m and is then progressively increased to values of 12.5 N.m, 25 N.m and finally 35 N.m. The response of both controllers in following the change in load, in maintaining the rotor speed and DC-link voltage at reference values are noted and illustrated in the Figures 7.14(a), (b) and (c).

The obtained DC-link voltage time response parameters such as peak over shoot, peak under shoot (in percentage), rise time, settling time (in sec) for Ziegler Nichols PI controller (ZN-PI) and fuzzy gain scheduling PI (FGS-PI) controller are presented for comparison in Table 7.15.

Although both controllers show a better speed response at varying loads than a traditional VSI, the FGS-PI clearly has an edge over the Zeigler-Nichols-PI. The speed response indicates a less rise time for the FGS-PI controller when compared with a Zeigler-Nichols-PI controller. The overshoot of the response are also starkly different. The settling time for the FGS-PI is reduced by more than half as compared

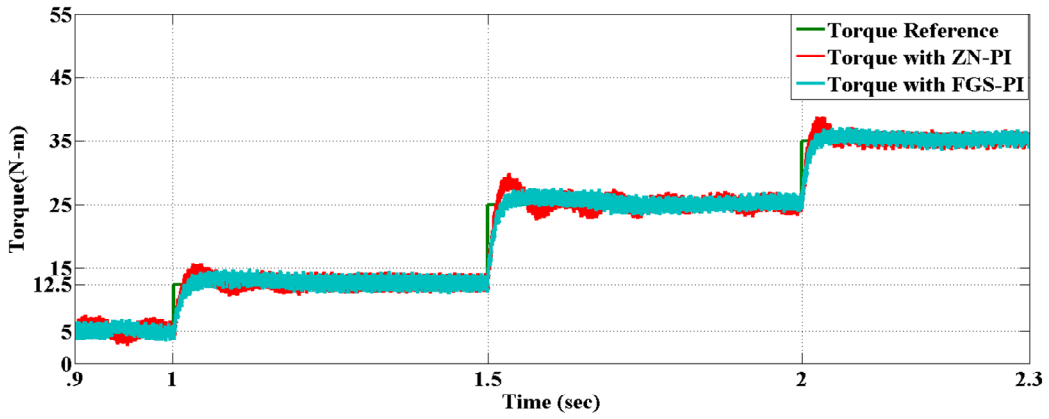

(a) Induction motor shaft torque

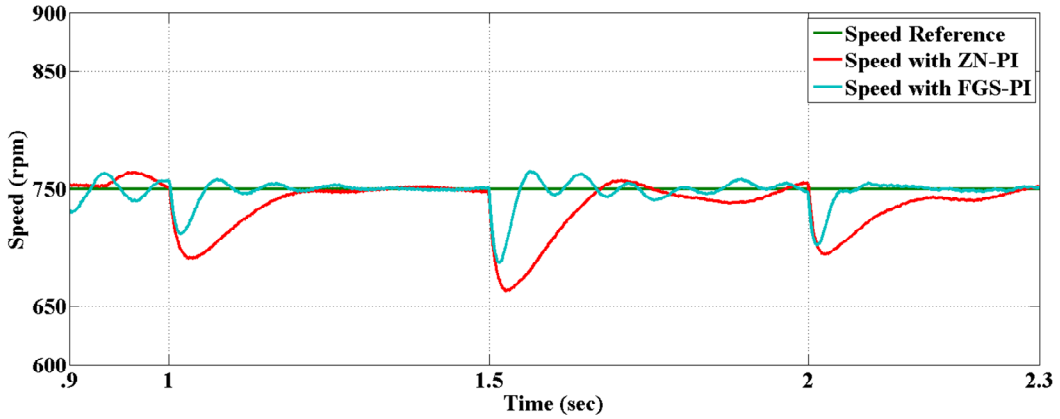

(b) Induction motor rotor speed

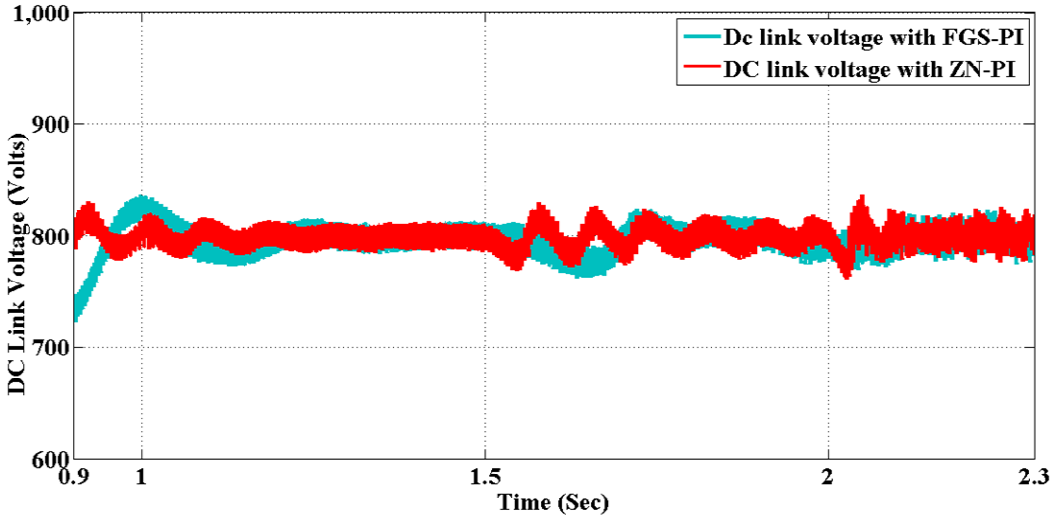

(c) DC-link voltage

Figure 7.14: ZSI Drive with change in load-torque

Table 7.15: DC-link voltage performance indices with torque step change

DC-link performance indices	Torque (5-12.5 N.m)		Torque (12.5-25 N.m)		Torque (25-12.5 N.m)	
	ZN-PI	FGS-PI	ZN-PI	FGS-PI	ZN-PI	FGS-PI
Over shoot	6.5%	4%	7.5%	5%	5.4%	4.1%
Rise time	18 ms	8 ms	20 ms	10 ms	12 ms	25 ms
Settling time	60 ms	30 ms	72 ms	40 ms	50 ms	25 ms

7.3.2 Change in Speed with load: Acceleration and Deceleration of EV

The simulation setup has a 400 V DC input which is connected to an inverter through a Z-network. This Z-network helps boost the DC-link voltage from 400 V to 800 V. The simulation was carried for DC-link voltage of the Z-source inverter fed induction motor system, first using a Zeigler-Nichols PI controller followed by a fuzzy gain scheduling-PI controller under the condition of load-torque of 25 N.m. The reference speed of the motor is then increased from 750 rpm to 1000 rpm. This was followed by another raise to 1400 rpm before bringing the speed back to 1000 rpm and then finally back to 750 rpm. The system's step response of speed, DC-link voltage and load-torque for both the controllers are recorded and showcased in Figure(s) 7.15(a), (b) and (c).

The obtained DC-link voltage time response parameters such as peak over shoot, peak under shoot (in percentage), rise time, settling time(in sec) for Ziegler Nichols PI controller (ZN-PI) and Fuzzy Gain Scheduling PI (FGS-PI) controller are presented for comparison in Table 7.16.

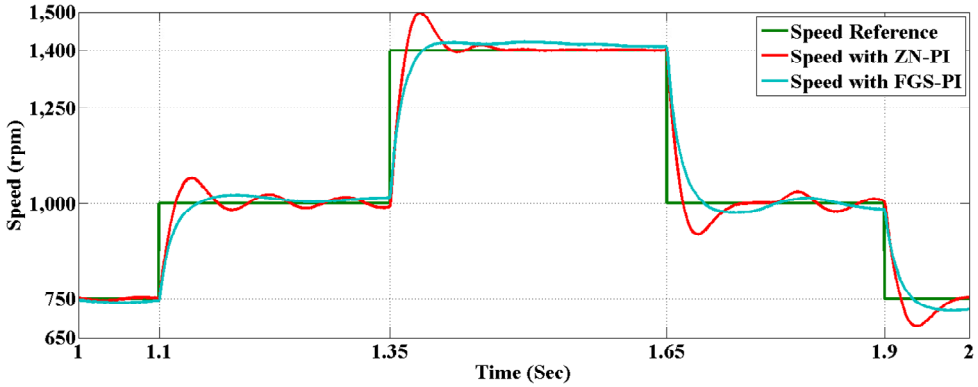

(a) Induction motor rotor speed

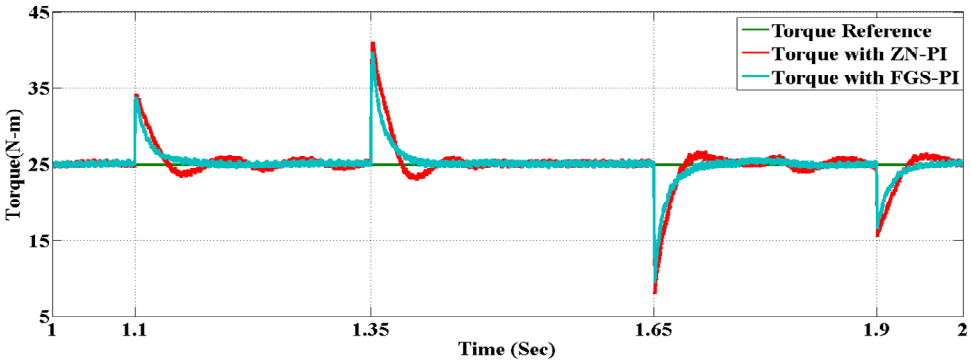

(b) Induction motor shaft torque

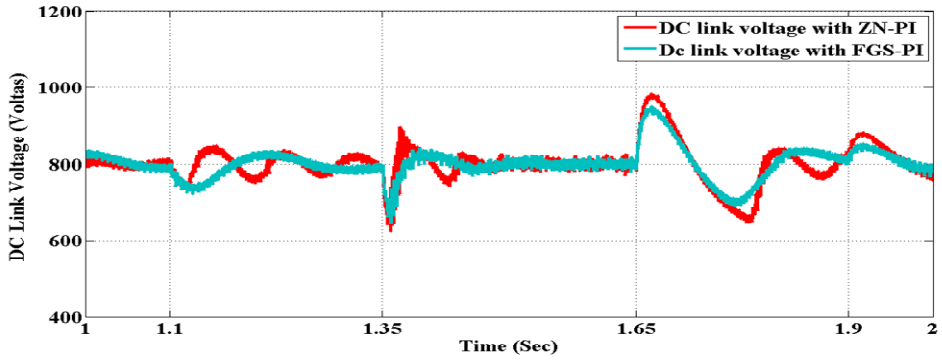

(c) DC-link voltage

Figure 7.15: ZSI Drive with change in speed

Table 7.16: DC-link voltage of performance indices with speed step change

DC-link performance indices	Speed 750-1000 rpm		Speed 1000-1400 rpm		Speed 1400-1000 rpm		Speed 1000-750 rpm	
	ZN-PI	FGS-PI	ZN-PI	FGS-PI	ZN-PI	FGS-PI	ZN-PI	FGS-PI
Under/over shoot	12 %	8 %	15 %	10 %	16.2 %	11.6 %	14.6 %	10.2 %
Rise time	25 ms	15 ms	30 ms	20 ms	20 ms	10 ms	20 ms	10 ms
Setting time	225 ms	110 ms	250 ms	120 ms	500 ms	400 ms	450 ms	300 ms

The DC-link voltage is better maintained in the case of FGS-PI as opposed to Zeigler-Nichols-PI. The overshoots at the instances of speed change are higher for Zeigler-Nichols-PI. There are substantial oscillations in the waveform in the case of Zeigler-Nichols-PI while the response is exceedingly smooth and consistent for FGSPI. All these factors very clearly indicate the superiority of an FGS-PI over the standard Zeigler-Nichols-PI in controlling the induction motor system.

7.4 ZSI Fed Induction Motor Drive: Experimental Setup

A porototype Z-source inverter fed induction motor drive setup Figure 7.16 made in laboratory. The Z-source inverter fed induction motor coupled with DC generator. The speed of the motor was measured with the AC-tacho generator. The speed sensor output is sine-wave and it is converted into pulses using a zero crossing detector circuit. The pulses are fed through the capture module of the DSP for speed sensing. Figures 7.16, 7.17, and 7.18 shows the Z-source inverter, Z-network elements inductor and capacitor, IPM inverter module (BSM50GD120DN2E3226) with (ADUM4332) driver circuit, LEM LV-25 voltage sensor used for input and capacitor voltage sensing, LEM LA-55 current sensor used for induction motor current sensing. The sensed signals are fed to the TMS320F28335 DSP controller for control the DC-link voltage and speed control of induction motor drive. The experimental setup has a 400 V DC input which is connected to an inverter through a Z-network. This Z-network helps boost the DC-link voltage from 400 V to 600 V. The Z-source inverter drives a 3-phase induction motor with coupled to a DC generator. The DC generator is loaded with a bank of resistors. The induction motor parameters and DC generator parameters are given in Table 7.4 and Table 7.5. Since the DC generator carries a load, the induction motor also indirectly sustaining a load.

The aim is to test the ZSI fed drive system under two PI controllers:

1. Zeigler-Nichols (ZN)
2. Fuzzy Gain Scheduling(FGS)

For two dynamical conditions:

1. Load-torque change keeping speed constant (hill climbing and downing emulation of electrical vehicle): There are two phases in this process. First, increase of the load from no-load to overload condition. Second, decrease of the load with time from an existing overloaded condition to no-load condition. We study the system's response in both phases.
2. Speed change with load (acceleration and deceleration emulation of electrical vehicle): The experiment similar to the previous cases where we first load the DC generator with a set of resistors and then test the ZSI drive response to change in the motor speed. Initially, the system is loaded 70% then the speed is changed. The system's response characteristics of peak overshoot/under shoot and changes in input voltage are noted.

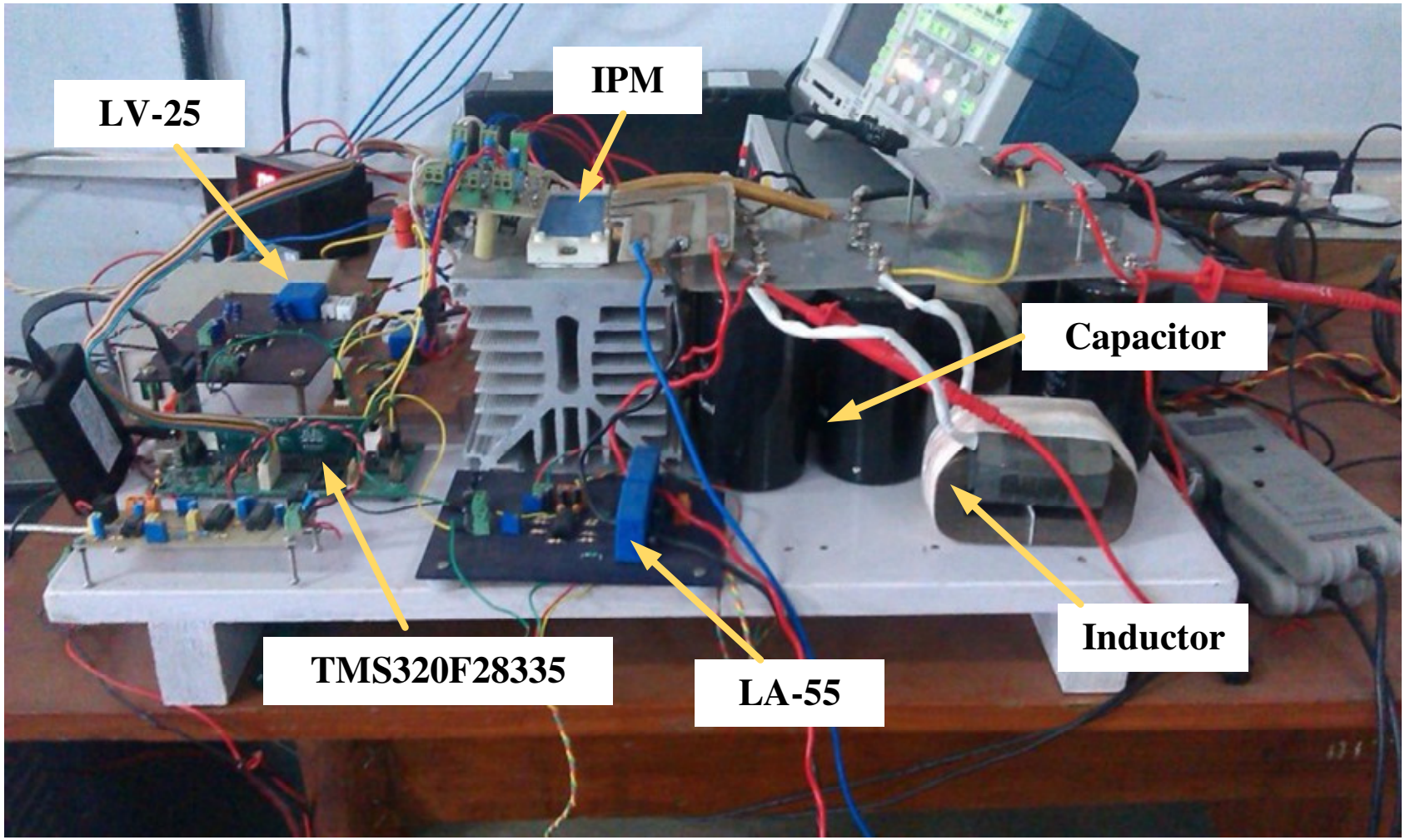

Figure 7.16: Experimental set-up of Z-source fed induction motor drive (a)

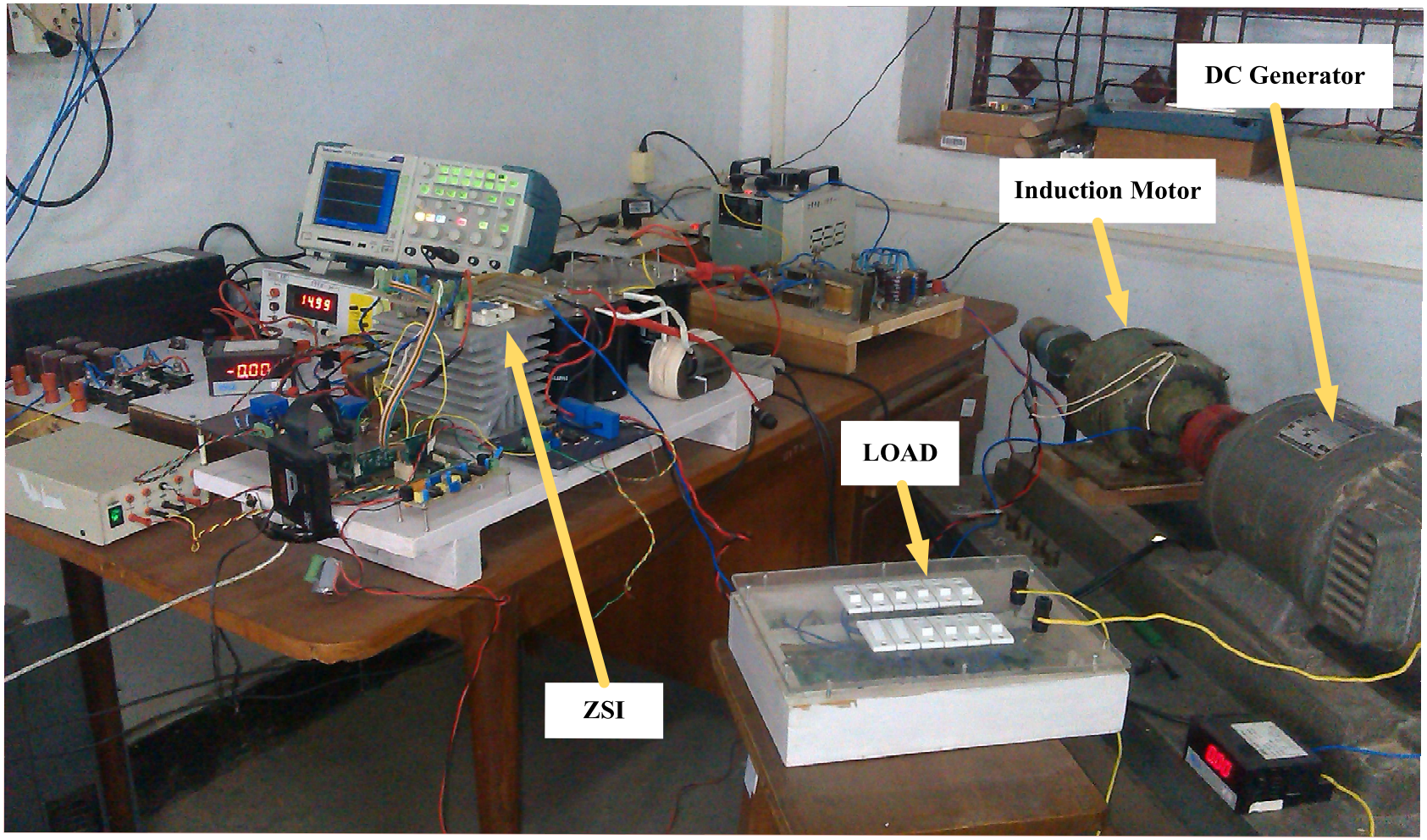

Figure 7.17: Experimental set-up of Z-source fed induction motor drive (b)

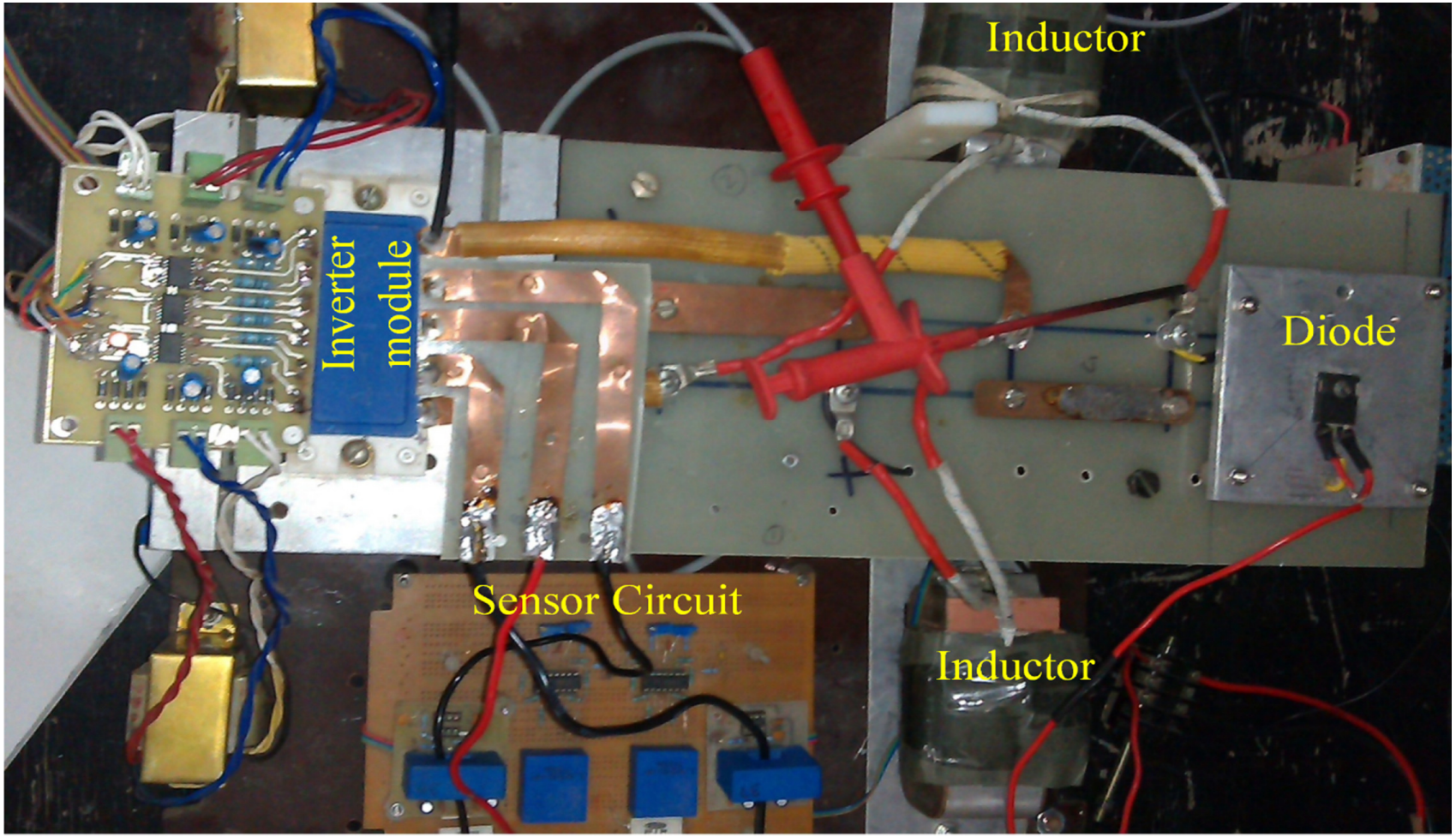

Figure 7.18: Experimental set-up of Z-source fed induction motor drive (c)

7.5 Zeigler-Nichols PI Controller based ZSI Fed Induction Motor Experimental Results

In this case, the DC-link voltage PI controller has been designed using the standard Zeiglar-Nichols control method.

7.5.1 Change in Load-Torque with Speed Constant: Hill Climbing and Downing of EV

Increasing Load Condition: Hill Climbing of EV

The Figure 7.19(a) shows the speed response of the induction motor varying with time. The load applied across the DC generator is increased steadily from no load to overload conditions at instants 20 sec (L_{1i}), 40 sec (L_{2i}), 60 sec (L_{3i}) and 80 sec (L_{4i}).

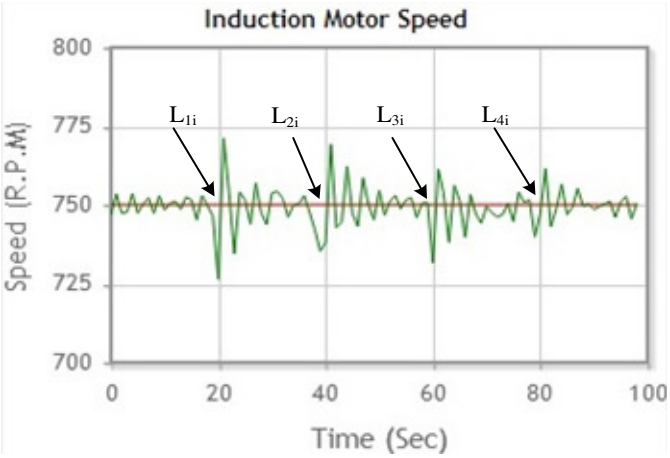

(a) Induction motor rotor speed

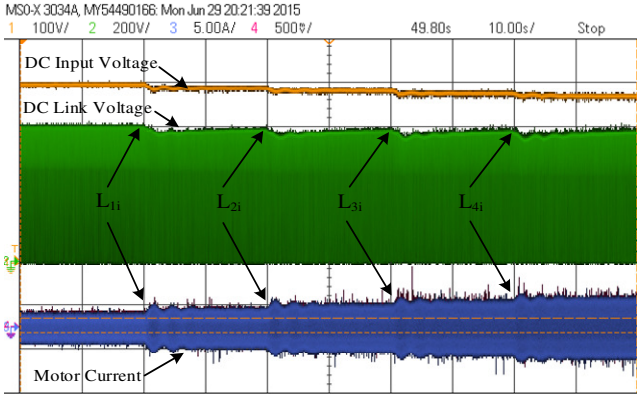

(b) DC-link voltage and induction motor line current

Figure 7.19: Zeigler-Nichols-PI based ZSI drive's performance indices with increasing load

The Figure 7.19(b) shows the DC input voltage, DC-link voltage and induction motor line current of the system from top to bottom respectively. From the Figure 7.19(a), the speed response is better than voltage source inverter fed induction motor. However, the DC-link voltage is not controlled properly. The characteristics of rotor speed, DC-link voltage responses and input DC voltage drop (from 400 V) at each of the loading instants summarized in Table 7.17.

Table 7.17: ZSI with Zeigler-Nichols-PI controller performance indices with increasing load

Load	DC-link voltage undershoot	Induction motor speed overshoot	Input voltage drop from 400 V
L_{1i} = 48%	10.3 %	2.6 %	385 V
L_{2i} = 70%	8.9 %	2.5 %	378 V
L_{3i} = 96%	8.6 %	1.3 %	370 V
L_{4i} = 114%	8.2 %	1.2 %	365 V

Decreasing Load Condition: Hill Downing of EV

The Figure 7.20(a) shows the response of the induction motor to the change in electrical loads at the DC generator end. The DC generator is given an initial 114 % overload and then decreased to no load condition. The drop in load values occur at the times instants of 20 sec (L_{1d}), 40 sec (L_{2d}), 60 sec (L_{3d}) and 80 sec (L_{4d}).

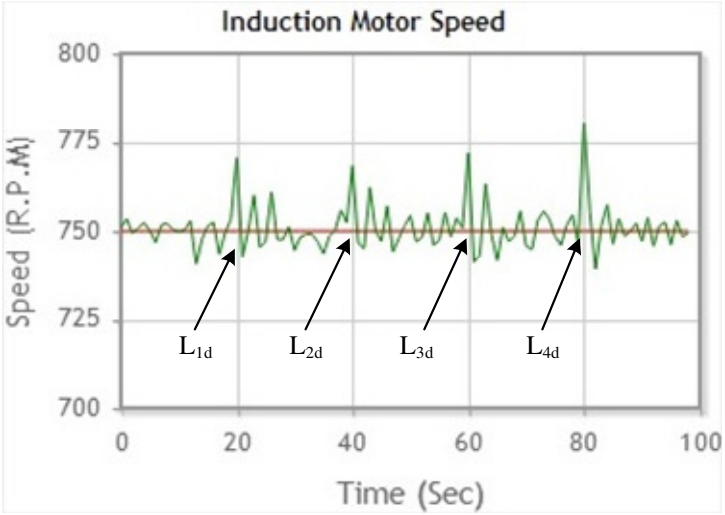

(a) Induction motor rotor speed

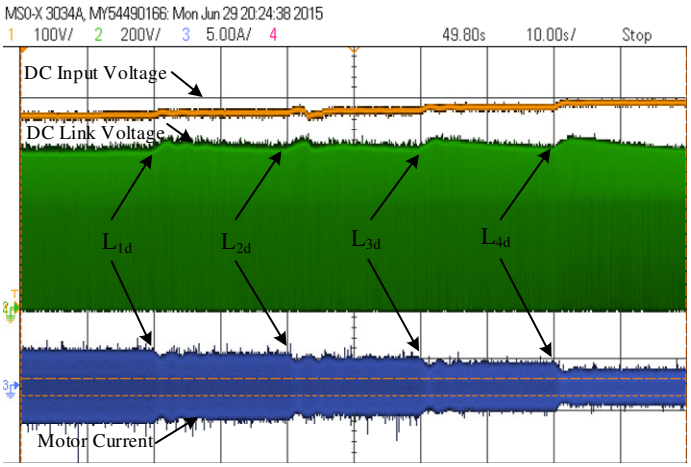

(b) DC-link voltage and induction motor line current

Figure 7.20: Zeigler-Nichols-PI based ZSI drive's performance indices with decreasing load

The Figure 7.20(b) shows the DC input voltage, DC-link voltage and the induction motor line current. The characteristics of rotor speed, DC-link voltage responses and input DC voltage drop (from 400 V) at each of the loading instants summarized in Table 7.18.

Table 7.18: ZSI with Zeigler-Nichols-PI controller performance indices with decreasing load

Load	DC-link voltage overshoot	Induction motor speed overshoot	Input voltage drop from 400 V
L_{1d} = 96 %	8.2 %	2.7 %	370 V
L_{2d} = 70 %	7.9 %	2.8 %	378 V
L_{3d} = 48 %	8.6 %	3.3 %	385 V
L_{4d} = 32 %	9 %	4 %	397 V

7.5.2 Change in Speed with load: Acceleration and Deceleration of EV

The experiment similar to the previous cases where we first load the DC generator with a set of resistors and then test the ZSI drive response to change in the motor speed. Initially, the system is loaded 70% then the speed is changed. The system's response characteristics of peak overshoot/under shoot and changes in input voltage are noted.

750 rpm→ 850 rpm → 950 rpm → 850 rpm → 750 rpm: The overall increase of the system speed is performed in two steps. The ZSI drive is loaded at 10 sec (L_{1i}) with reference speed of 750 rpm. The speed of the motor is first changed from 750 rpm to 850 rpm at the 20 sec (N_1) mark and is held constant for next 20 seconds. Then the speed is re-raised to 950 rpm at 40 sec (N_2) mark and maintained for another 20 seconds. After that the speed is relapsed to 850 rpm at the 60 sec (N_3) mark. Then it is relapsed to the 750 rpm at the 80 sec (N_4) mark and the system is finally unloaded at the 90 sec (L_{1d}) mark.

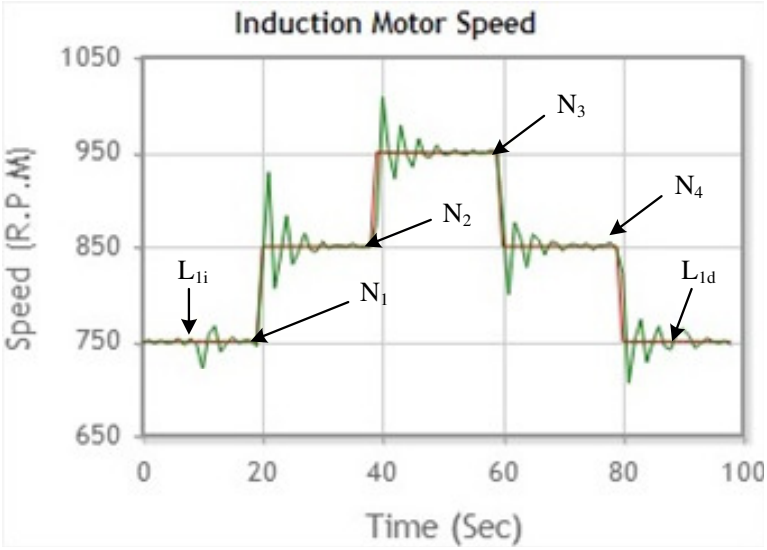

(a) Induction motor rotor speed

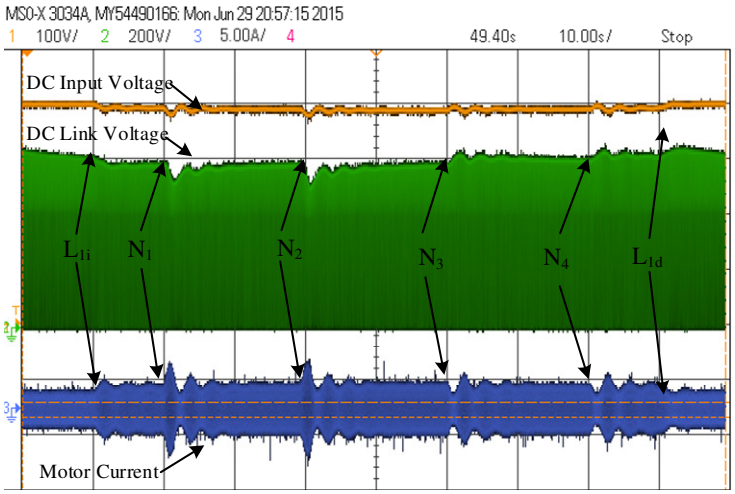

(b) DC-link voltage and induction motor line current

Figure 7.21: Zeigler-Nichols-PI based ZSI drive's performance indices with change in speed (750-850-950-850-750 rpm)

The Figure 7.21(a) shows the ZSI drive speed response at loaded condition. Figure 7.21(b) shows the changes in input DC voltage, DC-link voltage and induction motor line current. The characteristics of rotor speed, DC-link voltage responses and input DC voltage drop (from 400 V) at each of the loading instants summarized in Table 7.19.

Table 7.19: Zeigler-Nichols-PI controller based ZSI drive change in speed

Speed	DC-link voltage over/ under shoot	Induction motor speed over/under shoot	Input voltage drop from 400 V
N_1 = 750-850 rpm	11.5 %	9.4 %	380 V
N_2 = 850-950 rpm	12 %	10%	370 V
N_3 = 950-850 rpm	6 %	5.5 %	380 V
N_4 = 850-750 rpm	8 %	5 %	390 V

7.6 Fuzzy Gain Scheduling PI Controller based ZSI Fed Induction Motor Experimental Results

In this case, we proceed to illustrate the working of a FGS PI controller for ZSI fed Induction motor drive.

7.6.1 Change in Load-Torque with Speed Constant: Hill Climbing and Downing of EV

Increasing Load Condition: Hill Climbing of EV

The Figure 7.22(a) shows the speed response of the induction motor varying with time. The load applied across the DC generator is increased steadily from no load to overload conditions at instants 20 sec (L_{1i}), 40 sec (L_{2i}), 60 sec (L_{3i}) and 80 sec (L_{4i}). The Figure 7.22(b) shows the DC input voltage, DC-link voltage and induction motor line current of the system from top to bottom respectively.

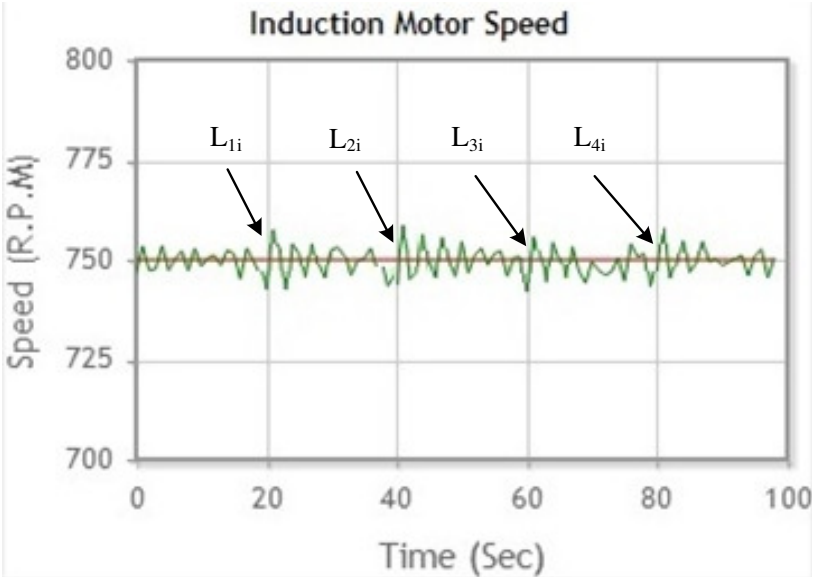

(a) Induction motor rotor speed

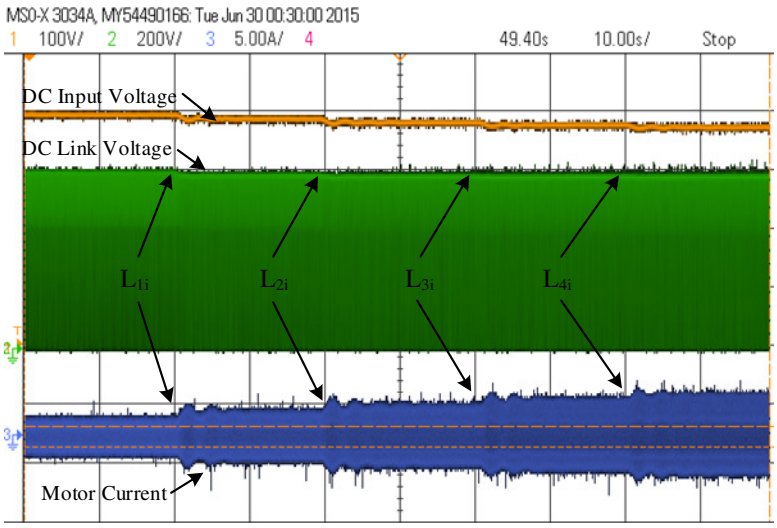

(b) DC-link voltage and induction motor line current

Figure 7.22: FGS-PI based ZSI drive's performance indices with increasing load

From the Figure 7.22(a), the speed response is better than voltage source inverter fed induction motor. However, the DC-link voltage is not controlled properly. The characteristics of rotor speed, DC-link voltage responses and input DC voltage drop (from 400 V) at each of the loading instants summarized in Table 7.20.

Table 7.20: ZSI with fuzzy gain scheduling-PI controller performance indices with increasing load

Load	DC-link voltage undershoot	Induction motor speed overshoot	Input voltage drop from 400 V
L_{1i} = 48 %	1.3 %	0.6 %	385 V
L_{2i} = 70 %	0.9 %	02.5 %	378 V
L_{3i} = 96 %	0.6 %	0.3 %	370 V
L_{4i} = 114 %	0.2 %	0.2 %	365 V

Decreasing Load Condition: Hill Downing of EV

The Figure 7.23(a) shows the response of the induction motor to the change in electrical loads at the DC generator end. The DC generator is given an initial 114 % overload and then decreased to a no load condition. The drop in load values occur at the times instants of 20 sec (L_{1d}), 40 sec (L_{2d}), 60 sec (L_{3d}) and 80 sec (L_{4d}). The Figure 7.23(b) shows the DC input voltage, DC-link voltage and the induction motor line current. The characteristics of rotor speed, DC-link voltage responses and input DC voltage drop (from 400 V) at each of the loading instants summarized in Table 7.21.

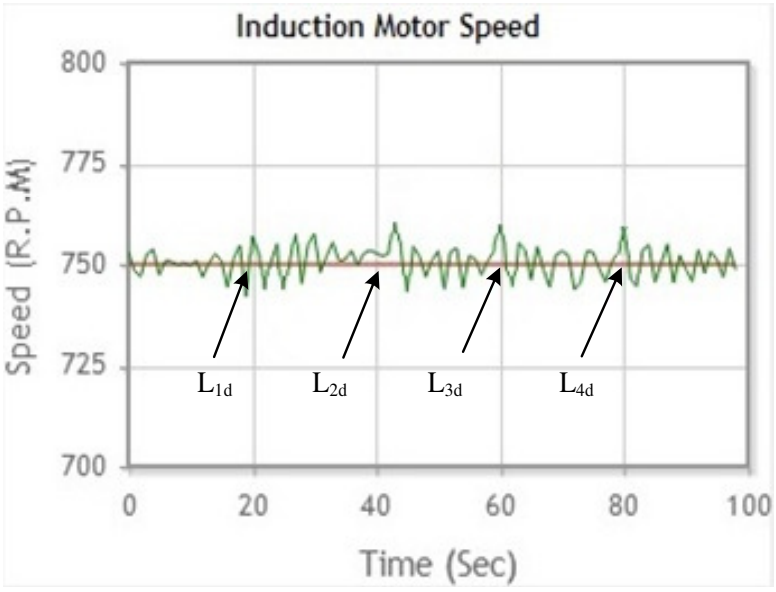

(a) Induction motor rotor speed

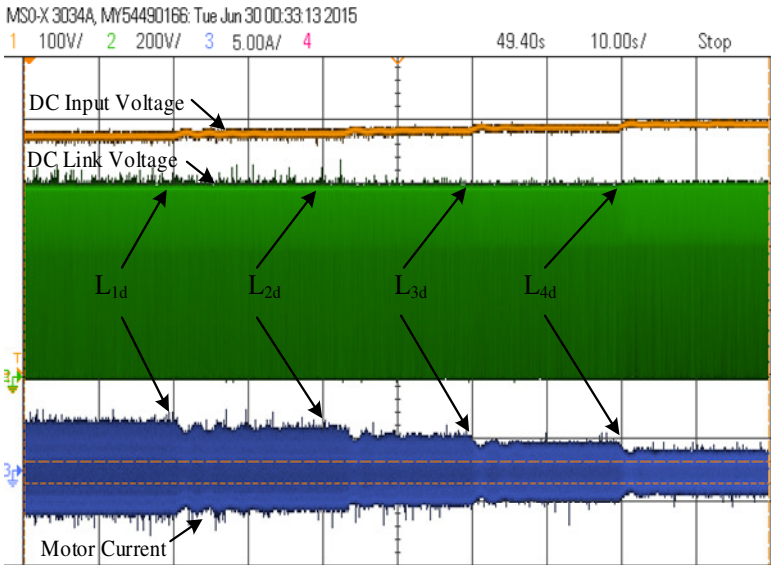

(b) DC-link voltage and induction motor line current

Figure 7.23: FGS-PI based ZSI drive's performance indices with decreasing load

Table 7.21: ZSI with fuzzy gain scheduling-PI controller performance indices with decreasing load

Load	DC-link voltage overshoot	Induction motor speed overshoot	Input voltage drop from 400 V
L_{1d} = 96 %	0.2 %	0.6 %	370 V
L_{2d} = 70 %	0.9 %	0.7 %	378 V
L_{3d} = 48 %	0.6 %	0.4 %	385 V
L_{4d} = 32 %	0.9 %	0.3 %	397 V

7.6.2 Change in Speed with load: Acceleration and Deceleration of EV

The experiment similar to the previous cases where we first load the DC generator with a set of resistors and then test the ZSI drive response to change in the motor speed. Initially, the system is loaded 70% then the speed is changed. The system's response characteristics of peak overshoot/under shoot and changes in input voltage are noted.

750 rpm→ 850 rpm → 950 rpm → 850 rpm → 750 rpm: The overall increase of the system speed is performed in two steps. The ZSI drive is loaded at 10 sec (L_{1i}) with reference speed of 750 rpm. The speed of the motor is first changed from

750 rpm to 850 rpm at the 20 sec (N_1) mark and is held constant for next 20 seconds. Then the speed is re-raised to 950 rpm at 40 sec (N_2) mark and maintained for another 20 seconds. After that the speed is relapsed to 850 rpm at the 60 sec (N_3) mark. Then it is relapsed to the 750 rpm at the 80 sec (N_4) mark and the system is finally unloaded at the 90 sec (L_{1d}) mark.

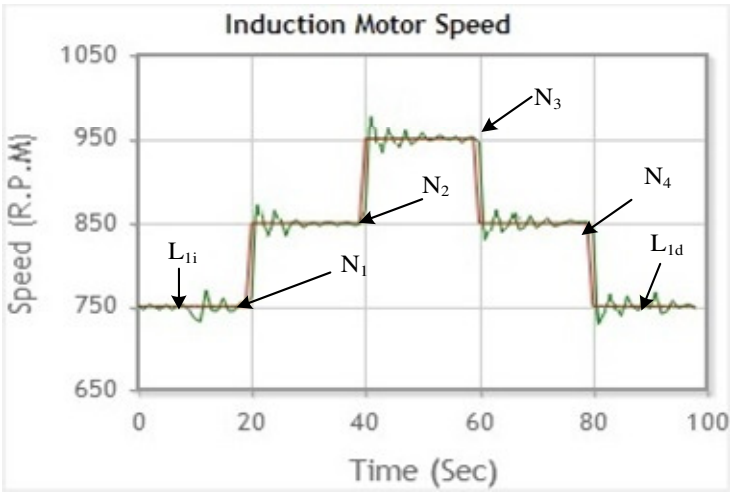

(a) Induction motor rotor speed

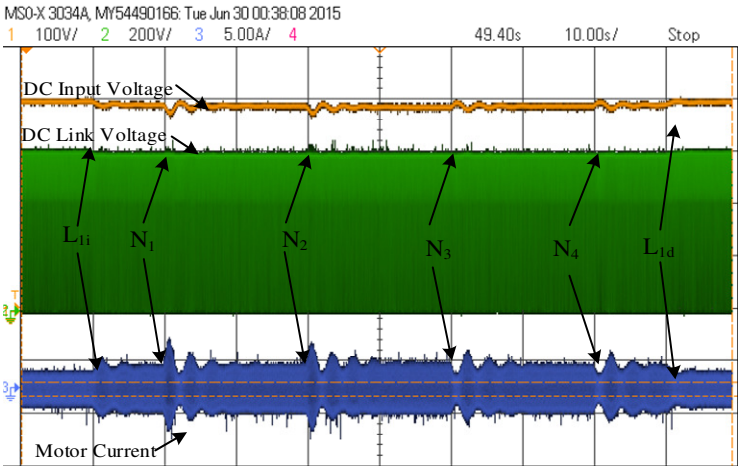

(b) DC-link voltage and induction motor line current

Figure 7.24: FGS-PI based ZSI drive's performance indices with change in speed (750-850-950-850-750 rpm)

The Figure 7.24(a) shows the ZSI drive speed response at loaded condition. Figure 7.24(b) shows the changes in input DC voltage, DC-link voltage and induction motor line current. The characteristics of rotor speed, DC-link voltage responses and

input DC voltage drop (from 400 V) at each of the loading instants summarized in Table 7.22.

Table 7.22: FGS-PI based ZSI drive change in speed

Speed	DC-link voltage over/ under shoot	Induction motor speed over/under shoot	Input voltage drop from 400 V
N_1 = 750-850 rpm	1.5 %	1 %	380 V
N_2 = 850-950 rpm	1.2 %	1.2%	370 V
N_3 = 950-850 rpm	0.6 %	0.9 %	380 V
N_4 = 850-750 rpm	0.8 %	0.8 %	390 V

In all cases, it can be observed that the peak overshoot, rise-time and settling time of DC-link voltage have decreased in the ZSI drive based on FGS-PI controller compared to that of ZN-PI controller, along with this drive speed performance also improved.

Table 7.23: Converter's efficiency

Load	VSI efficiency	ZSI efficiency
52 %	55.18 %	79.20 %
66 %	66.18 %	85.25 %
73%	72.93 %	91.95 %
82 %	82.9 %	94.30 %
97 %	85.6 %	96.10%
118%	82.3 %	94.20 %

Table 7.23 shows the efficiency at different loading conditions and all loading conditions the ZSI drive efficiency is more the VSI drive.

7.7 Summary

The Z-source inverter fed induction motor drive was subjected to various dynamical conditions. The results obtained for Zeigler-Nichols and fuzzy gain scheduling PI controllers were compared and the over all drive's performance is analyzed implemented.

Chapter - 8

Conclusions and Future Scope

This thesis presents design and development of hybrid controller for controlling the peak DC-link voltage of Z-source inverter (ZSI) fed induction motor drive in electrical vehicle. Modelling and simulation for performance analysis of the ZSI drive under various operating conditions was carried out using different controllers in MATLAB environment using simulink and power system block set toolboxes. Implementation of the Z-source inverter drive consists of developing and testing of the prototype drive to validate the effectiveness of the proposed control algorithm. Relevant conclusions pertaining to the various aspects of the investigation has been reported at the end of respective chapters. This chapter is an overall summary of the investigations in various chapters.

The main objective of the thesis was presenting efficient control algorithm and its implementation. The peak DC-link voltage control by non-linear control technique using fuzzy gain scheduled-proportional integral (FGS-PI) controller showed better control in the situation of the input voltage drops under various operating condition of electrical vehicle. The proposed algorithm succeeds in DC-link voltage boosting to desired level by sensing the input and capacitor terminal voltages. The simulation of the proposed control algorithm was done for various practical operating conditions of the drive, which were validated by implementing in real time on prototype laboratory setup. The investigations were carried out for Z-source inverter fed induction motor drive with (i) speed change with load (acceleration and deceleration), (ii) change in load-torque at constant speed (hill climbing and downing). During these conditions the input voltage got drop, it is observed FGS-PI controller provides a better peak DC-link voltage boost for the same shoot-through duty ratio and modulation index. The modulation index and shoot-through are regulated continuously to track the reference peak DC-link voltage. The proposed FGS-PI controller technique has better stability than traditional Zeigler-Nichols Proportional Integral (ZN-PI) controller and it has verified by both simulation and hardware.

The Z-source inverter fed induction motor drive has implemented using motion control dedicated digital signal processor TMS320F28335 has resulted in reduction of the system hardware to great extent. The processor also enables to monitor the software signals in real time frame during the drive control using GUI composer in digital signal processor.

Recommendations for Future Works

The following research work is suggested for the Z-source inverter fed induction motor drive as a continuation of this research.

- In this research the experimental verifications were carried out using the simplified Z-source inverter. The Quasi Z-source inverter (QZSI) can be implemented by replacing the Z-network of the system.
- In this research work, grid supply with a front end diode rectifier is taken to supply DC voltage to the Z-source inverter, A solar system or fuel cell system can be used as the input source and effectiveness of the proposed FGS-PI controller method can be verify.
- The dynamic control model of the Z-source inverter can be implementing in FPGA.
- The adaptive PI controller can be implemented to control the DC-link voltage of Z-source inverter.
- The optimizing methods can be used for tuning the PI controller.

References

[1] B. A. Welchko, T. A. Lipo, T. M. Jahns, and S. E. Schulz, "Fault tolerant three-phase AC motor drive topologies: A comparison of features, cost, and limitations," *IEEE Trans. Power Electron.*, vol. 19, no. 4, pp. 1108–1116, 2004.

[2] A. Sikorski and T. Citko, "Current controller reduced switching frequency for VS-PWM inverter used with AC motor drive applications," *IEEE Trans. Ind. Electron.*, vol. 45, no. 5, pp. 792–801, 1998.

[3] O. Luca, C. Carretero, J. M. Burdio, J. Acero, and F. Almazan, "Multiple-output resonant matrix converter for multiple induction heaters," *IEEE Trans. Ind. Appl.*, vol. 48, no. 4, pp. 1387–1396, 2012.

[4] N. Vazquez, C. Aguilar, J. Arau, R. O. Caceres, I. Barbi, and J. a. Gallegos, "A novel uninterruptible power supply system with active power factor correction," *IEEE Trans. Power Electron.*, vol. 17, no. 3, pp. 405–412, 2002.

[5] C. R. Kay Soon Low, "Model Predictive Control of Parallel-Connected Inverters for Uninterruptible Power Supplies," *IEEE Trans. Ind. Electron.*, vol. 55, no. 8, pp. 2884–2893, 2008.

[6] M. Arias Perez de Azpeitia, A. Fernandez, D. G. Lamar, M. Rodrnguez, and M. M. Hernando, "Simplified voltage-sag filler for line-interactive uninterruptible power supplies," *IEEE Trans. Ind. Electron.*, vol. 55, no. 8, pp. 3005–3011, 2008.

[7] A. Nasiri, "Digital Control of Three-Phase Series-Parallel Uninterruptible Power Supply Systems," *IEEE Trans. Power Electron.*, vol. 22, no. 4, pp. 1116–1127, 2007.

[8] N. Y. Dai, M. C. Wong, and Y. D. Han, "Application of a three-level NPC inverter as a three-phase four-wire power quality compensator by generalized 3DSVM," *IEEE Trans. Power Electron.*, vol. 21, no. 2, pp. 440–449, 2006.

[9] Man-Chung Wong, Zheng-Yi Zhao, Ying-Duo Han, and Liang-Bing Zhao, "Three-dimensional pulse-width modulation technique in three-level power inverters for three-phase four-wired system," *IEEE Trans. Power Electron.*, vol. 16, no. 3, pp. 418–427, 2001.

[10] T. B. Lazzarin and I. Barbi, “DSP-Based Control for Parallelism of Three-Phase Voltage Source Inverter,” *IEEE Trans. Ind. Informatics*, vol. 9, no. 2, pp. 749–759, 2013.

[11] A. Kahrobaeian and Y. A. R. I. Mohamed, “Interactive distributed generation interface for flexible micro-grid operation in smart distribution systems,” *IEEE Trans. Sustain. Energy*, vol. 3, no. 2, pp. 295–305, 2012.

[12] P. Rodriguez, A. V. Timbus, R. Teodorescu, M. Liserre, and F. Blaabjerg, “Flexible Active Power Control of Distributed Power Generation Systems During Grid Faults,” *IEEE Trans. Ind. Electron.*, vol. 54, no. 5, pp. 2583–2592, 2007.

[13] M. I. Marei, E. F. El-Saadany, and M. M. A. Salama, “A flexible DG interface based on a new RLS algorithm for power quality improvement,” *IEEE Syst. J.*, vol. 6, no. 1, pp. 68–75, 2012.

[14] M. I. Marei, E. F. El-Saadany, and M. M. A. Salama, “A novel control algorithm for the DG interface to mitigate power quality problems,” *IEEE Trans. Power Deliv.*, vol. 19, no. 3, pp. 1384–1392, 2004.

[15] P. H. Nguyen, W. L. Kling, and P. F. Ribeiro, “Smart power router: A flexible agent-based converter interface in active distribution networks,” *IEEE Trans. Smart Grid*, vol. 2, no. 3, pp. 487–495, 2011.

[16] F. Wang, J. L. Duarte, and M. A. M. Hendrix, “Pliant active and reactive power control for grid-interactive converters under unbalanced voltage dips,” *IEEE Trans. Power Electron.*, vol. 26, no. 5, pp. 1511–1521, 2011.

[17] J. De Santiago, H. Bernhoff, B. Ekergard, S. Eriksson, S. Ferhatovic, R. Waters, and M. Leijon, “Electrical motor drivelines in commercial all-electric vehicles: A review,” *IEEE Trans. Veh. Technol.*, vol. 61, no. 2, pp. 475–484, 2012.

[18] W. Li, J. Cao, and X. Zhang, “Electrothermal analysis of induction motor with compound cage rotor used for PHEV,” *IEEE Trans. Ind. Electron.*, vol. 57, no. 2, pp. 660–668, 2010.

[19] A. Emadi and K. Rajashekara, “Power Electronics and Motor Drives in Electric, Hybrid Electric, and Plug-In Hybrid Electric Vehicles,” *IEEE Trans. Ind. Electron.*, vol. 55, no. 6, pp. 2237–2245, 2008.

[20] K. W. E. Cheng, B. P. Divakar, H. Wu, K. Ding, and H. F. Ho, "Battery-management system (BMS) and SOC development for electrical vehicles," *IEEE Trans. Veh. Technol.*, vol. 60, no. 1, pp. 76–88, 2011.

[21] K. Clement-Nyns, E. Haesen, and J. Driesen, "The impact of Charging plug-in hybrid electric vehicles on a residential distribution grid," *IEEE Trans. Power Syst.*, vol. 25, no. 1, pp. 371–380, 2010.

[22] D. Hirschmann, D. Tissen, S. Schröder, R. W. De Doncker, and R. W. De Doncker, "Reliability Prediction for Inverters in Hybrid Electrical Vehicles," *IEEE Trans. Power Electron.*, vol. 22, no. 6, pp. 2511–2517, 2007.

[23] O. Vodyakho and C. C. Mi, "Three-Level Inverter-Based Shunt Active Power Filter in Three-Phase Three-Wire and Four-Wire Systems," *IEEE Trans. Power Electron.*, vol. 24, no. 5, pp. 1350–1363, 2008.

[24] W. C. Lee, T. K. Lee, and D. S. Hyun, "A three-phase parallel active power filter operating with PCC voltage compensation with consideration for an unbalanced load," *IEEE Trans. Power Electron.*, vol. 17, no. 5, pp. 807–814, 2002.

[25] J. B. Ekanayake and N. Jenkins, "Three-level advanced static VAr compensator," *IEEE Trans. Power Deliv.*, vol. 11, no. 1, pp. 540–545, 1996.

[26] C. J. Hatziadoniu and F. E. Chalkiadakis, "A transformerless high-pulse static synchronous compensator based on the 3-level GTO-inverter," *IEEE Trans. Power Deliv.*, vol. 13, no. 3, pp. 883–888, 1998.

[27] F. Z. Peng, "Z-source inverter," *IEEE Trans. Ind. Appl.*, vol. 39, no. 2, pp. 504–510, 2003.

[28] T. Sukegawa, K. Kamiyama, K. Mizuno, T. Matsui, and T. Okuyama, "Fully digital, vector-controlled PWM VSI-fed AC drives with an inverter dead-time compensation strategy," *IEEE Trans. Ind. Appl.*, vol. 27, no. 3, pp. 552–559, 1991.

[29] S. A. S. Grogan, D. G. Holmes, and B. P. McGrath, "High performance voltage regulation of current source inverters," *IEEE Trans. Power Electron.*, vol. 26, no. 9, pp. 2439–2448, 2010.

[30] S. Kwak and T. Kim, "An integrated current source inverter with reactive and harmonic power compensators," *IEEE Trans. Power Electron.*, vol. 24, no. 2, pp. 348–357, 2009.

[31] M. Takei, Y. Harada, and K. Ueno, "600 V-IGBT with reverse blocking capability," in *Proc. 13th IEEE Conf. Power Semiconductor Devices & ICs. IPSD '01*, 2001, pp. 413–416.

[32] F. Z. Peng, M. Shen, and Z. Qian, "Maximum boost control of the Z-source inverter," *IEEE Trans. Power Electron.*, vol. 20, no. 4, pp. 833–838, 2005.

[33] M. Shen, J. Wang, A. Joseph, F. Z. Peng, L. M. Tolbert, and D. J. Adams, "Constant boost control of the Z-source inverter to minimize current ripple and voltage stress," *IEEE Trans. Ind. Appl.*, vol. 42, no. 3, pp. 770–778, 2006.

[34] P. C. Loh, D. M. Vilathgamuwa, Y. Sen Lai, G. T. Chua, and Y. Li, "Pulse-width modulation of Z-source inverters," *IEEE Trans. Power Electron.*, vol. 20, no. 6, pp. 1346–1355, 2005.

[35] P. C. Loh, D. M. Vilathgamuwa, C. J. Gajanayake, Y. R. Lim, and C. W. Teo, "Transient Modeling and Analysis of Pulse-Width Modulated Z-Source Inverter," *IEEE Trans. Power Electron.*, vol. 22, no. 2, pp. 498–507, 2007.

[36] F. Z. Peng, A. Joseph, J. Wang, M. Shen, L. Chen, Z. Pan, E. Ortiz-Rivera, and Y. Huang, "Z-source inverter for motor drives," *IEEE Trans. Power Electron.*, vol. 20, no. 4, pp. 857–863, 2005.

[37] F. Z. Peng, X. Yuan, X. Fang, and Z. Qian, "Z-source inverter for adjustable speed drives," *IEEE Power Electron. Lett.*, vol. 99, no. 2, pp. 33–35, 2003.

[38] P. C. Loh, F. Gao, and F. Blaabjerg, "Topological and modulation design of three-level Z-source inverters," *IEEE Trans. Power Electron.*, vol. 23, no. 5, pp. 2268–2277, 2008.

[39] X. Fang, X. Yuan, and H. Zhou, "Current Mode Z-Source Inverter-Fed ASD System," in *Proc. EEE Conf. Power Electronics Specialists Conference. PESC 04*, 2004, pp. 2805–2809.

[40] P. C. Loh, F. Gao, F. Blaabjerg, S. Y. C. Feng, and K. N. J. Soon, "Pulsewidth-Modulated Z-Source Neutral-Point-Clamped Inverter," *IEEE Trans. Ind. Appl.*, vol. 43, no. 5, pp. 1295–1308, 2007.

[41] Y. Huang, M. Shen, F. Z. Peng, and J. Wang, "Z-Source Inverter for Residential Photovoltaic Systems," *IEEE Trans. Power Electron.*, vol. 21, no. 6, pp. 1776–1782, 2006.

[42] C. J. Gajanayake, D. M. Vilathgamuwa, and P. C. Loh, "Development of a comprehensive model and a multiloop controller for Z-source inverter DG systems," *IEEE Trans. Ind. Electron.*, vol. 54, no. 4, pp. 2352–2359, 2007.

[43] Q. V Tran, T. W. Chun, J. R. Ahn, and H. H. Lee, "Algorithms for controlling both the dc boost and ac output voltage of Z-source inverter," *IEEE Trans. Ind. Electron.*, vol. 54, no. 5, pp. 2745–2750, 2007.

[44] J. Liu, J. Hu, and L. Xu, "Dynamic Modeling and Analysis of Z Source Converter-Derivation of AC Small Signal Model and Design-Oriented Analysis," *IEEE Trans. Power Electron.*, vol. 22, no. 5, pp. 1786–1796, 2007.

[45] X. Ding, Z. Qian, S. Yang, B. Cui, and F. Peng, "A PID Control Strategy for DC-link Boost Voltage in Z-source Inverter," in *Proc. Twenty Second Annual IEEE Conf. Applied Power Electronics Conference. APEC 2007*, 2007, pp. 1145–1148.

[46] Y. Liu, H. Abu-Rub, F. Z. Peng, and B. Ge, "Modelling and controller design of quasi-Z-source inverter with battery-based photovoltaic power system," *IET Power Electron.*, vol. 7, no. 7, pp. 1665–1674, 2014.

[47] S. Yang, X. Ding, F. Zhang, F. Z. Peng, and Z. Qian, "Unified control technique for Z-Source inverter," in *Proc. IEEE Conf. Power Electronics Specialists Conference. PESC 08*, 2008, pp. 3236–3242.

[48] M. Shen and F. Z. Peng, "Operation modes and characteristics of the Z-source inverter with small inductance or low power factor," *IEEE Trans. Ind. Electron.*, vol. 55, no. 1, pp. 89–96, 2008.

[49] Y. Tang, S. Xie, C. Zhang, and Z. Xu, "Improved Z-source inverter with reduced Z-source capacitor voltage stress and soft-start capability," *IEEE Trans. Power Electron.*, vol. 24, no. 2, pp. 409–415, 2009.

[50] S. Rajakaruna and L. Jayawickrama, "Steady-state analysis and designing impedance network of Z-source inverters," *IEEE Trans. Ind. Electron.*, vol. 57, no. 7, pp. 2483–2491, 2010.

[51] S. Ashok and V. Vijayan, "High-performance bi-directional Z-source inverter for locomotive drive application," *IET Electr. Syst. Transp.*, vol. 5, no. 4, pp. 166–174, 2015.

[52] F. Z. Peng, M. Shen, and K. Holland, "Application of Z-source inverter for traction drive of fuel cell-battery hybrid electric vehicles," *IEEE Trans. Power Electron.*, vol. 22, no. 3, pp. 1054–1061, 2007.

[53] O. Ellabban, J. Van Mierlo, and P. Lataire, "A DSP-based dual-loop peak dc-link voltage control strategy of the Z-source inverter," *IEEE Trans. Power Electron.*, vol. 27, no. 9, pp. 4088–4097, 2012.

[54] M. H. J. Bollen and L. D. Zhang, "Analysis of voltage tolerance of AC adjustable-speed drives for three-phase balanced and unbalanced sags," in *Proc. IEEE Conf. Industrial & Commercial Power Systems Technical Conference*, 1999, vol. 6, pp. 904–910.

[55] A. Von Jouanne, P. N. Enjeti, and B. Banerjee, "Assessment of ride-through alternatives for adjustable-speed drives," *IEEE Trans. Ind. Appl.*, vol. 35, no. 4, pp. 908–916, 1999.

[56] F. F. Wang, S. Member, G. Chen, D. Boroyevich, S. Ragon, M. Arpilliere, and V. R. Stefanovic, "Analysis and Design Optimization of Diode Front-End Rectifier Passive Components for Voltage Source Inverters," *IEEE Trans. Power Electron.*, vol. 23, no. 5, pp. 2278–2289, 2008.

[57] R. O. Caceres and I. Barbi, "A boost DC-AC converter: Analysis, design, and experimentation," *IEEE Trans. Power Electron.*, vol. 14, no. 1, pp. 134–141, 1999.

[58] L. Bor-Ren, "Analysis and implementation of a three-level pwm rectifier/inverter," *IEEE Trans. Aerosp. Electron. Syst.*, vol. 36, no. 3 PART 1, pp. 948–956, 2000.

[59] Y. P. Siwakoti, F. Z. Peng, F. Blaabjerg, P. C. Loh, and G. E. Town, "Impedance-Source Networks for Electric Power Conversion Part I: A Topological Review," *IEEE Trans. Power Electron.*, vol. 30, no. 2, pp. 699–716, 2015.

[60] M. E. H. Benbouzid and N. S. Nait Said, "An Efficiency-Optimization Controller for Induction Motor Drives," *IEEE Power Eng. Rev.*, vol. 18, no. 5, pp. 63–64, 1998.

[61] F. Zidani, M. E. H. Benbouzid, and D. Diallo, "Fuzzy efficient-optimization controller for induction motor drives," *IEEE Power Eng. Rev.*, vol. 20, no. 10, pp. 43–44, 2000.

[62] H.-D. Lee and S.-K. Sul, "Fuzzy-Logic-Based Torque Control Strategy for Parallel-Type Hybrid Electric Vehicle," *IEEE Trans. Ind. Electron.*, vol. 45, no. 4, pp. 625–632, 1998.

[63] Y. A. R. I. Mohamed, "Direct Instantaneous Torque Control in Direct Drive Permanent Magnet Synchronous Motors - a New Approach," *IEEE Trans. Energy Convers.*, vol. 22, no. 4, pp. 829–838, 2007.

[64] M. G. Jovanovic and R. E. Betz, "The use of doubly fed reluctance machines for large pumps and wind turbines," *IEEE Trans. Ind. Appl.*, vol. 38, no. 6, pp. 1508–1516, 2002.

[65] M. Zeraoulia, M. E. H. Benbouzid, and D. Diallo, "Electric Motor Drive Selection Issues for HEV Propulsion Systems: A Comparative Study," *IEEE Trans. Veh. Technol.*, vol. 55, no. 6, pp. 1756–1764, 2006.

[66] E. P. Wiechmann, P. Aqueveque, R. Burgos, and J. Rodriguez, "On the efficiency of voltage source and current source inverters for high-power drives," *IEEE Trans. Ind. Electron.*, vol. 55, no. 4, pp. 1771–1782, 2008.

[67] R. Ramchand, K. Sivakumar, a. Das, C. Patel, and K. Gopakumar, "Improved switching frequency variation control of hysteresis controlled voltage source inverter-fed IM drives using current error space vector," *IET Power Electron.*, vol. 3, no. 2, p. 219, 2010.

[68] P. C. Loh, D. M. Vilathgamuwa, C. J. Gajanayake, L. T. Wong, and C. P. Ang, "Z-source current-type inverters: Digital modulation and logic implementation," *IEEE Trans. Power Electron.*, vol. 22, no. 1, pp. 169–177, 2007.

[69] D. C. Franklin and A. Morelato, "Improving dynamic aggregation of induction motor models," *IEEE Trans. Power Syst.*, vol. 9, no. 4, pp. 1934–1941, 1994.

[70] R. W. De Doncker and D. W. Novotny, "The universal field oriented controller," *IEEE Trans. Ind. Appl.*, vol. 30, no. 1, pp. 92–100, 1994.

[71] A. Ba-Razzouk, A. Cheriti, G. Olivier, P. Sicard, A. Cheriti, G. Olivier, and P. Sicard, "Field-oriented control of induction motors using neural-network decouplers," *IEEE Trans. Power Electron.*, vol. 12, no. 4, pp. 752–763, 1997.

[72] N. Teske, G. M. Asher, M. Sumner, and K. J. Bradley, "Suppression of saturation saliency effects for the sensorless position control of induction motor drives under loaded conditions," *IEEE Trans. Ind. Electron.*, vol. 47, no. 5, pp. 1142–1150, 2000.

[73] Y. Tang and S. Xie, "System design of series Z-source inverter with feedforward and space vector pulse-width modulation control strategy," *IET Power Electron.*, vol. 7, no. 3, pp. 736–744, 2014.

[74] A. K. Akkarapaka and D. Singh, "An IFOC-DSVPWM Based DC-Link Voltage Compensation of Z-Source Inverter Fed Induction Motor Drive for EVs," *Hindawi Adv. Power Electron.*, vol. 2015, pp. 1–14, 2015.

[75] A. K. Akkarapaka and D. Singh, "Digital Implementation of DSVPWM Control for EV fed through Impedance Source Inverter," *Int. J. Power Electron. Drive Syst.*, vol. 6, no. 3, 2015.

[76] K. Hatua and V. T. Ranganathan, "A Novel VSI- and CSI-Fed Dual Stator Induction Motor Drive Topology for Medium-Voltage Drive Applications," *IEEE Trans. Ind. Electron.*, vol. 58, no. 8, pp. 3373–3382, 2011.

[77] Y. P. Siwakoti, F. Z. Peng, F. Blaabjerg, P. C. Loh, G. E. Town, and S. Yang, "Impedance-Source Networks for Electric Power Conversion Part II: Review of Control and Modulation Techniques," *IEEE Transactions on Power Electronics*, vol. 30, no. 4, pp. 1887–1906, 2015.

[78] F. Guo, L. Fu, C.H. Lin, C. Li, W. Choi, and J. Wang, "Development of an 85-kW Bidirectional Quasi-Z-Source Inverter With DC-Link Feed-Forward Compensation for Electric Vehicle Applications," *IEEE Trans. Power Electron.*, vol. 28, no. 12, pp. 5477–5488, 2013.

[79] J. Jung, V. Q. Leu, T. D. Do, E. Kim, and H. H. Choi, "Adaptive PID Speed Control Design for Permanent Magnet Synchronous Motor Drives," *IEEE Trans. Power Electron.*, vol. 30, no. 2, pp. 900–908, 2015.

[80] S. Skoczowski, S. Domek, K. Pietrusewicz, and B. Broel-Plater, "A method for improving the robustness of PID control," *IEEE Trans. Ind. Electron.*, vol. 52, no. 6, pp. 1669–1676, 2005.

[81] K. H. Ang, G. Chong, and Y. Li, "PID control system analysis, design, and technology," *IEEE Trans. Control Syst. Technol.*, vol. 13, no. 4, pp. 559–576, 2005.

[82] A. Ferrante and L. Ntogramatzidis, "Exact tuning of PID controllers in control feedback design," *IET Control Theory Appl.*, vol. 5, no. 4, pp. 565–578, 2011.

[83] J. J. E. Oviedo, T. Boelen, and P. Van Overschee, "Robust Advanced PID Control (RaPID) PID Tuning Based on Engineering Specifications," *Ieee Control Syst. Mag.*, no. February, pp. 15–19, 2006.

[84] G. J. Silva, A. Datta, and S. P. Bhattacharyya, "On the Stability and Controller Robustness of Some Popular PID Tuning Rules," *IEEE Trans. Automat. Contr.*, vol. 48, no. 9, pp. 1638–1641, 2003.

[85] E. Poulin and A. Pomerleau, "PID tuning for integrating and unstable processes," in *Proc. IEEE Conf. Control Theory and Applications*, 1996, vol. 143, pp. 429–435.

[86] J. Xu, Z.Q. Guo, and T. H. Lee, "Design and Implementation of a Takagi Sugeno-Type Fuzzy Logic Controller on a Two-Wheeled Mobile Robot," *IEEE Trans. Ind. Electron.*, vol. 60, no. 12, pp. 5717–5728, 2013.

[87] A. Rubaai, D. Ricketts, and M. D. Kankam, "Laboratory implementation of a microprocessor-based fuzzy logic tracking controller for motion controls and drives," *IEEE Trans. Ind. Appl.*, vol. 38, no. 2, pp. 448–456, 2002.

[88] S.C. Wang and Y.H. Liu, "A Modified PI-Like Fuzzy Logic Controller for Switched Reluctance Motor Drives," *IEEE Trans. Ind. Electron.*, vol. 58, no. 5, pp. 1812–1825, 2011.

[89] A. G. Perry, G. F. G. Feng, Y.F. L. Y.F. Liu, and P. C. Sen, "A Design Method for PI-like Fuzzy Logic Controllers for DC-DC Converter," *IEEE Trans. Ind. Electron.*, vol. 54, no. 5, pp. 2688–2696, 2007.

[90] A. R. Ofoli and A. Rubaai, "Real-Time Implementation of a Fuzzy Logic Controller for Switch-Mode Power-Stage DC-DC Converters," *IEEE Trans. Ind. Appl.*, vol. 42, no. 6, pp. 1367–1374, 2006.

[91] M. Singh, P. Kumar, and I. Kar, "Implementation of vehicle to grid infrastructure using fuzzy logic controller," *IEEE Trans. Smart Grid*, vol. 3, no. 1, pp. 565–577, 2012.

[92] M. Tomizuka and S. Isaka, “Fuzzy gain scheduling of PID controllers,” *IEEE Trans. Syst. Man. Cybern.*, vol. 23, no. 5, pp. 1392–1398, 1993.

[93] Y. Kanthaphayao and V. Chunkag, “Current-sharing bus and fuzzy gain scheduling of proportional-integral controller to control a parallel-connected AC/DC converter,” *IET Power Electron.*, vol. 7, no. 10, pp. 2525–2532, 2014.

[94] F. U. Syed, M. L. Kuang, M. Smith, S. Okubo, and H. Ying, “Fuzzy gain-scheduling proportional-integral control for improving engine power and speed behavior in a hybrid electric vehicle,” *IEEE Trans. Veh. Technol.*, vol. 58, no. 1, pp. 69–84, 2009.

[95] T. Screenuch, A. Tsourdos, E. Hughes, and B. White, “Fuzzy gain-scheduled missile autopilot design using evolutionary algorithms,” *IEEE Trans. Aerosp. Electron. Syst.*, vol. 42, no. 4, pp. 1323–1339, 2006.

[96] V. Vlatkovic and D. Borojevic, “Digital-signal-processor-based control of three-phase space vector modulated converters,” *Ind. Electron. IEEE Trans.*, vol. 41, no. 3, pp. 326–332, 1994.

[97] M. Suetake, I. N. Da Silva, and A. Goedtel, “Embedded DSP-based compact fuzzy system and its application for induction-motor V/f speed control,” *IEEE Trans. Ind. Electron.*, vol. 58, no. 3, pp. 750–760, 2011.

[98] R. J. Wai and L. J. Chang, “Decoupling and tracking control of induction motor drive,” *IEEE Trans. Aerosp. Electron. Syst.*, vol. 38, no. 4, pp. 1357–1369, 2002.

[99] M. M. Morcos and A. Lakshmikanth, “DSP-based solutions for AC motor drives,” *IEEE Power Eng. Rev.*, vol. 19, no. 9, pp. 57–59, 1999.

[100] E. Cerruto, A. Consoli, S. Member, A. Raciti, and A. Testa, “Fuzzy Adaptive Vector Control of Induction Motor Drives,” *IEEE Trans. Power Electron.*, vol. 12, no. 6, pp. 1028–1040, 1997.

[101] S. A. Zaid, O. A. Mahgoub, and K. A. El-Metwally, “Implementation of a new fast direct torque control algorithm for induction motor drives,” *IET Electr. Power Appl.*, vol. 4, no. 5, p. 305, 2010.

Appendix-A

Tacho-Generator

An electro-mechanical generator is a device capable of producing electrical power from mechanical energy. A generator specially designed and constructed for this use is called a tachometer or tachogenerator. The tachogenerator is connected to the motor through a mechanical coupling. The output of tachogenerator is a sinusoidal wave. The Figure B.1 (circuit) converts sinusoidal waves from tachogenerator into pulses which are given to DSP.

From the The Figure B.1, in the first OP-AMP, the sinusoidal wave is given and the voltage supplied is +3 *V* and -3 *V*. This circuit basically coverts the sine wave into a pulse of 3 *V* magnitude and same time period as of the input sine wave. But DSP doesn't accept negative values. So our pulse wave has to be shifted up. The wave is supplied to the inverting terminal of OP-AMP via a resistor in feedback. The noninverting terminal is connected to ground. The output of this configuration is 180 degrees phase shifted pulse wave with the magnitude $\frac{R_f}{R_{IN}}$ which is half the value. This wave is given to another OP-AMP inverting terminal via resistance as feedback. 1.5 *V* is applied as non-inverting terminal. This gives a 180 degrees phase shifted and 1.5 *V* positive offset pulse wave. This output wave contains glitches. To eliminate them, it is fed to a schmitt trigger where the output settles at constant values.

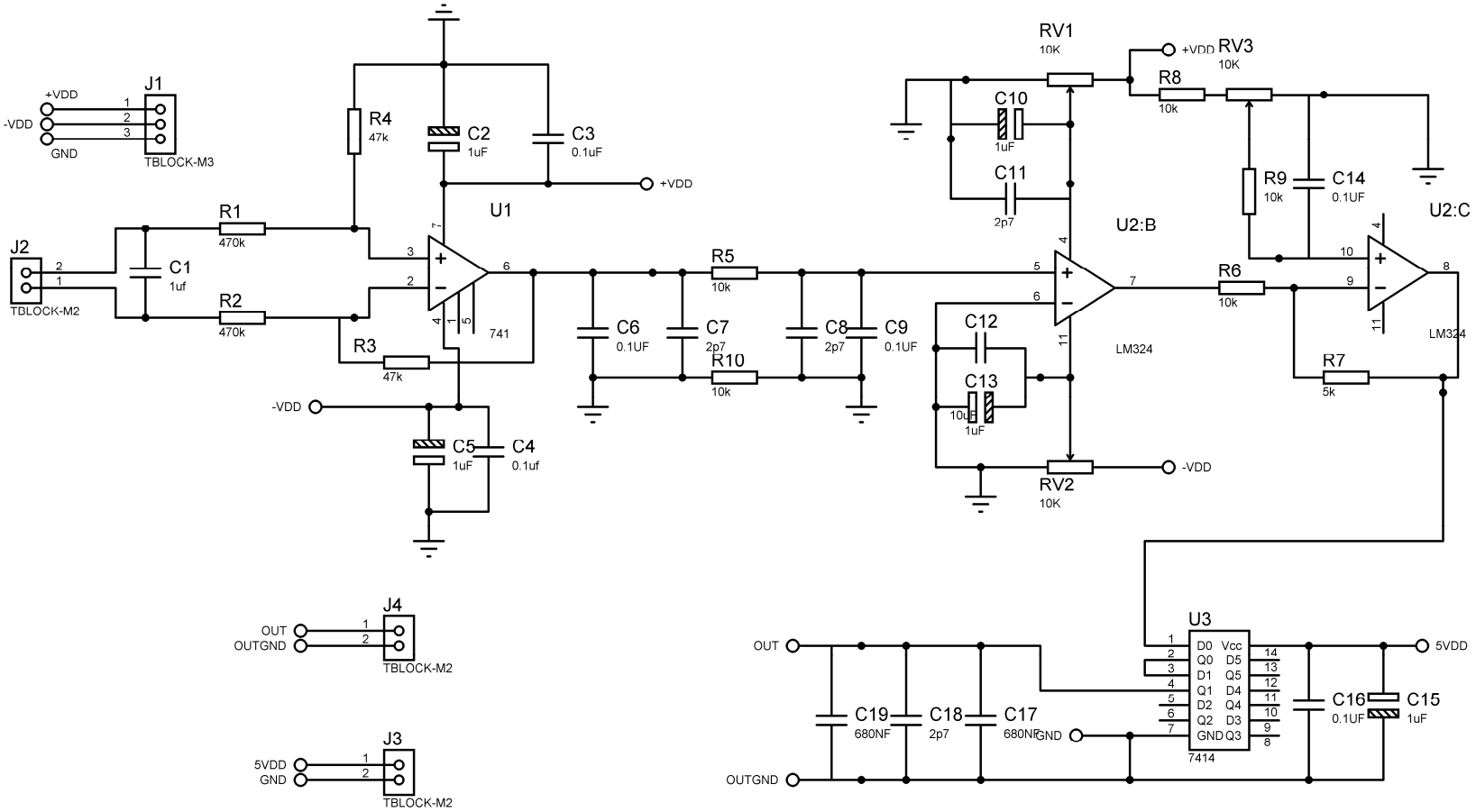

Figure A1: Citcuit diagram for speed measurement

Voltage and current sensors

B1. Voltage sensor LV 25P

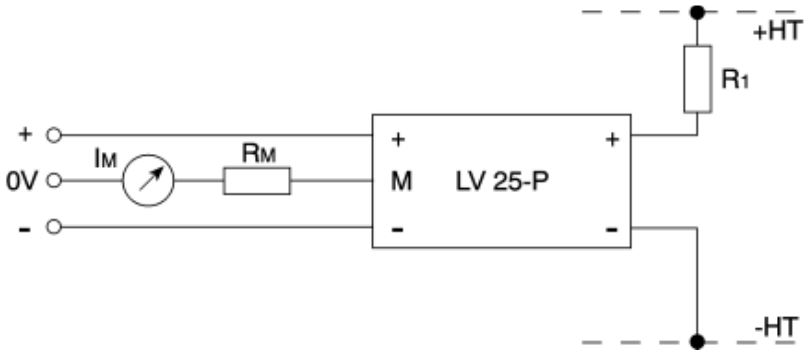

Figure B1: Hall Effect voltage sensor LV-25P

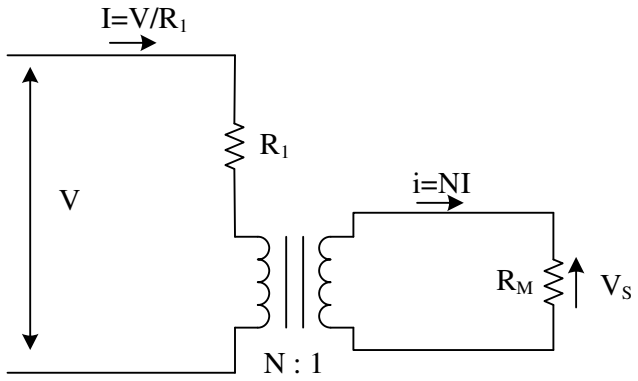

Figure B2: Internal circuit voltage sensor LV-25P

Input maximum measured voltage V = 600 V

Input current I = 10 mA,

R_1 = V/I = 600 V/10 mA =60KΩ

The transformer is supposed to have a turn ratio 1000:2500,

i = 2.5×I = 25 mA

The ADC input maximum voltage is 3V, so V_S = 3V

$R_M=V_S/I$=3V/25mA= 120 Ω

B2. Current sensor LA 55P

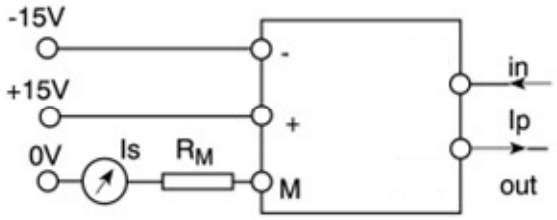

Figure B3: Hall Effect current sensor LA-55P

Input maximum current Ip =10A

The conversion factor for the hall-effect sensor inbuilt transformer is 1:2000. Therefore the secondary current would be 1/1000 times the primary current

$I_s = I_p/2000 = 10/1000 = 0.01A$

The ADC input maximum voltage is 3V, so $V_S = 3V$

$R_M = V_S/I = 3/0.01 = 300\ \Omega$

List of Publications

Journal Papers

[1] A Ananda Kumar and Dheerendra Singh, "An IFOC-DSVPWM Based DC-Link Voltage Compensation of Z-Source Inverter Fed Induction Motor Drive for EVs," *Hindawi Adv. Power Electron.*, vol. 2015, pp. 1-14, 2015.

[2] A Ananda Kumar and Dheerendra Singh, "Digital Implementation of DSVPWM Control for EV fed through Impedance Source Inverter," *Int. J. Power Electron. Drive Syst.*, vol. 6, no. 3, 2015.

[3] A Ananda Kumar and Dheerendra Singh, "Implementation of New Algorithm for EV fed through an Impedance Source Inverter," *Int. J. Appl. Eng. Res. (IJAER),* vol. 10, no. 10, pp. 26321-26338, 2015.

Journal Papers Communicated

[1] A Ananda Kumar and Dheerendra Singh, "FGS-PI Controller based DC-Link Voltage Control of Quasi Z-Source Inverter fed Induction Motor Drive for EVs," *IEEE Trans. Ind. Appl.* 2015.

[2] A Ananda Kumar and Dheerendra Singh, "Implementation of Voltage Sag Ride Through for Impedance Source Inverter fed Induction Motor Drive based on Predictive Current Control Technique," *IEEE Trans. Ind. Electron.* 2015.

[3] A Ananda Kumar and Dheerendra Singh, "FGS-PI Controller based DC-Link Voltage Control of Z-Source Inverter fed Induction Motor Drive for EVs," *IEEE Trans. Power Electron.* 2015.

Conferences in Abroad

[1] A Ananda Kumar and Dheerendra Singh, "The IFOC Based Speed Control of Induction Motor fed by A High Performance Z-Source Inverter," in *Proc. IEEE Conf. Renewable Energy Research and Application (ICRERA)*, 2014, pp. 539-543.

Conferences in India

[1] A Ananda Kumar and Dheerendra Singh, "DSP based IFO control of HEV fed through impedance source inverter," in *Proc. IEEE Conf. Annual IEEE India Conference (INDICON)*, 2013, pp. 1-6.

[2] A Ananda Kumar and Dheerendra Singh, "New Control Algorithm for Impedance (Z-Source) Inverter," in *Proc. IEEE Conf. Automation, Computing, Communication, Control and Compressed Sensing (iMac4s)*, 2013, pp. 656-661.

[3] A Ananda Kumar and Dheerendra Singh, "Implementation of Indirect field Oriented Control of HEV fed through Impedance Source Inverter," in *First National Conference on Power Electronics Systems & Applications (PESA-2013)*, 2013.

[4] A Ananda Kumar and Dheerendra Singh, "Novel Control Algorithm for Impedance Source Inverter," in *First National Conference on Power Electronics Systems & Applications (PESA-2013)*, 2013.

[5] A Ananda Kumar and Dheerendra Singh, "Double Sine Pulse Width Modulation Control of Impedance-Network Inverter," in *Proc. IEEE Conf. Emerging Trends in Electrical Engineering and Energy Management (ICETEEEM)*, 2012, pp. 345-349.

[6] A Ananda Kumar and Dheerendra Singh, "DSC based Modified Unipolar Switching Techniques for Single Phase Z Source Inverter," in *Centenary Conference-EE, IISC, Bangalore*, 2011, no. Dec, pp. 69-75.

[7] A Ananda Kumar and Dheerendra Singh, "Solar Power Based Impedance - Source Converter for BLDC Motor With Closed loop Control," in *Proc. IEEE Conf.Process Automation, Control and Computing (PACC)*, 2011, pp. 1-6.

Brief Biography of the Candidate

A Ananda Kumar completed B.Tech in Electrical and Electronics Engineering from Narayana Engineering College, Nellore, Andhra Pradesh, India in 2004. He received M.Tech in Power Electronics and Drives from SRM University, Chennai, Tamil Nadu, India in 2006. Presently, he is pursuing Ph.D. and working as a Lecturer in Department of Electrical and Electronics Engineering, Birla Institute of Technology and Science BITS-Pilani, Pilani Campus, Rajasthan, India. His research interests include Power Electronics and Drives, Renewable Energy Systems, DSP Controller and Design of Converters.

Brief Biography of the Supervisor

Prof. (Dr.) Dheerendra Singh obtained B.E. (Electrical Engineering) from Indian Institute of Technology (IIT), Roorkee. He received M.Tech from IIT Delhi. He did his Ph.D. from BITS-Pilani, Pilani Campus. He joined Birla Institute of Technology and Science (BITS), Pilani, Rajasthan in 1999. Presently, he is working as Assistant Professor in BITS-Pilani, Pilani Campus. He is more involved in teaching and research in the area of Power Electronics based Renewable Energy Systems, Controls and Drives. He successfully co-ordinated many graduate programme for the industries like NTPC, CFCl, Hindustan Zinc etc. He is on Doctoral Advisory Committee (DAC) for Ph.D. students. He is senior member of various professional bodies. He has over 30 research publications. He visited University of Wisconsin, USA for presenting research papers.